UNIVERSITY OF CALIFORNIA SAN DIEGO

A study of near-inertial internal wave generation and the story of pelican flight.

A dissertation submitted in partial satisfaction of the
requirements for the degree
Doctor of Philosophy

in

Engineering Sciences (Mechanical Engineering)

by

Ian Stokes

Committee in charge:

Professor Andrew Lucas, Chair
Professor Matthew Alford
Professor Samuel Kelly
Professor Stefan Llewellyn-Smith
Professor Oliver Schmidt

2023

The dissertation of Ian Stokes is approved, and it is acceptable in quality and form for publication on microfilm and electronically.

University of California San Diego

2023

DEDICATION

To my Grandad, Rod MacPherson.

EPIGRAPH

"We know less about the ocean's bottom than about the moon's back side."

— Roger Revelle.

TABLE OF CONTENTS

LIST OF FIGURES

LIST OF TABLES

ACKNOWLEDGEMENTS

I am grateful for my family – my parents, brother and my loving partner Emily MacDonell – I couldn't have made it here without your love and support! I extend my gratitude to my advisor, Drew Lucas, and the rest of the team at the Multiscale Ocean Dynamics Group, especially the engineers, technicians, my fellow graduate students and postdocs, and the interns/undergraduates. Huge thanks to Captain Brett Pickering, Marine Physical Laboratory, Rich Walsh and the SIO scientific diving community. Lastly, thanks to Bucky, Trinity, and the rest of the dogs of Neirenberg Hall, and of course, the brown pelicans of the Pacific coast!

Chapter 1, in full, is a reprint of the material as it appears in Wave-slope soaring of the brown pelican, Movement Ecology. Ian A. Stokes, Andrew J. Lucas; *Published* 2021. The dissertation author was the primary investigator and author of this paper.

Chapter 2, in full, is a reprint of the material as it appears in A generalized slab model, Journal of Physical Oceanography. Ian A. Stokes, Samuel M. Kelly, Andrew J. Lucas, Amy F. Waterhouse, Caitlin B. Whalen, Thilo Klenz, Verena Hormann, Luca Centurioni; *Minor Revisions* 2023. The dissertation author was the primary investigator and author of this paper.

Chapter 3, in full, is a reprint of the material as it appears in Near-inertial wave generation in a linear, damped mixed layer model, Journal of Physical Oceanography. Ian A. Stokes, Samuel M. Kelly, Andrew J. Lucas; *In Preparation* 2023. The dissertation author was the primary investigator and author of this paper.

VITA

2012-2016	B. S. in Physics *cum laude*, University of California, Santa Barbara
2018-2019	M. S. in Engineering Sciences (Mechanical Engineering), University of California San Diego
2023	Ph. D. in Engineering Sciences (Mechanical Engineering), University of California San Diego

PUBLICATIONS

Gregory Sinnett, Kristen A. Davis, Andrew J. Lucas, Sarah N. Giddings, Emma Reid, Madeleine E. Harvey, Ian A. Stokes; "Distributed Temperature Sensing for Oceanographic Applications", *Journal of Atmospheric and Oceanic Technology*, **37**, 1987-1997, (2020).

Ian A. Stokes, Andrew J. Lucas; "Wave Slope Soaring of the Brown Pelican", *Movement Ecology*, **9**, 13, (2021).

Ian A. Stokes, Samuel M. Kelly, Andrew J. Lucas, Amy F. Waterhouse, Caitlin B. Whalen, Thilo Klenz, Verena Hormann, Luca Centurioni; "A Generalized Slab Model", *Physical Oceanography*, *Minor Revisions*.

Leif N. Thomas, Samuel M. Kelly, Thilo Klenz, William R. Young, Luc Rainville, Harper Simmons, Verena Hormann, Ian Stokes; "Why near-inertial waves are less affected by vorticity in the Northeast Pacific than in the North Atlantic", *The Oceanography Society*, *In Review*.

Samuel M. Kelly, Erica L. Green, Ian A. Stokes, Jay A. Austin, Andrew J. Lucas, Jonathan D. Nash; "Direct observations of coastally generated near-inertail waves", *Journal of Physical Oceanography*, *In Review*.

Ian A. Stokes, Samuel M. Kelly, Andrew J. Lucas; "Near-inertial wave generation in a linear, damped mixed layer model", *Journal of Physical Oceanography*, *In Preparation*.

ABSTRACT OF THE DISSERTATION

A study of near-inertial internal wave generation and the story of pelican flight.

by

Ian Stokes
Doctor of Philosophy in Engineering Sciences (Mechanical Engineering)
University of California San Diego, 2023
Professor Andrew Lucas, Chair

Organizational notes. This dissertation consists of three distinct contributions in the field of Applied Ocean Science. These contributions are not directly related, and each serve as a stand-alone scientific work. As such, the dissertation is written and formatted as three independent chapters. These are titled *'Wave-slope soaring of the brown pelican'* (published in *Movement Ecology*, 2020), *'A generalized slab model'* (submitted to *Journal of Physical Oceanography* and in review), and *'Near-inertial wave generation in a linear, damped mixed layer model'* (in preparation for submission to *Journal of Physical Oceanography*). The abstract of each chapter is included below. Following these abstracts, we will dive right into *'Wave-slope soaring of the brown pelican'* in Chapter 1.

(1) Wave-slope soaring of the brown pelican. From the laboratory at Scripps Institution of Oceanography, one can observe the brown pelican (*Pelecanus occidentalis*) traveling along the crests of near-shoaling waves just outside the surf zone. In this manner, the birds travel great distances without flapping, all the while a scant ~ 30 cm off the ocean's surface. Here we derive a theoretical framework for assessing the energetic benefit of this behavior, "wave-slope soaring," in which an organism in flight takes advantage of updrafts caused by traveling ocean surface gravity waves. The energy cost of steady, constant altitude flight is analyzed as a control. Potential flow theory is used to quantify the ocean wave-induced wind associated with near-shoaling, weakly nonlinear, shallow water ocean surface gravity waves. Using a regular expansion of the Stokes stream function and the Green's function for Laplace's equation in 2D with Dirichlet boundary conditions, we obtain integral expressions for the horizontal and vertical components of the wave-induced wind. The development of these relationships produces expressions for the components of the wave-induced wind in a frame of reference moving with the wave. Wave-slope soaring flight is then analyzed using an energetics-based approach for waves of typical ocean conditions (wave height of 1m, period of 10s) and the body plan of *P. occidentalis.* For pure ground effect flight, we calculate an upper bound mechanical advantage of $\sim$ 20 - 25% as compared with steady, level flight without ground effect. When wave-slope soaring is employed, we calculate an upper bound mechanical advantage of $\sim$ 50 - 60% as compared with steady, level flight without ground effect. The theoretical development presented here suggests there are energy savings associated with wave-slope soaring. Individual brown pelicans may gain upwards of 50% mechanical advantage utilizing this mode of flight under typical ocean conditions, as compared to steady, level flight out of ground effect. Thus wave-slope soaring appears to provide a significant benefit to these highly mobile organisms that depend on patchy prey distribution over large home ranges.

(2) A generalized slab model. We construct a generalized slab model to calculate the ocean's linear response to an arbitrary, depth-variable forcing stress profile. To introduce a first-order improvement to the linear stress profile of the

traditional slab model, a piecewise-nonlinear stress profile which allows momentum to penetrate into the transition layer (TL) is used (denoted 'mixed layer/transition layer,' or MLTL stress profile). The MLTL stress profile induces a two-fold reduction in power input to inertial motions relative to the traditional slab approximation. The primary reduction arises as the TL allows momentum to be deposited over a greater depth range, reducing surface currents. The secondary reduction results from the production of turbulent kinetic energy (TKE) beneath the mixed layer (ML) related to interactions between shear stress and velocity shear. Direct comparison between observations in the Iceland Basin, the traditional slab model, the generalized slab model with the MLTL stress profile, and the Price-Weller-Pinkel (PWP) model suggest that the generalized slab model offers improved performance over a traditional slab model. In the Iceland Basin, modeled TKE production in the TL is consistent with observations of turbulent dissipation. Extension to global results via analysis of Argo profiling float data suggests that on the global, annual-mean, $\sim 30\%$ of the total power input to near-inertial motions is allocated to TKE production. We apply this result to the latest global, annual-mean estimates for near-inertial power input (0.27 TW) to estimate that 0.08 ± 0.01 TW of the total near-inertial power input are diverted to TKE production.

(3) Near-inertial wave generation in a linear, damped mixed layer model. We present a new model for studying near-inertial internal wave (NIW) generation. In development of the model, we provide a theoretical perspective on the NIW generation process which is exactly analogous to that of internal tide generation proposed by Llewellyn Smith and Young [2002]. We consider NIW generation via wind-stress curl, latitudinal variability of the Coriolis parameter (the β-effect) and lateral variability of the mesoscale eddy field (the ζ-effect) using this model. We separate the forcing function and wave response in the model, which reveals that beta and zeta refraction can produce high-wavenumber variability that does not generate waves. This contradicts the common assumption that NIWs are generated at scales which identically mirror their forcing. A spectral approach is used in tandem with the model that allows us to constrain the scales of NIW generation for each mode. Because the vertical energy propagation associated with

internal waves is a function of the total wave generation and the lateral scale of these waves, this technique may prove to be a useful tool in reducing uncertainties related to how NIWs impact the global ocean's energy budget.

Chapter 1

Wave-slope soaring of the brown pelican

Authors: Ian A. Stokes and Andrew J. Lucas

1.1 Background

Some birds are able to fly with little flapping by exploiting energy present in the ambient wind field Rayleigh [1883], Pennycuick [1973], Wilson [1975], Pennycuick [1983], Taylor et al. [2016]. When these energy gains are great enough to offset the cost of flight, the phenomenon is known as 'soaring' Rayleigh [1883], Cone [1962]. As an energy efficient means of searching for prey or travelling long distances, soaring behaviors are widespread in avians and have demonstrated ecological significance Taylor et al. [2016], Richardson [2011], Richardson et al. [2018], Richardson [2019].

Soaring behaviors in general take advantage of the structure and variability of the fluid flow in the lower atmosphere Pennycuick [1973, 1983]. For example, when the desert floor and the still air just above is heated by the midday summer sun, vigorous thermal convection can occur. 'Thermal soaring' is the familiar behavior associated with catching these updrafts, and is used to gain altitude and locate prey from long distances Pennycuick [1973, 1983]. The moving atmosphere impinging on raised topography also can create strong vertical flows. 'Slope soaring' takes

advantage of updrafts that are created by the vertical redirection of airflow over cliffs and steep hills Pennycuick [1973, 1983].

Soaring behaviors are not limited to localized convection or the presence of topographic obstacles. In the windswept mid- and high-latitude open ocean, seabirds use the vertical shear of wind within the turbulent atmospheric boundary layer to gain energy in a behavior known as 'dynamic soaring' Richardson [2011], Richardson et al. [2018], Idrac [1925], Sachs et al. [2013]. The wandering albatross can circumnavigate the globe, rarely flapping their wings, by employing this technique Richardson [2011], Richardson et al. [2018]. The potential for using vertical shear in horizontal winds to power continuous flight was first recognized by Leonardo da Vinci in the 16th century Richardson [2019].

However, even in conditions with little to no ambient wind, albatrosses have been reported to track and follow waves on the ocean surface for long distances Richardson [2011], Froude et al. [1892]. At the coastline during calm conditions, pelicans can also be seen tracking the crests of shoaling waves just outside of the surf-zone, often in formation.In this fashion, they appear to be able to gain forward speed and thus kinetic energy, which they then convert to height, peeling off and upwards just as the wave begins to break. This altitude is then used to glide downwards and offshore to the subsequent approaching wave. By linking individual waves together, the birds can travel hundreds of meters or more with limited flapping.

Here we theoretically examine the possibility that the vertical component of the wind induced by traveling ocean waves Idrac [1925] may explain the birds' tendency to follow wave crests Wilson [1975], Richardson [2011], Idrac [1925]. This behavior, which we term 'wave-slope soaring,' is shown by this analysis to have significant cost-benefit to energy efficient travel by comparison to steady level flight in and out of ground effect. It is a special case of 'slope soaring' flight with the primary difference that in wave-slope soaring, the updrafts are driven by traveling ocean surface waves Wilson [1975], Richardson [2011], Idrac [1925], Jameson [1958] pushing against a still atmosphere, rather than wind encountering a fixed object Pennycuick [1973, 1983].

1.2 Methods

The goal is to estimate the energy savings associated with wave-slope soaring (WSS) flight. To accomplish this, we perform a theoretical study of the brown pelican practicing WSS over near-shoaling coastal waves. First, controls are developed in section 1.1. There we analyze the cost of steady, constant altitude pelican flight in the absence of ocean surface waves, out of ground effect (OGE, section 1.1.1) and in ground effect (GE, section 1.1.2). In both cases, our description of the energetics uses energy consumption per distance travelled, or 'cost of transport' (COT) as the minimizing function Taylor et al. [2016]. These two results provide a baseline with which to compare the energy savings associated with wave-slope soaring flight, since flight in ground effect has demonstrated flight efficiency benefits Hainsworth [1988], Suh and Ostowari [1988], Laitone [1990], Rayner [1991], Johansson et al. [2018].

Second, a description of the updrafts caused by near-shoaling waves is needed. In the air-sea interactions literature, any displacement of the atmosphere caused by traveling waves is known as 'wave-induced wind'. The description of wave-induced wind is, in general, very complex due to the broad spectrum of ocean surface waves and nonlinear wave-wave and wave-wind interactions Semedo et al. [2009], Sullivan and McWilliams [2010], Edson et al. [2013], Buckley and Veron [2016]. However, since wave-slope soaring behavior is seen in calm wind conditions close to the coastline in the brown pelican, and appears to favor smooth, long-crested swells, we proceed with a simplified model. This model describes wave-induced wind in zero ambient wind conditions offshore of the depth of wave-breaking (Sec. 1.2, 1.3). To retain some of the nonlinearities intrinsic to shoaling waves, but allow the problem to be analytically tractable, we assume a waveform shape of the well-studied soliton Barthélemy [2004]. This approach has been effective in modeling near-shoaling, shallow water, ocean surface gravity waves, and was shown to be a reasonable representation of and ocean surface gravity wave in the region just outside of the surf zone, where nonlinear steepening begins Barthélemy [2004].

We use potential flow theory to model the wave-induced wind over these solitary waves. This is a significant simplification since, being an inviscid model, it

Table 1.1: Average Brown Pelican Parameters Pennycuick [1983].

Parameter	**Symbol**	**Value**
Mass	M	2.65 kg
Wingspan	b	2.10 m
Maximum Wing Area	$S_{w_{max}}$	0.45 m^2
Wing Loading	$W/S_{w_{max}}$	57.8 N/m^2
Aspect Ratio	A	9.8

does not account for development of boundary layers, especially on the trailing face of the moving wave. Obervations have shown that there are weak wind conditions where the atmospheric boundary layer remains laminar and well-attached Smedman et al. [1994], Stull et al. [2000], Angevine et al. [2006], justifying the use of an inviscid assumption here. This assumption is violated in moderate and strong wind conditions, when a separated, turbulent boundary layer forms between wave-crests Banner and Melville [1976], Högström et al. [2009], Smedman et al. [2009], Soloviev and Kudryavtsev [2010].

Since we observe the wave-slope soaring behavior in weak wind conditions, we assert for our model that the atmosphere is initially at rest, the ocean surface is smooth, the wave steepness is small, and the dynamics of the wave-induced wind in this idealized case can be largely captured by inviscid theory. Crucially, in what follows, we provide a comparison of the wave-induced wind produced by our potential flow model to measurements by Grare et al. [2018] in Sec. 1.3.

Armed with the vertical component of the wave-induced wind from our inviscid model, we evaluate the cost of transport for flight through a moving medium following Taylor et al. [2016]. We then assess the efficiency of flight in WSS for a range of environmental/flight conditions, and compare to flight OGE and flight in GE to assess possible energy benefit of WSS flight (Sec. 1.4). The physical characteristics of the brown pelican relevant to flight are drawn from Pennycuick Pennycuick [1983] and given in Table 1.1.

Figure 1.1: Photograph of a brown pelican using wave-slope soaring flight on a calm day in La Jolla, CA.

1.2.1 Steady, Level Pelican Flight in the Absence of Ocean Waves

We decompose the total aerodynamic drag into profile, parasitic, and induced drag components Pennycuick [1989, 2008]. Profile drag arises primarily from friction drag, and secondarily from pressure drag, both acting on the wings. Parasitic drag results primarily from pressure drag, and secondarily from friction drag, acting on the body. Finally, induced drag is a consequence of lift generation, associated with the downwash required to produce lift Taylor et al. [2016], Rayner [1991], Pennycuick [1989], Taylor and Thomas [2014]. From Pennycuick [1989, 2008], we write the total drag experienced by a bird gliding in still air at equilibrium as a function of airspeed u, such that

$$D_{oge}(u) \approx \frac{\rho u^2}{2}\left(b\bar{c}C_{D_{pro}} + S_b C_{D_{par}}\right) + \frac{2k}{\pi\rho}\left(\frac{mg}{bu}\right)^2, \tag{1.2.1.1}$$

where ρ is air density (1.225 kg/m^3), b is wingspan, $\bar{c}$ is the mean chord length, S_b is the body frontal area, m is the mass of the bird, k is the induced drag factor, and g is gravitational acceleration. $C_{D_{pro}}$ and $C_{D_{par}}$ are the profile and parasitic

drag coefficients, respectively.

With units of [J/m], (1.2.1.1) can be interpreted as the COT for gliding flight in a still medium. In the case of gliding flight through a moving medium, (i.e. wind) Taylor et al. [2016] show that the theoretical COT ($\mathcal{C}$) can be expressed as

$$\mathcal{C} \approx \frac{Du - mgw_u}{\sqrt{(u - w_h)^2 + w_s^2}} = \frac{Du - mgw_u}{U}, \tag{1.2.1.2}$$

where w_u is the vertical component of the wind, w_h is the headwind experienced by the bird, and w_s is the crosswind experienced by the bird. Taylor et al Taylor et al. [2016] show that the denominator in (1.2.1.2) can be equivalently expressed as the groundspeed (U). Note that in the presence of ambient wind, $u \neq U$. In the case where $w \to 0$, the airspeed and groundspeed equate (i.e. $u \to U$) and (1.2.1.2) simplifies to (1.2.1.1). In Section 1.4, we assess wave-slope soaring where the still-air initial condition is relaxed, necessitating the introduction of (1.2.1.2).

Beginning with the first term on the right hand side of (1.2.1.1), which represents the profile drag, we calculate the standard mean chord $\bar{c}$ assuming a straight tapered wing with constant area ($S_{w_{max}}$) and constant wingspan (b) given by Pennycuick Pennycuick [1983] in Table 1.1. This calculation yields $\bar{c} = S_{w_{max}}/b = 0.21$ m. Taylor & Thomas Taylor and Thomas [2014] propose setting $C_{D_{pro}} = 2.656 \cdot \mathrm{Re}^{-1/2}$, where $\mathrm{Re} = \rho \bar{c} u/\mu$ is the chord Reynolds number, and μ is the dynamic viscosity of air ($1.81 \cdot 10^{-5}$ kg/m·s). We will follow this assumption in our analysis to account for variation of the profile drag with changes in airspeed.

The second term on the right hand side of (1.2.1.1) represents the contribution from parasitic drag, which is difficult to estimate for seabirds Taylor et al. [2016]. Taylor & Thomas Taylor and Thomas [2014] suggest setting $S_b C_{D_{par}} = 0.01 \cdot S_{w_{max}}$. This formulation shows agreement with field estimates of the parasitic drag on diving passerines Hedenstrom and Liechti [2001].

To characterize the induced drag, the third term in (1.2.1.1), we must assign a value to the induced drag factor, k. The induced drag factor is directly related to the wing shape Taylor et al. [2016], Pennycuick [2008], Taylor and Thomas [2014], Tucker [1993]. The slotted tips of the brown pelican wing Pennycuick [1983] act as winglets in tandem to reduce the induced drag experienced in gliding flight Tucker

[1993]. However, these winglets do not reduce k Munk [1923], Hummel [1980]. In Pennycuick's model Pennycuick [2008], a k value of 1.1 is used as default–Taylor & Thomas Taylor and Thomas [2014] show that only for an efficient elliptically loaded wing, rounding this factor down to $k \approx 1$ is appropriate. Accordingly, for a conservative estimate we will assume $k = 1.1$.

Flight out of Ground Effect

To analyze cost benefits of flight in ground effect (GE), we must first obtain a baseline comparison through analysis of the steady, constant altitude flight of a pelican in still air, out of ground effect (OGE). First, we assess the COT for a range of airspeeds (u) by using the parameters in Table 1 and Section 1.1 with (1.2.1.1) and evaluate for a range of values of airspeed u between [8, 20] m/s for comparison with Pennycuick [1983], Schnell and Hellack [1978]. We refer to the airspeed that minimizes the COT as the minimum-cost velocity, denoted u_{mc}. Second, we quantify the required power output by the bird for a given COT. This is done by multiplying the COT with the corresponding airspeed, as the gliding flight here is apprioximated to be level.

Thus, power expenditure out of ground effect as a function of airspeed, $P_{oge}(u)$, can be written as

$$P_{oge}(u) \approx \frac{\rho u^3}{2}\left(b\bar{c}C_{D_{pro}} + S_b C_{D_{par}}\right) + \frac{2k}{\pi\rho u}\left(\frac{mg}{b}\right)^2, \tag{1.2.1.3}$$

The airspeed that minimizes the required power output will be referred to as the minimum-power velocity, denoted u_{mp}. The results of this analysis are displayed in Figure 1.2. COT and power output as functions of airspeed are shown in the top and bottom panels, respectively.

Using the values corresponding to the brown pelican as given in Section 1.1 and the density and viscosity of air at sea level, we find that $u_{mc} \sim 13.4$ m/s with a corresponding COT calculated from (1.2.1.1) of ~ 1.5 J/m. Though u_{mc} provides the minimum COT, this value exceeds $u_{mp} \sim 10.0$ m/s, which is calculated by minimizing (1.2.1.3) with respect to velocity.

The precise measurement of the metabolic power input for brown pelican flight

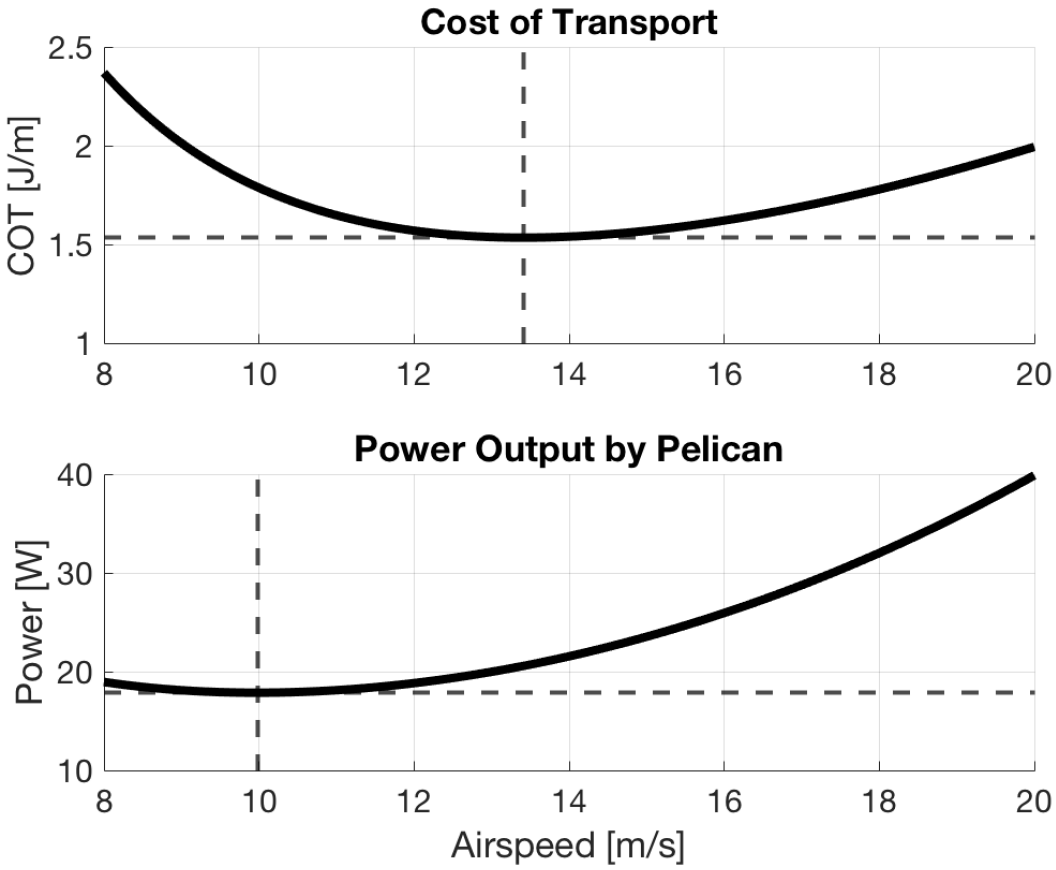

Figure 1.2: Efficiency of steady, level flight out of ground effect in absence of ocean waves. Top Panel: COT as a function of airspeed for steady, level flight out of ground effect (OGE). Minimum-cost velocity $\sim$ 13.4 m/s with a corresponding COT of $\sim$ 1.5 J/m. Bottom Panel: Power output as a function of airspeed for steady, level flight OGE. Minimum-power velocity $\sim$ 10.0 m/s with a corresponding power output of $\sim$ 17.9 W.

is not readily available in the literature. Noting that the mean airspeed from Pennycuick [1983] lies roughly halfway between u_{mc} and u_{mp}, we estimate the range of power expenditure for the brown pelican to be roughly $[P(u_{mp}),\ P(u_{mc})]$ for steady, level flight. Using (1.2.1.3), we calculate this range of expected power output to be $\sim [17.9,\ 20.6]$. W. Ballance Ballance [1995], in study of the red footed booby, a smaller marine bird, found that it expends an average of ~ 20 W in gliding flight. Though further experiment will be required to verify our estimated power requirement of the brown pelican in steady, level flight, we use this minimum COT as the primary control for what follows.

Flight in Ground Effect

Flight in ground effect decreases the induced drag, which is commonly referred to as 'induced drag savings' Hainsworth [1988]. This is estimated using a drag reduction factor, ϕ, that is a function of flight height H and wingspan b. The profile and parasitic drag, which are related to the form of the flier only, remain unchanged Hainsworth [1988], Suh and Ostowari [1988], Laitone [1990], Rayner [1991]. Ground effect occurs when $\phi < 1$ for heights less than one wingspan ($H < b$) and tends to $\phi \approx 1$ as $H > b$ Suh and Ostowari [1988], Laitone [1990].

An analytical expression for ϕ is given by Laitone [1990], which is written as

$$\phi = \frac{1 - 2/\pi + (16H/\pi b)^2}{1 + (16H/\pi b)^2}. \tag{1.2.1.4}$$

Including this factor in (1.2.1.1) gives an expression for the total drag experienced in GE, written

$$D_{ge}(u) \approx \frac{\rho u^2}{2}\left(b\bar{c}C_{D_{pro}} + S_b C_{D_{par}}\right) + \phi\frac{2k}{\pi\rho}\left(\frac{mg}{bu}\right)^2. \tag{1.2.1.5}$$

Noting again that for flight in still air the COT equates to the drag, we use (1.2.1.5) to calculate COT in GE for flight heights between 0 to 2m above the sea surface, which corresponds to $H/b \approx 1$ where the GE becomes negligible. These results are shown in Figure 1.3.

Hainsworth Hainsworth [1988] reports average brown pelican ground-effect flight height of 33 cm, with a standard deviation of 5 cm. For flight heights on the

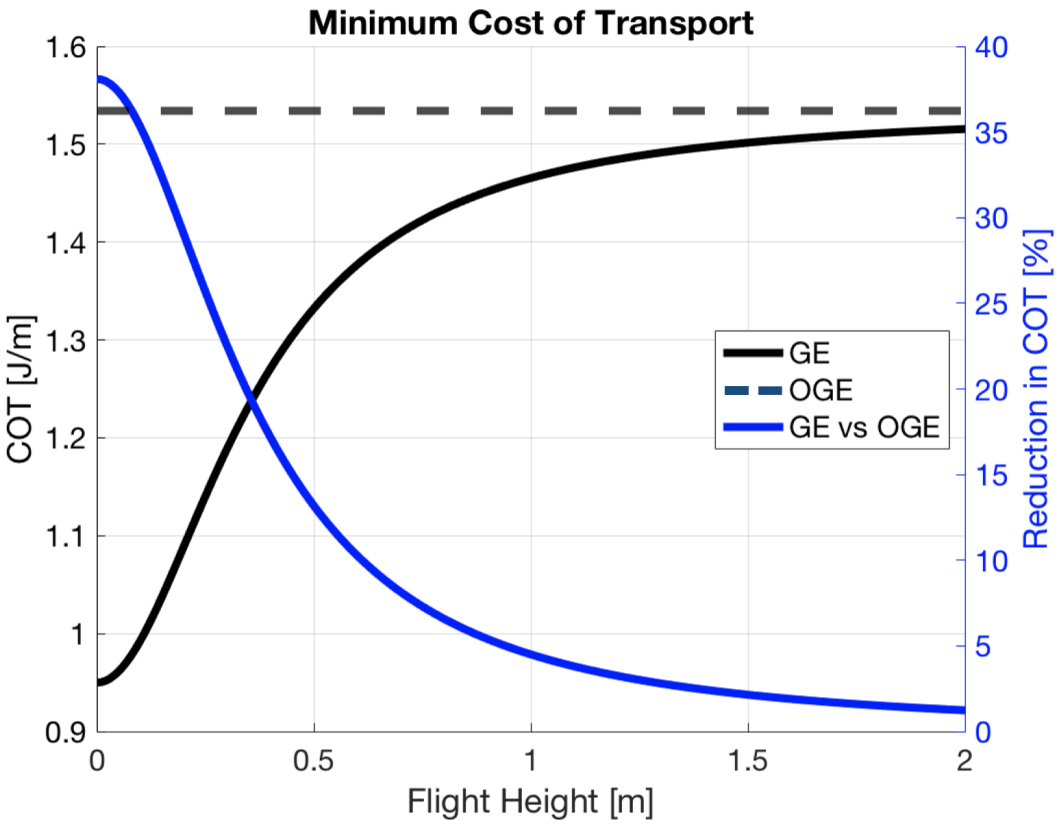

Figure 1.3: Using (1.2.1.5) we calculate the energetics of flight in GE. Minimum Cost of transport as a function of flight height is plotted on the left hand y-axis, in black. Reduction in Minimum Cost of Transport as a function of flight height is plotted on the right hand y-axis, in blue. Note that this compares flight at different airspeeds, as GE reduces the minimum cost velocity Rayner [1991].

range reported by Hainsworth [1988], COT required for flight is $\sim$ 1.1-1.3 J/m, with corresponding percent mechanical advantages of $\sim$ 15-25%, when compared to the 1.5 J/m required for flight OGE. These values agree with Rayner [1991], Johansson et al. [2018].

1.2.2 Airflow Induced by Near-Shoaling Waves

As ocean waves translate, they induce airflow as a result of the no-penetration condition on a boundary, even in the case where there is no ambient wind. Interestingly, wave-induced wind might have been first reported in 1925 by Idrac Idrac [1925] in his study of albatrosses, who noted that large, steep traveling ocean surface gravity waves can produce updrafts with vertical velocity in excess of 2 m/s at 8 meters height. It was also noted that these updrafts effects can be felt up to 15 meters above the ocean surface Idrac [1925].

Research on wave-induced wind has principally focused on its impacts on the ocean and atmospheric boundary layer properties and dynamics. These include both numerical (e.g. Sullivan et al. [2008]) and observational studies (e.g. Högström et al. [2009], Smedman et al. [2009], Soloviev and Kudryavtsev [2010]). Recently, the upward transfer of momentum from ocean swell to the wind was experimentally verified by Grare et al. [2018] in their experiment aboard the Scripps Institution of Oceanography's FLoating Instrumentation Platform (R/P FLIP). Using wave measurement apparatus and an array of ultrasonic anemometers, they estimated wave-induced components of the wind velocity for various wind-wave conditions, producing an empirical curve for wave-induced wind components scaled by surface wave orbital velocity as a function of height above the ocean scaled by surface-wave wavenumber Grare et al. [2018].

We aim to model the process of wave-slope soaring in the coastal ocean offshore of the surf-zone during periods of weak winds, when it is most commonly observed. In this region, the ocean surface waves are depth limited and thus modified from a linear sinusoidal state. It is typical to model ocean gravity waves just offshore of the surf-zone as solitons Barthélemy [2004]. Solitons are localized nonlinear waves that propagate without change of speed or form Lakshmanan [2011]. Here

we assume weak nonlinearity such that we can use the Korteweg-de Vries (KdV) equation Barthélemy [2004]. Note that the KdV equation is valid only for waves in shallow water with $\lambda \gg h$ or equivalently $kh \ll 1$, where λ is the wavelength, k is the wavenumber, and h is the ocean depth.

Neglecting surface tension, we begin with the dimensional traveling soliton solution,

$$\eta(x,t) = A\,\mathrm{sech}^2(kx - \omega t), \tag{1.2.2.1}$$

where

$$\begin{aligned} A &\equiv \frac{4}{3}\,k^2h^3, \\ \omega &\equiv k\sqrt{gh} - \frac{2}{3}\,k^3h^2\sqrt{gh}. \end{aligned} \tag{1.2.2.2}$$

We use the dispersion relation to write the wave's dimensional phase velocity (c) as

$$c = \sqrt{gh}\left[1 - \frac{2}{3}(kh)^2\right]. \tag{1.2.2.3}$$

Our definition for the amplitude in (1.2.2.2) can be used to eliminate k from (1.2.2.3), allowing us to write the phase velocity as a function of amplitude and depth,

$$c = \sqrt{gh}\left[1 - \frac{A}{2h}\right]. \tag{1.2.2.4}$$

We now use the dispersion relation and the definition of amplitude given in (1.2.2.2) to write an expression for the period as a function of amplitude and depth,

$$T = \frac{4\pi h}{\sqrt{3gA}\left(1 - \frac{A}{2h}\right)}. \tag{1.2.2.5}$$

For the waves we consider in the case of WSS flight (Sec. 1.4) with height of 2 meters and period of 15 seconds, the soliton approximation is valid over depths on the order of 10 m, corresponding in our local area to distances of 100 to several hundred meters offshore of the surf zone.

1.2.3 Potential Flow over Solitary Waves

The use of potential flow solutions requires that the fluid be irrotational, incompressible, and inviscid within our region of interest. The symmetry of the

solitary waveform we have imposed justifies the assumption of irrotational flow, while the assumption of incompressible flow is justified by the small Mach number at ocean surface wave velocities. However, as noted in Section 1, the atmospheric boundary layer over the ocean is generally turbulent in moderate to strong winds. This restricts our analysis to weak or no wind conditions. Furthermore, the low amplitude, smoothly varying wave-form used here is meant to approximate shoaling swell in no wind conditions, where flow separation of the wave-induced wind field is unlikely Smedman et al. [1994], Stull et al. [2000], Angevine et al. [2006], Banner and Melville [1976].

We model potential flow over the soliton

$$\eta = A\,\mathrm{sech}^2(kx), \tag{1.2.3.1}$$

moving at phase speed c. We first boost to a frame of reference moving with the soliton such that $U_\infty = -c$. As we are assuming potential flow conditions, the system is governed by Laplace's equation for the stream function,

$$\Delta\psi = 0, \tag{1.2.3.2}$$

with the no penetration boundary condition

$$\left[\mathbf{u}\cdot\hat{\mathbf{n}} = 0\right]_{z=A\ \mathrm{sech}^2(kx)}. \tag{1.2.3.3}$$

Laplace's equation in the upper half plane with a no-penetration boundary condition on the horizontal axis is a well-studied problem that can be solved using Green's theorem. With the proper nondimensionalization, the soliton boundary can act as a small disturbance, or 'perturbation' to this problem. Thus, we will use perturbation theory to derive an approximate solution for the airflow over a soliton.

We introduce the non-dimensional coordinates

$$\zeta = kz, \qquad\qquad \xi = kx. \tag{1.2.3.4}$$

From (1.2.2.2) we can write

$$Ak = \frac{4}{3}(kh)^3. \tag{1.2.3.5}$$

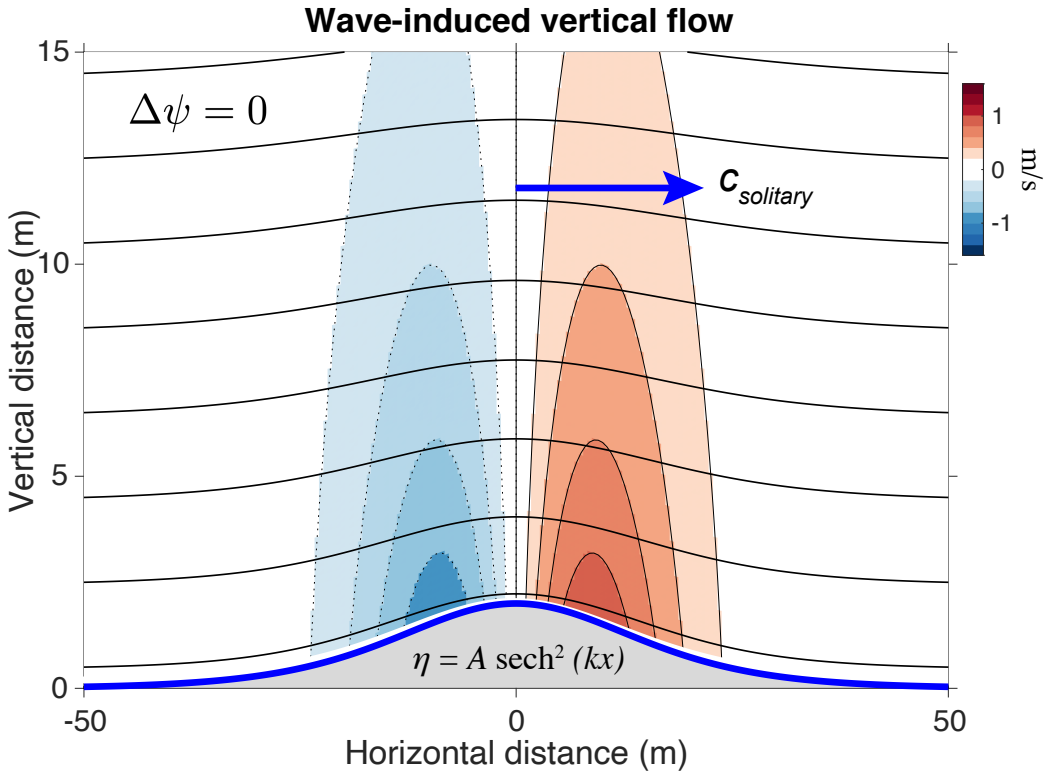

Figure 1.4: Flow visualization of the wave-induced updraft over the soliton $\eta(x) = A\,\mathrm{sech}^2(kx)$ in the $x - z$ plane, forced by the Laplacian, $\Delta\psi = 0$. The soliton shown has wave height $A = 2$ m, period $T = 15$ s, and travels at phase speed $c_{solitary} \approx 7.75$ m/s.

As the soliton was derived in the limit of $\lambda \gg h$, it follows that $kh \ll 1$. We will define another nondimensional coordinate $\epsilon \equiv Ak$ such that $\epsilon \propto (kh)^3 \ll 1$. This coordinate, ϵ, will serve as the small disturbance upon which we build our perturbation expansions. Using (1.2.3.1), (1.2.3.4), and ϵ we can express the boundary in terms of nondimensional coordinates as

$$\zeta = \epsilon\,\mathrm{sech}^2(\xi). \tag{1.2.3.6}$$

Since $\epsilon \ll 1$ in the scaled geometry, to a first approximation we simply have to solve Laplace's equation in the upper half plane.

By the definition of the stream function, we have

$$u_{wi} = \frac{\partial\psi}{\partial\zeta}, \qquad w_{wi} = -\frac{\partial\psi}{\partial\xi}. \tag{1.2.3.7}$$

In this case, the stream function ψ is a function of the spatial variables ξ and ζ, as well as the scaled wave dimension ϵ such that $\psi = \psi(\xi, \zeta, \epsilon)$. The boundary condition (1.2.3.3) enforces that ψ must be constant everywhere on the sea surface. Integrating (1.2.3.7 a), using the condition that as $\xi \to \pm\infty$, $\psi \to -c\,\zeta$, and taking ψ to be constant on the sea surface gives the condition

$$\psi(\xi, \epsilon\,\mathrm{sech}^2\xi) = 0. \tag{1.2.3.8}$$

With $\epsilon \ll 1$, we Taylor expand (1.2.3.8). This gives

$$\psi(\xi, 0) + \epsilon\,\mathrm{sech}^2(\xi)\psi_\zeta(\xi, 0) + O(\epsilon^2) = 0 \tag{1.2.3.9}$$

where subscripts denote partial derivatives. We now expand ψ in a regular perturbation expansion to the order of ϵ, yielding

$$\psi = \psi_0 + \epsilon\,\psi_1 + O(\epsilon^2), \tag{1.2.3.10}$$

where for all ψ_n, with $n \in [0, \infty)$, $\psi_n = \psi_n(\xi, \zeta)$ and $\Delta\psi_n = 0$. At $O(\epsilon^0)$, $\Delta\psi_0 = 0$. Integration yields

$$\psi_0 = -c\,\zeta. \tag{1.2.3.11}$$

Substitution of our perturbation expansion (1.2.3.10) with (1.2.3.11) into (1.2.3.9) gives

$$\epsilon\left[\,\psi_1(\xi, 0) - c\,\mathrm{sech}^2(\xi)\,\right] + O(\epsilon^2) = 0. \tag{1.2.3.12}$$

At $O(\epsilon)$ in (1.2.3.12) we obtain the boundary condition

$$\psi_1(\xi, 0) = c\,\mathrm{sech}^2(\xi), \tag{1.2.3.13}$$

necessary to solve the Laplacian at $O(\epsilon)$, $\Delta\psi_1 = 0$. By Green's theorem, the solution to an arbitrary partial differential equation can be expressed as an integral of the relevant Green's function, provided such a function exists Riley et al. [2002]. This allows us to solve for the $O(\epsilon)$ term of the stream function (ψ_1) using the Green's function for Laplace's equation in the two-dimensional upper half plane with the Dirichlet boundary condition in (1.2.3.13). This particular Green's

function can be written as

$$G\left(\xi,\zeta;\xi',\zeta'\right) = \frac{1}{2\pi}\left(\ln\sqrt{\left(\xi-\xi'\right)^2+\left(\zeta-\zeta'\right)^2} - \ln\sqrt{\left(\xi-\xi'\right)^2+\left(\zeta+\zeta'\right)^2}\right), \tag{1.2.3.14}$$

Riley et al. [2002] where (ξ',ζ') lies within the upper ξ-ζ plane.

Using (1.2.3.13) and (1.2.3.14) with Green's theorem allows us to obtain an expression for $\psi_1(\xi,\zeta)$ as

$$\psi_1(\xi,\zeta) = \frac{c}{\pi}\int_{-\infty}^{\infty}\frac{\zeta\,\mathrm{sech}^2(\xi')}{(\xi-\xi')^2+\zeta^2}\,d\xi', \tag{1.2.3.15}$$

where ξ' is the variable of integration. We remove the singularity by dividing the domain of integration at $\xi' = \xi$. Combining (1.2.3.15) and (1.2.3.11) with (1.2.3.10), we can now obtain a full expression for ψ as

$$\psi = -c\zeta + \frac{Akc}{\pi}\int_0^{\infty}\frac{\zeta}{\xi'^2+\zeta^2}\Big[\mathrm{sech}^2(\xi-\xi') + \mathrm{sech}^2(\xi+\xi')\Big]d\xi' + O(\epsilon^2), \tag{1.2.3.16}$$

where ξ' remains our variable of integration. This expression can now be evaluated numerically.

Using (1.2.3.7 a), we can carry out the differentiation to obtain an integral for the horizontal flow speed u in the frame of reference moving with the wave to the order of ϵ in terms of scaled coordinates as

$$u_{wi} = -c + \frac{Akc}{\pi}\int_0^{\infty}\frac{\xi'^2-\zeta^2}{(\xi'^2+\zeta^2)^2}\Big[\mathrm{sech}^2(\xi-\xi') + \mathrm{sech}^2(\xi+\xi')\Big]\,d\xi' + O(\epsilon^2), \tag{1.2.3.17}$$

where we have substituted the definition of ϵ ($\epsilon \equiv Ak$) back into the expression. Similarly, we can use (1.2.3.7 b) to write an integral for the vertical flow speed w to $O(\epsilon)$ in terms of scaled coordinates as

$$w_{wi} = \frac{2Akc}{\pi}\int_0^{\infty}\frac{\zeta}{\xi'^2+\zeta^2}\Big[\mathrm{sech}^2(\xi-\xi')\tanh(\xi-\xi') + \mathrm{sech}^2(\xi+\xi')\tanh(\xi+\xi')\Big]\,d\xi' + O(\epsilon^2). \tag{1.2.3.18}$$

In order to evaluate the flow velocities, we need the wave number k. As the nonlinearities intrisic to KdV solitons are captured in our expressions for phase velocity (1.2.2.4) and corresponding wave period (1.2.2.5), the linear dispersion relation can be used to obtain an expression for the wavenumber in terms of the phase velocity and period as $k = 2\pi/cT$ Barthélemy [2004]. Note that (1.2.2.4) and (1.2.2.5) can be co-evaluated to produce the phase velocity of our model wave for a given wave height (A) and period (T). Following this analysis, the resultant phase velocity, wavenumber, and given amplitude can be inserted into (1.2.3.17) and (1.2.3.18), yielding the theoretical wave-induced wind in the near-shoaling regime relevant to wave-slope soaring. A visualization of this flow field above a propagating, weakly nonlinear surface wave with no ambient wind is displayed in Figure 1.4.

To validate our expression for wave-induced wind, we compare our predictions to the findings of Grare et al Grare et al. [2018] (Fig. 1.5), using the vertical component of the wave-induced wind non-dimensionalized by surface orbital velocity (Akc), and the previously defined non-dimensional vertical height $\zeta = kz$. In our region of interest ($kz \leq 0.05$), we see good agreement with an empirical fit to the measurements given by Grare et al. as

$$w/Akc = 0.85\Big[1 - 0.66 \cdot \exp\Big(- \Big|\frac{c}{u} - 1\Big|\Big)\Big]\exp(-0.83 \cdot kz), \tag{1.2.3.19}$$

with $r^2 = 0.76$. (Fig. 1.5 Grare et al. [2018]).

1.2.4 Wave-Slope Soaring Flight

We assume that the only wind field is that which is driven by the wave. We define coordinates such that $\hat{\mathbf{x}}$ is in the direction of wave propagation, $\hat{\mathbf{y}}$ is parallel to the wave front, and $\hat{\mathbf{z}}$ is in the vertical direction. A schematic of this coordinate system is shown in the top panel of Figure 1.6. In order to gain benefit from the wave for extended periods of time, the bird must translate in $\hat{\mathbf{x}}$ so that its ground-speed in the direction of wave propagation (U_x) will match the phase velocity of the wave, $V(x,t)$. The phase velocity of the wave is constant under KdV soliton theory so that $V(x,t) = c$, which we calculate for specified wave height and period

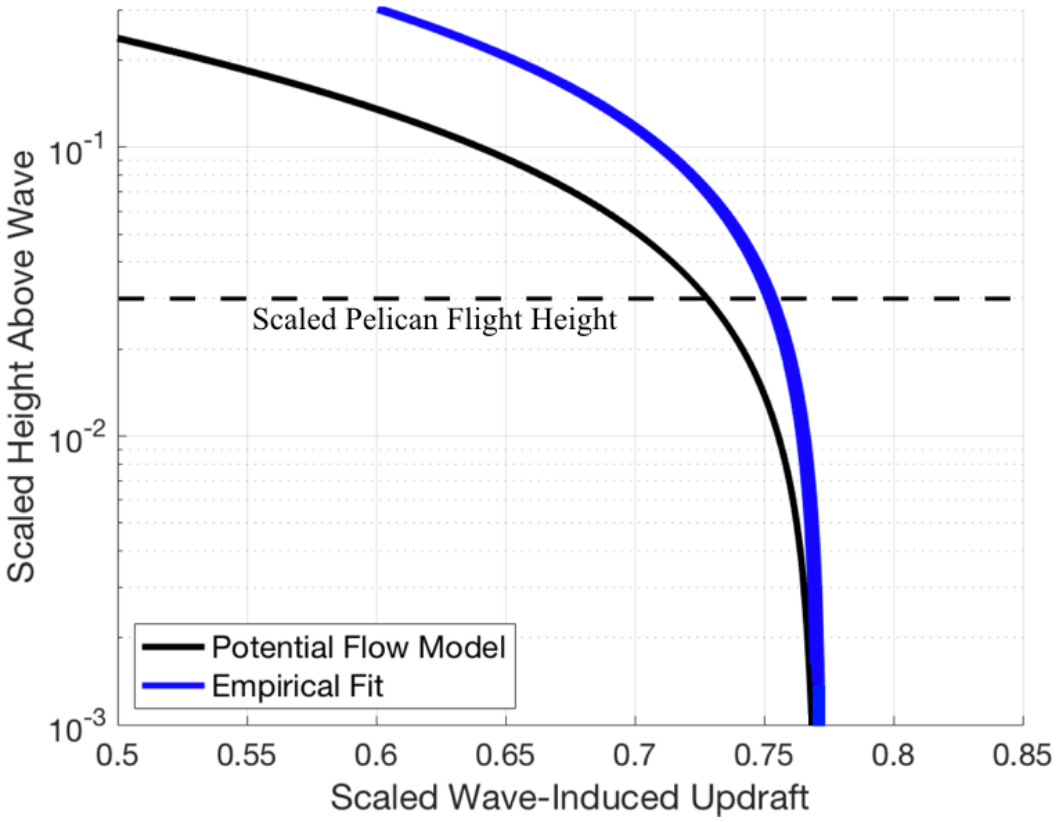

Figure 1.5: Comparison of potential flow theory to measurements by Grare et al Grare et al. [2018]. The vertical component of the wave-induced wind (w_{wi}) scaled with surface orbital velocity (Akc) is shown on the x-axis and scaled height (kz) is shown on the y-axis in a semilog plot. We see that the potential flow estimate of wave induced vertical gives a slight under-prediction but generally agrees with the empirical model best-fit curve for the vertical component of wave-induced wind from Grare et al. [2018]. This comparison to observations gives confidence that the wave-induced wind estimates used here are reasonably representative of the conditions at sea during wave-slope soaring.

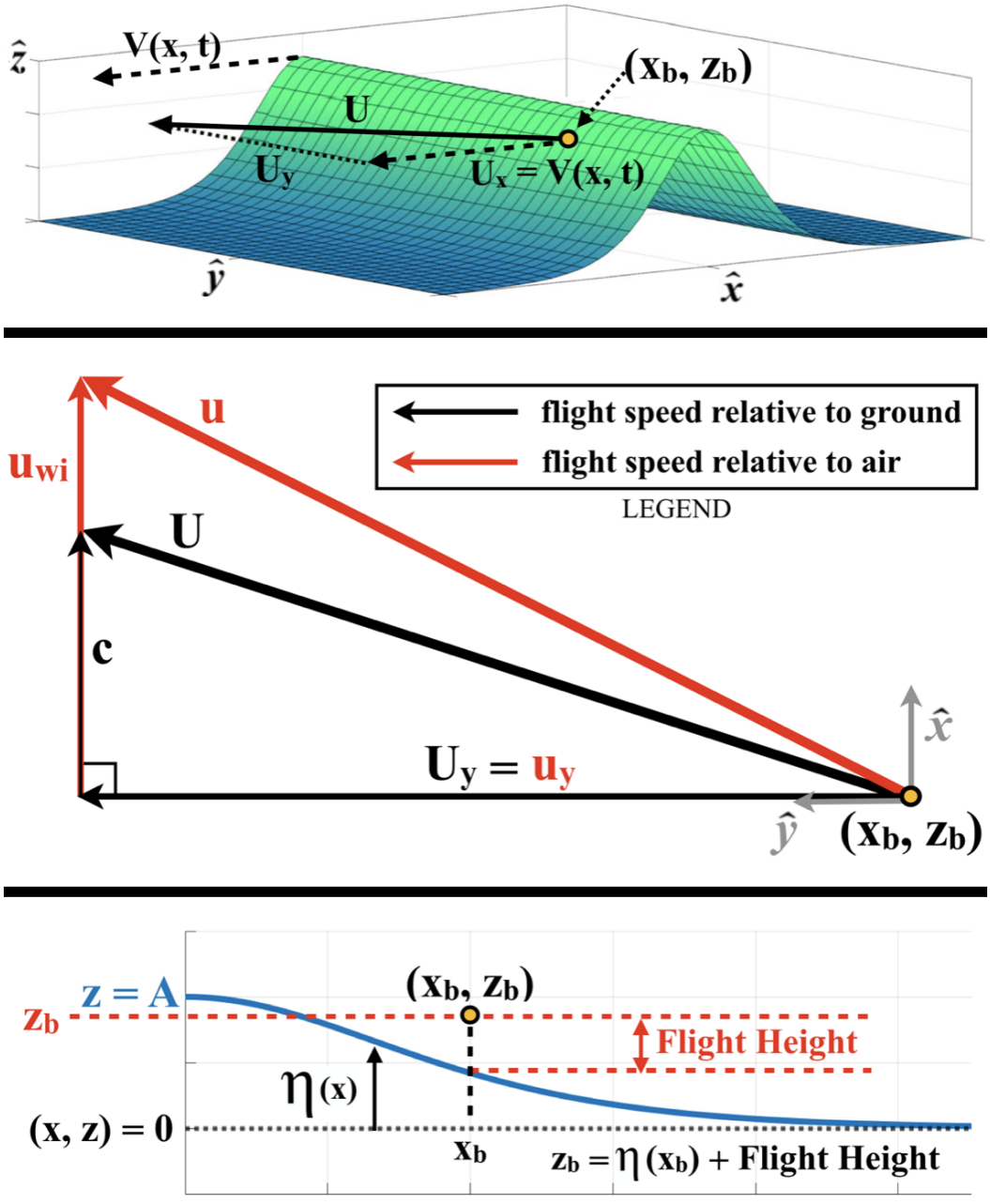

Figure 1.6: Top Panel: Coordinate system for the inertial trajectories of a pelican wave-slope soaring on a solitary wave. Middle Panel: Ground velocity vs. air velocity for wave-slope soaring and respective relations to phase velocity (c) and wave-induced wind (u_{wi}). Bottom Panel: Coordinate system for (x_b, z_b) in terms of $\eta(x)$ and bird's flight height.

using (1.2.2.4) and (1.2.2.5).

In setting $U_x = c$, it follows from Section 1.3 that the bird's airspeed in the direction of wave propagation (u_x) must then equate to the horizontal component of the wave-induced wind (u_{wi}) at the bird's location, shown in the middle panel of Figure 1.6. Because the components of groundspeed and airspeed in the along-wave-crest direction are equal (i.e. $U_y = u_y$, Fig. 6, middle panel), we can use the system's geometry to eliminate u_y and U_y. This allows us to write an expression for the groundspeed in terms of airspeed (u), phase velocity (c), and the horizontal component of the wave-induced wind (u_{wi}) as

$$U = \sqrt{u^2 + c^2 - u_{wi}^2}. \tag{1.2.4.1}$$

In (1.2.4.1), u_{wi} is a function of the spatial flight coordinates (x_b, z_b) i.e. $u_{wi} = u_{wi}(x_b, z_b)$.

To estimate (x_b, z_b), we impose the assumption that the bird will fly at the optimal location in the space above the wave for minimizing COT, and will remain at this location throughout soaring flight. Section 1.3 shows that the optimal flight location is directly over the inflection point of the wave surface, where the slope is the steepest. Accordingly, for the x coordinate of the bird's center of mass (x_b), we find the point of maximum slope associated with the waveform developed in Section 1.2. For the z coordinate of the bird's center of mass (z_b), we use the free surface elevation at this point of maximum slope, $\eta(x_b)$, calculated from (1.2.2.1) and add the case-respective flight height. A schematic of this procedure is displayed in the bottom panel of Figure 1.6

As the wavelength is large compared to the wingspan of the bird and the wave slope is small, we ignore variation of the wave-induced wind over the wingspan of the bird. The updraft component of the wind-field in (1.2.1.2) is driven solely by the wave, which with neglecting variation over wingspan justifies the use of a single value for w_u, as $w_u = w_{wi}$, in (1.2.1.2). Using the formalism developed in Section 1.3, w_{wi} is calculated from (1.2.3.18) using the coordinates (x_b, z_b) and case-respective wave parameters. Together with the substitution of (1.2.4.1) into (1.2.1.2) and using (1.2.3.17) to evaluate $u_{wi}(x_b, z_b)$, we estimate the COT in wave-

slope soaring, denoted $\mathcal{C}_{wss}$. This can be expressed as

$$\mathcal{C}_{wss} \approx \frac{Du - mgw_{wi}}{\sqrt{u^2 + c^2 - u_{wi}^2}}, \tag{1.2.4.2}$$

where D, u_{wi}, and w_{wi} are given by (1.2.1.1), (1.2.3.17), and (1.2.3.18) respectively, while c is given by evaluating (1.2.2.5) for h and substituting into (1.2.2.4).

Thus, we see that, for the simplifying assumptions we have made here, and ignoring ground-effect, we have an expression for the COT in WSS as a function of airspeed, wave height, wave period, flight location, and bird geometry, i.e.

$$\mathcal{C}_{wss} = \mathcal{C}_{wss}(u, A, T, x_b, z_b, \text{bird geometry}). \tag{1.2.4.3}$$

and is shown for a range of parameters in Figure 1.7.

1.3 Results

From our control, we find the minimum COT in steady, constant altitude pelican flight out of ground effect $\sim$ 1.5 J/m with a corresponding minimum cost velocity of $\sim$ 13.4 m/s (Fig. 1.2). When we consider ground effect flight for heights in the range reported by Hainsworth [1988], we find the COT is reduced by $\sim$ 15-25% to 1.1-1.3 J/m and the minimum cost velocity is decreased to $\sim$ 12 m/s (Fig. 1.3). A test case of WSS over a wave of 2 meters height with a 15 second period is used for consistency with a typical Southern California winter swell event Adams et al. [2008]. Under these conditions we estimate a large increases in energy savings in comparison to the control cases. Ignoring any benefit from GE, we find reductions in COT on the order of 70% for flight at 0.5m height, as compared to the 15% cost-benefit from GE at this height, shown in panel (a) of Figure 1.7. As expected, for lower flight heights and larger waves, the COT and minimum cost velocities are even further reduced. This is shown in panels (b) and (c) of Figure 1.7, respectively. Increasing the wave period does not monotonically decrease the COT. Though increasing the period increases the wave speed, it decreases the wave steepness, resulting in a nonlinear relationship between the wave's phase velocity and the updraft, headwind, and crosswind experienced by the bird. The result is

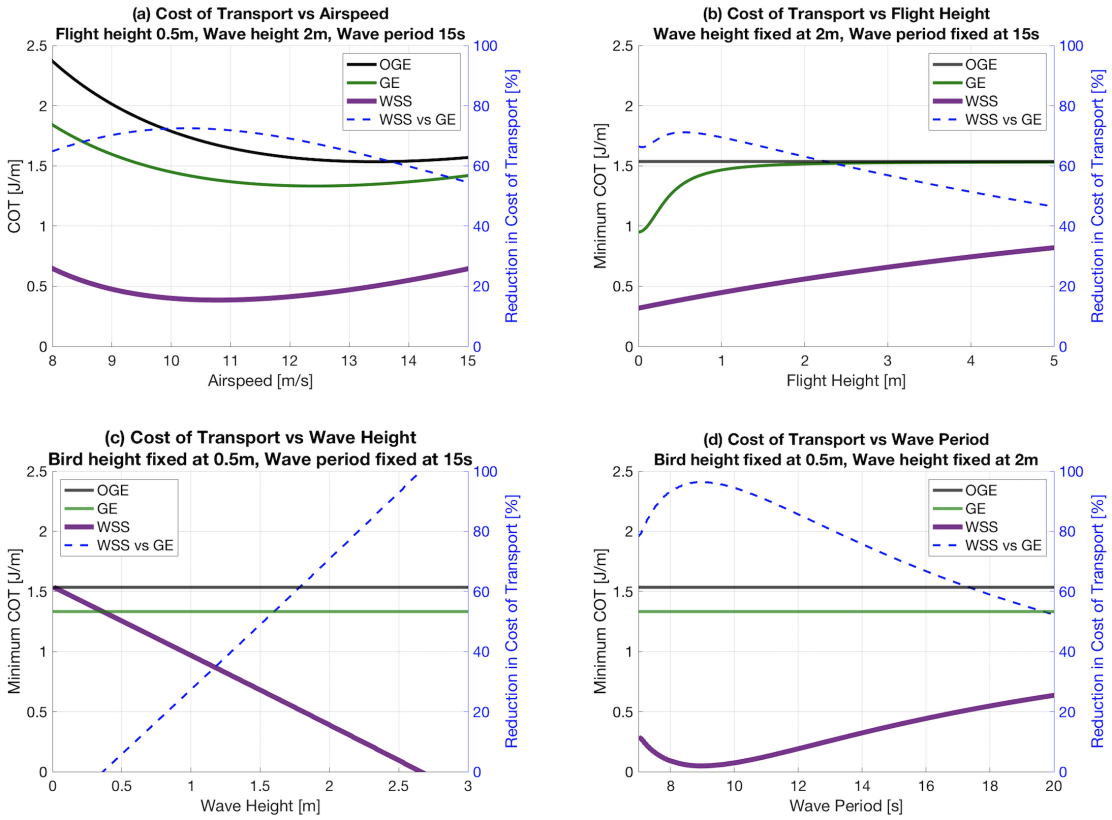

Figure 1.7: We explore the efficiency of wave slope soaring flight (WSS) under a range of environmental/flight conditions. In each panel, the corresponding percent reduction relative to flight in ground effect (GE) is shown in blue, with the right hand y-axis. (a) Cost of transport (COT) of WSS is shown for a range of airspeeds consistent with Pennycuick [1983], Schnell and Hellack [1978] in the default case of 0.5m bird height, 2m wave height, 15s wave period. (b) Minimum COT of WSS over a wave of 2m height, 15s period, varying flight height. (c) Minimum COT of WSS for 0.5m flight height over 15s period waves, varying wave height. (d) Minimum COT of WSS for 0.5m flight height over 2m high waves, varying wave period.

a maximum updraft at a relatively short period for a given wave height, shown in panel (d) of Figure 1.7.

1.4 Discussion

In the simplified case studied here, we show theoretically that wave-slope soaring can provide a considerable reduction in COT relative to steady, level flight in and out of ground effect. This may account for the widespread use of the behavior in the brown pelican that live in the coastal waters of Southern California.

There are several limitations of the theory presented here. We used the simplifying assumption of a weakly nonlinear solitary waveform. In reality, when observing pelicans employing wave-slope soaring, it is common for them to soar well into the surf zone, where nonlinearities become progressively stronger. In this regime, it becomes unreasonable to approximate the waveform as a soliton, and a more elaborate theory or numerical simulation would need to be employed. Added complications in the real world include the directional and frequency spread that characterizes ocean swell Fujiki et al. [2018], Montiel et al. [2018], Le Merle et al. [2019], Silva et al. [2020], and that shoaling waves tend to arrive in groups Mei [1989], Deike et al. [2017], Van Den Bremer et al. [2019], Buldakov et al. [2017], meaning that isolating the effect of a single wave may ignore an important effect of a train of waves shoaling in sequence.

The assumption of no ambient airflow in our model is another significant simplification. Our solution is framed around the benefit of vertical flow in the atmosphere perturbed by a travelling wave, which would be altered as ambient wind speeds increase, potentially increasing vertical velocities near the wave face Tamura et al. [2018]. However, the development of a turbulent boundary layer that tends toward separation between wave-crests is known to occur in moderate and strong wind scenarios Banner and Melville [1976], Husain et al. [2019], Buckley and Veron [2019]. This renders the inviscid simplification that underpins the potential flow solution invalid.

Perhaps turbulent airflow over ocean waves is not amenable to wave-slope soar-

ing. In the Southern Ocean, wave-slope soaring in albatrosses is only observed during rare calm periods Richardson [2011]. This suggests that as the boundary layer becomes turbulent, dynamic soaring is a more effective strategy. A separated, turbulent boundary layer may be less amenable to wave-slope soaring since updrafts associated with traveling waves may be reduced in magnitude or lose coherence in time or along the wave crest, which is the primary direction of travel.

High-resolution numerical simulations capable of representing the full response of the atmosphere to ocean waves are now being used to study air/sea interactions Semedo et al. [2009], Buckley and Veron [2016], Sullivan et al. [2008], Semedo et al. [2015], Druzhinin et al. [2012]. These simulations, if verified by future field observations, allow a 3-D and time varying wind field to be calculated for different forcing scenarios that would be of great utility for examining the aerodynamics of wave-slope soaring. Similarly, individual brown pelicans tagged with inertial measurement units and fast-rate GPS positions would allow for the flight behavior of wave-slope soaring to be better quantified Bouten et al. [2013], Treep et al. [2016], Williams et al. [2018]. In particular, time-series measurements of accelerations and air-speed could be used to quantify the forces acting during wave-slope soaring behavior Bouten et al. [2013], Elliott et al. [2013], Leos-Barajas et al. [2017], Takahashi and Shimoyama [2018]. Further investigation of wave-slope soaring is not relevant only to the ecology of seabirds, but in the future may be one of a suite of environmental scenarios in which unmanned aerial vehicle control systems can maximize flight endurance using environmental energy Bonnin et al. [2015], Deittert et al. [2009], Zhao and Qi [2004], Zhu et al. [2020], Jiakun et al. [2020].

1.5 Conclusions

The theoretical framework presented here suggests that brown pelicans could reduce the energetic demands of gliding flight by $\sim$ 60-70% via utilizing wave-slope soaring during periods of weak winds. Although there must be some risk associated with flying at a relatively high speed very close to an undulating and evolving surface, the benefit in terms of efficiency of apparently favors the behavior.

Surfing of shoaling and breaking waves has been documented in several species of marine mammals, wherein it is assumed that the activity represents play Paulos et al. [2010]. Brown pelicans, on the other hand, may leverage their ability to ride waves for long-distance travel, since flight allows them to connect a set of multiple shoaling waves in sequence. This allows continuous wave-riding for periods of minutes, and may account for travel of kilometers up or down the coast. Cost-effective travel resulting from wave-slope soaring behavior may have an important impact on the foraging range and foraging strategy of these ecologically important creatures.

1.6 Declarations

1.6.1 Dedication

We dedicate this manuscript to the late Ken Melville of Scripps Institution of Oceanography–a pioneer in the study ocean surface waves and air-sea interactions–for his suggestion on use of the soliton formalism to represent near-shoaling, shallow water, ocean surface gravity waves.

1.6.2 Ethics approval and consent to participate

Not applicable

1.6.3 Consent for publication

Not applicable.

1.6.4 Availability of data and material

Not applicable.

1.6.5 Competing interests

The authors declare that they have no competing interests.

1.7 Funding

AJL gratefully acknowledges the Office of Naval Research (ONR) Young Investigator Program Fellowship (ONR N00014-17-1-2987) for supporting this effort. IAS was supported by ONR grant (ONR N00014-17-1-2112).

1.7.1 Author's contributions

IAS developed the mathematical formalism central to the manuscript. Both authors contributed to framing the problem, developing the approach here, and writing the manuscript. This manuscript began as a Masters thesis for IAS at the Department of Mechanical and Aerospace Engineering at the University of California, San Diego.

1.7.2 Acknowledgements

We would like to thank Benjamin Monreal of Case Western Reserve University for introducing the us to the problem, as he observed pelicans wave-slope soaring during his years at the University of California, Santa Barbara, and noted that no proper theoretical solution existed in the literature. After reviewing the initial sketch up of the problem, Anthony Zee of the Kavli Institute of Theoretical Physics at the University of California, Santa Barbara expressed interest, encouraging us to extend the theory and analysis into a manuscript. Stefan Llewellyn-Smith and Bill Young at the University of California, San Diego, aided in the refinement of the mathematical methods used in this work. We further thank Stefan Llewellyn-Smith and two anonymous reviewers for providing useful feedback on the manuscript. Simone Staff generously provided us with the image in Figure 1.1, for which we are grateful.

Chapter 1, in full, is a reprint of the material as it appears in Wave-slope soaring of the brown pelican, Movement Ecology. Ian A. Stokes, Andrew J. Lucas; *Published* 2021. The dissertation author was the primary investigator and author of this paper.

Chapter 2

A generalized slab model

2.1 Introduction

The oceanic surface boundary layer (OSBL) plays a key role in energy exchange between the atmosphere and ocean [Grachev and Fairall, 2001]. Wind imposes shear stress on the OSBL which drives surface waves and turbulent mixing in the upper ocean. With time, a mixed layer (ML) develops that extends downward from the ocean surface. The ML is a ubiquitous feature of the OSBL, characterized by an approximately homogeneous region with small vertical gradients in temperature and salinity that exists between the ocean's surface and the stratified interior [Brainerd and Gregg, 1995]. The thickness of the ML varies globally and is generally largest during the winter and in energetic regions [Holte et al., 2017]. Beneath the ML stratification increases rapidly with depth, from a value near zero in the ML to a maximum value in the interior. This region of strong stratification gradients is the transition layer (TL) and marks the base of the OSBL [D'Asaro et al., 1995, Johnston and Rudnick, 2009, Kaminski et al., 2021]. The TL plays the important role of modulating interactions between the ML and the interior. For example, entrainment processes which enable momentum and property exchange between the OSBL and the interior are initiated in the TL and ultimately lead to ML deepening [Grant and Belcher, 2011]. In the analysis that follows, we investigate how variability in the TL modulates the atmosphere's ability to supply power to the internal wave field.

Wind stress acting on the ocean surface is estimated to supply 0.27-1.4 TW of power input to the near-inertial internal wave field globally [e.g., Wunsch, 1998, Alford, 2001, Watanabe and Hibiya, 2002, Furuichi et al., 2008, Rimac et al., 2013, Alford, 2020a]. Though these numbers only represent a small fraction of the total power input by the atmosphere into the ocean [Wunsch, 1998, Zippel et al., 2022], energy in the internal wave band propagates vertically, creating a pathway for energy from the atmosphere to penetrate deep into the ocean's interior [Gill, 1982, Alford et al., 2012]. The path begins with near-inertial oscillations (NIOs) of the ML. These oscillations are the ocean's local response to wind-forcing, and the frequency is set by the local Coriolis frequency [Plueddemann and Farrar, 2006]. Zonal gradients in wind stress produce variability in the intensity of NIOs, setting up regions of convergence and divergence which resonantly pump the base of the ML at the inertial frequency. This pumping action converts the inertial oscillations into near-inertial internal waves [NIWs, Gill, 1984]. Meridional variability of the Coriolis effect [i.e., the β-effect: D'Asaro, 1989, D'Asaro et al., 1995, Moehlis and Llewellyn Smith, 2001]) and the submesoscale eddy field [e.g., Asselin et al., 2020, Thomas et al., 2020] set up lateral gradients in the local vorticity which also generate NIWs. This process analogously produces convergence, but it is imposed by phase variability between adjacent NIOs rather than intensity variability [Young and Ben Jelloul, 1997]. Fast moving storms [e.g., Gill, 1984, D'Asaro et al., 1995, Brizuela et al., 2022] and interactions with coastlines [e.g., Pettigrew, 1981, Millot and Crépon, 1981, Kundu et al., 1983, Kelly, 2019]) can convert these oscillations into NIWs as well.

Alford and Whitmont [2007] and Silverthorne and Toole [2009] show that NIWs dominate internal wave kinetic energy and shear spectra at all depths throughout the global ocean. Observations of inertial kinetic energy (IKE) and ocean mixing show coherent seasonal variability, supporting the hypothesis that NIWs contribute strongly to ocean mixing [Alford, 2020a]. Thus there is substantial evidence indicating the importance of NIWs as a means for energy from the atmosphere to reach the deep ocean. Because NIWs arise from NIOs, the potential for the generation of NIWs is set by the wind's ability to supply power to NIOs. This power input is

often referred to as the "wind work" in the literature, and denoted Π (note that 'wind work' is actually power input with units of W/m^2). Π sets bounds on NIW generation and is of first order importance for energy transfer from the atmosphere to the ocean's interior.

The slab model, introduced by Pollard and Millard [1970], is a common method for global wind work estimation [e.g., Alford, 2001]. The slab model operates on the simplified view that the OSBL is a homogeneous ML that responds to wind stress as a solid body. In this formulation, all of the momentum imparted by the wind is deposited in the ML, and there are no currents below. For the solid-body-ML assumption of the slab model to hold, there must exist a step-like change in stratification at the base of the ML so that the TL thickness is negligible compared to the ML thickness. What results is a linear stress profile with a step-like vertical stress gradient, mirroring the ML's step-like stratification (Figure 2.1).

Slab models perform well in some cases [e.g., Pollard and Millard, 1970], but cannot always reproduce observations [Niiler, 1975, Alford, 2020a]. Plueddemann and Farrar [2006] show how turbulent entrainment by inertially generated shear at the base of the ML leads to ML deepening, which cannot be resolved in a slab model. As a consequence, momentum is concentrated in the ML, leading to an overestimation of inertial currents and wind work.

During the MIxed Layer Experiment (MILE), Davis et al. [1981] observed upper ocean shear development in response to wind stress and found that the behavior deviated considerably from the slab flow approximated by Pollard and Millard [1970]. These observations showed momentum diffusion into the TL beneath the ML. D'Asaro et al. [1995] also observed nonzero inertial currents beneath the ML during the Ocean Storms experiment, which are consistent with a three-layer model consisting of a ML, a TL, and a stratified interior. D'asaro [1995] reproduced the observed inertial currents by vertically redistributing the wind stress using a body force consistent with a linear stress profile in the ML and a quadratic stress profile in the TL. We refer to this model of the upper-ocean stress as the 'MLTL' model.

D'asaro [1995]'s empirical method of tuning the forcing stress (body force) successfully replicated the ML and TL currents during the Ocean Storms experiment.

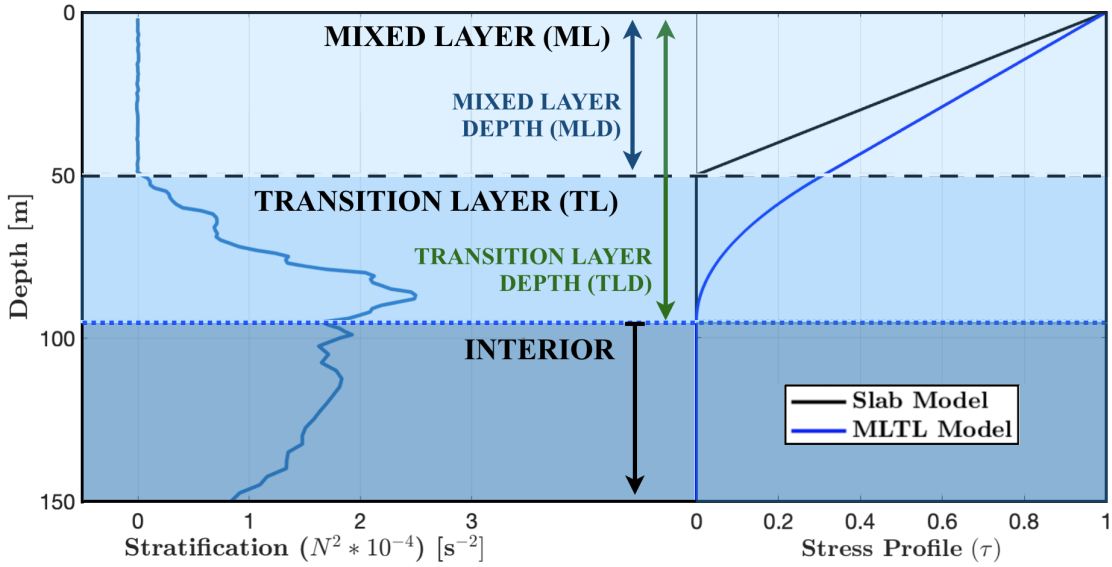

Figure 2.1: A schematic is shown for an example ML, TL, and the associated stratification and stress profiles. **Left-hand axes:** Stratification data from a high resolution Argo float in the Pacific Ocean on 2020/01/01 at 49.4 N, 129.3 W. The mixed layer depth (MLD) and transition layer depth (TLD) are calculated from the stratification data. MLD is calculated using the density method of Holte and Talley [2009] to be 50 m. TLD is calculated using the local minimum method of Sun et al. [2013] to be 95 m. Transition layer thickness (TLT) determined as TLD - MLD = 45 m. In this case, we have a relative transition layer thickness (TLT/MLD) of 0.9. The stratification data shown has been smoothed with a 15 point moving mean. **Middle axes:** The stress profiles associated with the slab model and MLTL model are plotted vs. depth in black and blue, respectively. The slab stress profile is linear, and only nonzero within the ML. The MLTL stress profile is nonlinear, and has nonzero components in both the ML and TL. Expressions for the vertical dependence of these profiles are derived in the Appendix and given by (2.6.3.1) and (2.6.3.2), respectively.

To generalize a tuning method, stratification based methods are needed to objectively define the ML, TL, and stratified interior. Johnston and Rudnick [2009] and Sun et al. [2013] built on D'Asaro et al. [1995]'s work by developing rigorous methods for determining the TL thickness (TLT). Johnston and Rudnick [2009] shows that the TL can be resolved by using either fine-scale shear or fine-scale stratification profiles. Sun et al. [2013] endorse the stratification approach to determining the base of the TL and define the TL as a region that extends from the base of the ML to a depth just below the maximum value of stratification. This TL depth (TLD) is selected by choosing the shallower of either a local minimum in stratification or an 'abrupt change in slope' below the maximum stratification value. To avoid ambiguity associated with the latter definition, we use the local minimum method as the primary means to determining the base of the TL. If there is no local minimum in the neighborhood of the maximum, the depth of maximum stratification is used in an effort to keep the estimation of TLT conservative. A schematic for this setup that includes the stress profiles of both the slab and MLTL model with corresponding stratification is shown in Figure 2.1. In this example stratification profile, the local minimum and slope methods both produce the same value for the base of the TL.

Observations show that the thickness of the TL can be equal to or greater than that of the ML [e.g., Sun et al., 2013], making the traditional slab model a poor approximation for the OSBL [see Figure 2.1 and D'Asaro et al., 1995, Grant and Belcher, 2011]. However, the impact of TLs on wind work and energetics have not been explicitly quantified. TLs substantially alter the vertical structure of near-inertial currents [D'Asaro et al., 1995, Dohan and Davis, 2011]. They mix momentum downward, reducing surface currents and, hence, wind work. This study develops a generalized slab model that allows for arbitrary depth-varying forcing stress profiles in the OSBL, which may be parameterized to match observations of the TL. We then analyze how the stress profile affects wind work. As a first-order improvement on the stress profile used in the traditional (ML) slab model, we add a TL using the three-layer piecewise-nonlinear MLTL model from D'Asaro et al. [1995]. The MLTL model is still an idealized representation of the

turbulent OSBL, but it provides the simplest estimate of how the TL affects wind work.

This article is organized into three parts: theoretical development of the generalized slab model, an in situ comparison of data with the generalized slab model and the traditional slab model, and a global analysis where the large-scale significance of the TL is evaluated. In section 2.2, we present the physics upon which our model is based. An insight here is a proof of how nonlinear forcing stress profiles lead directly to TKE production, thus limiting the ability of wind stress to power inertial motions. We apply these ideas to the Iceland Basin (sec 2.32.3.1) by comparing our model with observations from NISKINe (Near-Inertial Shear and KInetic eNergy experiment). We extend the model to global analyses (sec 2.32.3.2) by using high-resolution Argo autonomous profiling float observations to calculate a global climatological atlas of TLT. Coupling the TLT atlas with ML climatologies of Holte et al. [2017] provides a global set of MLTL stress profiles, which allow us to quantitatively estimate how TLs impact wind work globally.

2.2 Methods

2.2.1 Theory

Governing equations

Our goal is to assess the impact of vertical stress profiles on wind work calculations using a simplified dynamical model. The linear momentum equations governing the ocean's response to stress, ignoring pressure gradients and buoyancy forcing, are

$$\frac{\partial \mathbf{u}}{\partial t} + f\hat{\mathbf{k}} \times \mathbf{u} = \frac{\partial \boldsymbol{\tau}}{\partial z}, \tag{2.2.1.1}$$

where $\mathbf{u}$ is the velocity, f is the local Coriolis parameter, $\hat{k}$ is the unit normal vector, and $\boldsymbol{\tau}$ is the total stress, normalized by a reference density, ρ_0. As we are primarily interested in inertial motions, we apply a high-pass filter to the forcing term in order to remove Ekman effects [D'Asaro, 1985]. The stress gradient profile

provides the forcing and damping in (2.2.1.1) and is

$$\frac{\partial \boldsymbol{\tau}}{\partial z} = \frac{\partial}{\partial z}\left(\nu \frac{\partial \mathbf{u}}{\partial z} - \overline{w'\mathbf{u}'}\right). \tag{2.2.1.2}$$

The second term on the right-hand side, $\overline{w'\mathbf{u}'}$, is the turbulent Reynolds stress, which dominates over the first term (the viscous stress, kinematic viscosity ν) in the ocean [Gargett, 1989]. The Reynolds stress depends on all of the turbulent processes in the OSBL and is difficult to measure directly [Bian et al., 2018, Huang and Qiao, 2021]. The stress can be modeled via direct numerical simulations (DNS) and large eddy simulations (LES) [e.g., Skyllingstad et al., 2023], but these are too computationally expensive for regional or global circulation models, which rely on simpler 1D turbulence closure models [e.g., Large et al., 1994, Umlauf and Burchard, 2005]. Thus, turbulence models either require high-resolution numerical grids or ad hoc parameter tuning. An alternative approach is to tune a simple conceptual model of the stress profile to fit and interpret observations [D'asaro, 1995, Plueddemann and Farrar, 2006, Alford, 2020a, Zippel et al., 2022]. Here, we present a simple model to interpret how observed TLs alter wind work. Following D'Asaro et al. [1995], Plueddemann and Farrar [2006], and Alford [2020a], we separate stress into components due to direct wind forcing and inertial damping

$$\frac{\partial \mathbf{u}}{\partial t} + f\hat{\mathbf{k}} \times \mathbf{u} = \frac{\partial \boldsymbol{\tau}_w}{\partial z} + \frac{\partial \boldsymbol{\tau}_r}{\partial z}\,. \tag{2.2.1.3}$$

The first term, $\partial \boldsymbol{\tau}_w / \partial z$, parameterizes all of the turbulent motions in the OSBL that rapidly inject wind momentum downward, such as breaking waves, Langmuir turbulence, entertainment, Stokes drift, and shear instability of the total wind-driven flow. This term may be interpreted as the body force exerted by the wind on the inertial flow [D'asaro, 1995]. The second term, $\partial \boldsymbol{\tau}_r / \partial z$, parameterizes all of the turbulent motions that specifically damp the inertial flow, which includes stratified shear instability (due to the inertial flow), bottom drag, and wave drag due to internal wave radiation [Plueddemann and Farrar, 2006].

We obtain an energy balance by taking (2.2.1.3)$\cdot\mathbf{u}$ and depth integrating over

the ocean depth H:

$$\frac{\partial}{\partial t}\underbrace{\left(\int_{-H}^{0}\frac{|\mathbf{u}(z)|^2}{2}\mathrm{d}z\right)}_{\mathrm{IKE}} = \underbrace{[\boldsymbol{\tau}_w\cdot\mathbf{u}]_0}_{\Pi_{tot}} - \underbrace{\int_{-H}^{0}\boldsymbol{\tau}_w\cdot\frac{\partial\mathbf{u}}{\partial z}\mathrm{d}z}_{P_{TL}} - \underbrace{\int_{-H}^{0}\boldsymbol{\tau}_r\cdot\frac{\partial\mathbf{u}}{\partial z}\mathrm{d}z}_{P_R} - \underbrace{[\boldsymbol{\tau}_r\cdot\mathbf{u}]_{-H}}_{P_B}, \tag{2.2.1.4}$$

where we have expanded the stress-gradient terms using integration by parts, assuming $\boldsymbol{\tau}_w$ is zero at the bottom and $\boldsymbol{\tau}_r$ is zero at the surface. The Coriolis term, $f(\hat{k}\times\mathbf{u})\cdot\mathbf{u}=0$, does no work. The kinetic energy (KE) budget indicates that the time rate-of-change of the inertial kinetic energy (IKE; left-hand side) is set by the balance between the total power input by wind-stress (Π_{tot}, "total wind work") and turbulent kinetic energy (TKE) production, P. The sources of TKE production are forcing stress in the TL (P_{TL}), internal damping stresses (P_R), and bottom stress (P_B). We emphasize that P_{TL} is zero in a traditional slab model because forcing stress is confined to the ML, where shear is zero. We also note that P_B can typically be neglected in the deep ocean, but may be appreciable near coastlines or otherwise shallow bathymetry.

TKE production in the TL

Shear production ($P_{TL}+P_R$) is a positive quantity that is a sink in (2.2.1.4) and a source term in the TKE equation [Tennekes and Lumley, 1972]. TKE production only occurs where the curvature in the stress profile produces velocity shear. Traditional slab models assume a linear forcing-stress profile through the ML [Pollard and Millard, 1970], which produces no shear and no TKE production. Instead, energy is extracted from the flow by parameterzing the damping stress with a Rayleigh drag, $\partial\boldsymbol{\tau}_r/\partial z\approx -r\mathbf{u}$, which represents the combined effects of entrainment, convective-shear instability, wave radiation, and bottom drag [Moehlis and Llewellyn Smith, 2001, Plueddemann and Farrar, 2006, Kelly, 2019].

Price et al. [1986] used the same forcing stress profile as Pollard and Millard [1970], but substantially improved the parameterization of the damping stress. Their numerical model, Price-Weller-Pinkel (PWP), is a well-accepted 1D quasi-bulk dynamical instability ML model available for estimating vertical mixing in the TL and the atmospheric power input to inertial motions [Alford, 2020b]. The

PWP model is widely used in large-scale global ocean models [e.g., HYbrid Coordinate Ocean Model, 'HYCOM;' Chassignet et al., 2007] when more accurate parameterizations [e.g., KPP; Large et al., 1994] become too computationally expensive. PWP deepens the ML using a bulk Richardson number parameterization for entrainment, and accounts for TKE shear production by parameterizing stratified-shear instability of the inertial flow in the TL using the gradient Richardson number. Unstable patches are partially mixed, which smooths the velocity profile, removes kinetic energy, and transfers momentum from the ML to the TL. Plueddemann and Farrar [2006] and Alford [2020a] show that PWP agrees better with observations than traditional slab model estimates.

The generalized slab model presented here differs from the traditional slab model and PWP because it allows for an arbitrary profile of forcing stress that can extend into the TL. That is, it relaxes the traditional slab-model assumption that momentum from the wind is uniformly deposited throughout the ML. This modification is motivated by observations that the actively mixing layer, as defined by TKE dissipation, often differs from the ML, as defined by the density profile [Brainerd and Gregg, 1995]. With the generalized slab model, one is free to specify a forcing stress profile that was observed during a storm or modeled using LES. Moreover, one can simply specify a forcing stress profile that directly reproduces observed vertical shear in the TL [D'asaro, 1995] without having to resolve the turbulent dynamics of the OSBL.

In the analyses here, we use the MLTL forcing stress profile because it is the simplest model that produces shear in the TL (Fig. 2.1). The MLTL model can be combined with any model of damping stress. For computational simplicity, we use a tunable Rayleigh drag to parameterize unresolved damping stresses that depend on the strength of the inertial currents. A catch-all Rayleigh damping was also added to PWP by Plueddemann and Farrar [2006] and tuned to improve agreement with observations.

The direct generation of TKE shear production by forcing stress in the TL (P_{TL}) is a feature of the generalized slab model that is absent in the traditional slab model. Previous models which lump TKE production into P_R require that

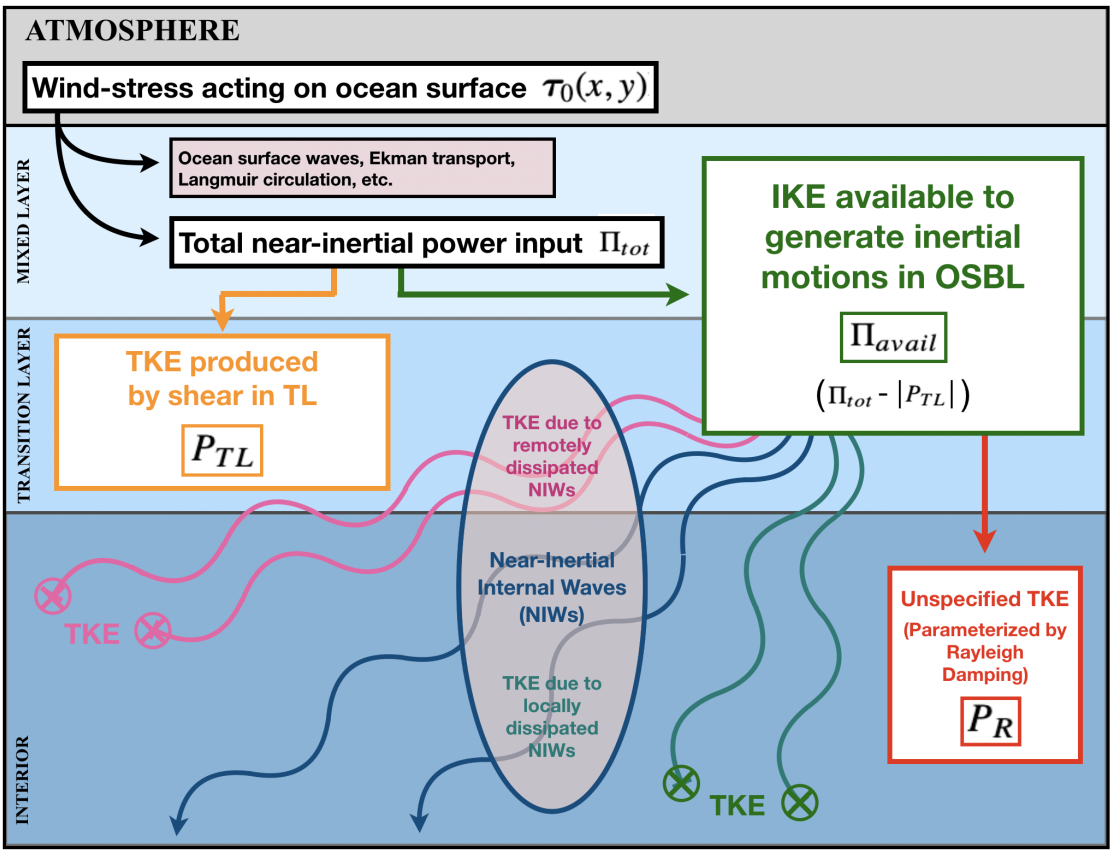

Figure 2.2: A flow chart is provided to visualize the pathways energy can take from wind in the atmosphere to mixing. The y-axis is correlated to ocean depth, and is superposed on a layered model of the atmosphere-ocean system (layers in descending order are atmosphere, ML, TL, interior). Boxes indicate processes in play, and box positions indicate which layer(s) the processes act on. The vertical positions of boxes within each layer are arbitrary. Processes highlighted in red are included for completeness, but not specifically addressed in the paper.

the OSBL already be in motion ($\mathbf{u} \neq 0$) in order to generate TKE. They may also underestimate P_R if momentum is mixed through the OSBL by turbulence that is not directly associated with the inertial flow (e.g., wave breaking, Langmuir turbulence, etc.). In the generalized slab model, P_{TL} is a direct function of the wind stress, so that TKE shear production occurs as soon as the wind blows, provided that the forcing stress profile has curvature. Thus, one may think of curvature in the forcing stress profile as a distinct pathway for TKE shear production in the ocean (Fig. 2.2).

2.2.2 Solution via decomposition into normal modes

In this section we present a method to solve the governing equations derived in Section 2.22.2.1. In our generalized slab model, we allow for an *arbitrary, depth-variable* forcing stress profile, making analytical solutions in Cartesian coordinates difficult. We resolve this issue by employing the modal decomposition of Gill and Clarke [1974]. For each mode, we recover the simple damped oscillator equation, analogous to Pollard and Millard [1970]. Summing over all modes reconstructs the velocity profile that is generated by an arbitrary forcing stress profile.

Modal decomposition

Horizontal baroclinic velocity, $\mathbf{u}(\mathbf{x}, z, t) = [u(\mathbf{x}, z, t), v(\mathbf{x}, z, t)]$, is expressed as sum of orthogonal vertical modes

$$\mathbf{u}(\mathbf{x}, z, t) = \sum_{n=1}^{\infty} \mathbf{u}_n(\mathbf{x}, t)\phi_n(z) \ , \tag{2.2.2.1}$$

where $\mathbf{x} = [x, y]$, z, and t are horizontal, vertical, and time coordinates, $\mathbf{u}_n(\mathbf{x}, t)$ is the velocity modal amplitude, n is the vertical mode number, and $\phi_n(z)$ is the vertical mode [Kelly, 2016]. The modes satisfy

$$\frac{\mathrm{d}^2\Phi_n}{\mathrm{d}z^2} + \frac{N^2}{c_n^2}\Phi_n = 0, \qquad \text{with} \qquad \Phi_n(0) = \Phi(-H) = 0, \tag{2.2.2.2a}$$

and

$$\frac{\mathrm{d}}{\mathrm{d}z}\left(\frac{1}{N^2}\frac{\mathrm{d}\phi_n}{\mathrm{d}z}\right) + \frac{1}{c_n^2}\phi_n = 0, \qquad \text{with} \qquad \left.\frac{\mathrm{d}\phi_n}{\mathrm{d}z}\right|_0 = \left.\frac{\mathrm{d}\phi_n}{\mathrm{d}z}\right|_{-H} = 0, \tag{2.2.2.2b}$$

where $\phi_n = \mathrm{d}\Phi_n/\mathrm{d}z$, c_n is the eigenspeed of mode n, and N is the buoyancy frequency. In practice (2.2.2.2) is solved numerically using climatological stratification. The modes are orthogonal such that

$$\int_{-H}^{0} \Phi_m \frac{N^2}{c_m c_n} \Phi_n \mathrm{d}z = H\delta_{mn}, \qquad \text{and} \qquad \int_{-H}^{0} \phi_m \phi_n \mathrm{d}z = H\delta_{mn} \; . \tag{2.2.2.3}$$

Multiplying (2.2.1.3) by ϕ_n and depth integrating yields the momentum equation for the nth mode,

$$\frac{\partial \mathbf{U}_n}{\partial t} + f\hat{\mathbf{k}} \times \mathbf{U}_n = \boldsymbol{\tau}_n^w - r\mathbf{U}_\mathbf{n}, \tag{2.2.2.4}$$

where $\boldsymbol{\tau}_n^w$ is the projection of the forcing stress onto mode n and the modal transports are simply $\mathbf{U}_n = H\mathbf{u}_n$.

Forcing stress parameterization

The modal forcing stress is

$$\boldsymbol{\tau}_n^w = \int_{-H}^{0} \frac{\partial \boldsymbol{\tau}_w}{\partial z} \phi_n \mathrm{d}z. \tag{2.2.2.5}$$

At any given time and place, the forcing stress may be written as $\boldsymbol{\tau}_w = \boldsymbol{\tau}_0 \Sigma(z)$, where $\boldsymbol{\tau}_0$ is the surface wind stress and $\Sigma(z)$ is the forcing profile with $\Sigma(0) = 1$. Modal forcing can then be written as

$$\boldsymbol{\tau}_n^w = \boldsymbol{\tau}_0 \phi_{ns} \qquad \text{with} \qquad \phi_{ns} = \int_{-H}^{0} \frac{\partial \Sigma}{\partial z} \phi_n \mathrm{d}z \; . \tag{2.2.2.6}$$

In general, both the wind stress, $\boldsymbol{\tau}_0$, and forcing profile, $\Sigma(z)$, evolve in time. Strong forcing alters the ML and TL depths through turbulent entrainment and mixing [Price et al., 1986]. In the analyses here, we use static ML and TL depths based on observations and climatology. This assumption is valid for moderate winds and short-duration simulations over days to weeks. If longer simulations are desired, say weeks to months, the stress profile can be updated during forward time stepping.

When $\Sigma(z)$ is constant in time and all modes are damped with the same r, the modal transports are proportional to the total transport, $\mathbf{U}_n = \mathbf{U}\phi_{ns}$, where the total transport equation is

$$\frac{\partial \mathbf{U}}{\partial t} + f\hat{\mathbf{k}} \times \mathbf{U} = \boldsymbol{\tau}_0 - r\mathbf{U} \; . \tag{2.2.2.7}$$

We solve this equation numerically by specifying a wind stress time series, damping coefficient, and inertial frequency, and using a convolution method consistent with Gupta et al. [2019]. We can then obtain modal amplitudes by specifying a vertical stress profile, $\Sigma(z)$, computing ϕ_{ns} from (2.2.2.6), and using $\mathbf{U}_n = \mathbf{U}\phi_{ns}$.

Wind work calculations

Nomenclature: In the traditional slab model, "wind work" describes the power input by the wind to inertial motions in the OSBL. Because TKE production in the traditional slab is related to Rayleigh drag, the damping can only dissipate motions which have already been generated by the wind. Thus the damping does not affect the "power input", only the decay rate, so the names "wind work" and "power input" can be used interchangeably. However, in the generalized slab model, some TKE production is associated with the wind itself (P_{TL}). This TKE production inhibits the acceleration of inertial motions, and accordingly reduces the net work on inertial motions. Specifically, some fraction of the total power input is immediately diverted to TKE production in the TL, while the remainder excites inertial motions. We refer to these quantities as the "TKE fraction" ($\mathcal{P} = P_{TL}/\Pi_{tot}$) and "available wind work" ($\Pi_{avail} = \Pi_{tot} - P_{TL}$), respectively. Since P_{TL} is positive semi-definite, available wind work is always less than or equal to total wind work.

Total wind work: From (2.2.1.4), the total wind work, (Π_{tot}) is given by $[\boldsymbol{\tau}_w \cdot \mathbf{u}]_{z=0}$ and can be expressed as

$$\Pi_{tot} = \boldsymbol{\tau}_0 \cdot \mathbf{u}_{\text{surf}}, \tag{2.2.2.8}$$

where the surface velocity can be written as a sum of modes,

$$\mathbf{u}_{\text{surf}} = \frac{1}{H}\sum_{n=1}^{\infty} \mathbf{U}_n \phi_n(0) = \frac{\mathbf{U}}{H}\sum_{n=1}^{\infty} \phi_{ns}\phi_n(0)\ . \tag{2.2.2.9}$$

and the total wind work as

$$\Pi_{tot} = \frac{\boldsymbol{\tau}_0 \cdot \mathbf{U}}{H}\sum_{n=1}^{\infty} \phi_{ns}\phi_n(0). \tag{2.2.2.10}$$

Available wind work: The net wind work on each mode (Π_n) is given by Alford [2020b] as

$$\Pi_n = \boldsymbol{\tau}_n^w \cdot \mathbf{u}_n. \tag{2.2.2.11}$$

Substituting $\boldsymbol{\tau}_n^w = \boldsymbol{\tau}_0 \phi_{ns}$ and $\mathbf{u}_n = \mathbf{U}\phi_{ns}/H$ and summing over all modes yields

$$\Pi_{avail} = \frac{\boldsymbol{\tau}_0 \cdot \mathbf{U}}{H} \sum_{n=1}^{\infty} \phi_{ns}^2. \tag{2.2.2.12}$$

TKE production: The TKE production in the TL is computed by rearranging $\Pi_{avail} = \Pi_{tot} - P_{TL}$ and using the expressions above

$$P_{TL} = \frac{\boldsymbol{\tau}_0 \cdot \mathbf{U}}{H} \sum_{n=1}^{\infty} \phi_{ns} \left[\phi_n(0) - \phi_{ns}\right]. \tag{2.2.2.13}$$

TKE fraction: The fraction of Π_{tot} which is diverted to TKE production ($\mathcal{P} = P_{TL}/\Pi_{tot}$) can be written using (2.2.2.10) and (2.2.2.13) so that it doesn't depend on wind stress

$$\mathcal{P} = 1 - \frac{\sum_n \phi_{ns}^2}{\sum_n \phi_{ns}\phi_n(0)}\ . \tag{2.2.2.14}$$

$\phi_n(0)$ only depends on observed or climatological stratification (N^2) and ocean depth via (2.2.2.2). ϕ_{ns} additionally depends on the forcing stress profile, $\Sigma(z)$, via (2.2.2.6). This means that with stratification, ocean depth, and an inferred (or measured) stress profile, we can estimate the ratio of TKE production to inertial oscillation generation without explicitly knowing the wind. However, the wind sets the forcing stress profile, and this profile changes as the OSBL structure evolves (e.g., strong wind can deepen the ML). Thus, our analyses are only suitable for isolated wind events that do not strongly alter the structure of the OSBL. For stronger storms and longer integrations, temporally evolving stress profiles [$\Sigma(z) \longrightarrow \Sigma(z,t)$] can be used in the same way that traditional slab models have incorporated time-dependent MLD [D'Asaro, 1985].

2.3 Results

We use both local and global observational datasets to assess the differences between the generalized slab model, the traditional slab model of Pollard and

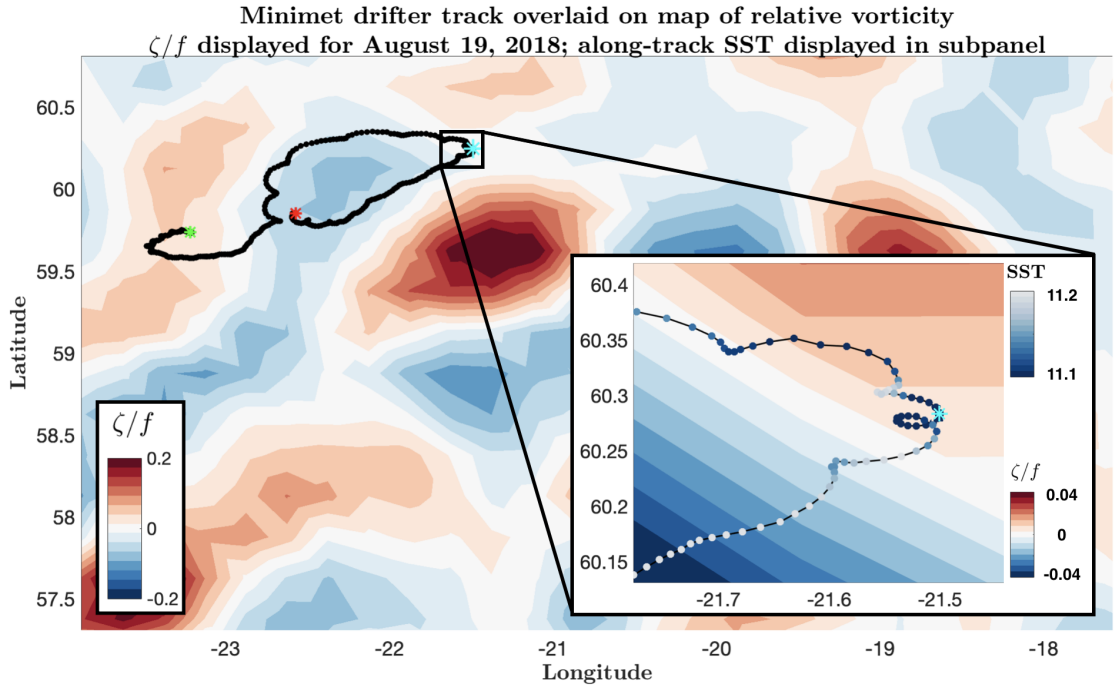

Figure 2.3: Minimet drifter track is displayed for August 7-27, 2018. The wind event under consideration occurred in the middle of this time-series, on August 17. Local vorticity is obtained via satellite altimetry [Data Unification and Altimeter Combination System (DUACS); Taburet et al., 2019] using the assumption of geostrophic flow and shown with the color contours. Along-track sea surface temperature (SST) is obtained from the Minimet and shown by the color of along-track data points. The drifter location on August 19, 2018 is shown with the cyan star. The green and red stars represent the drifter location on August 7 and 27, respectively.

Millard [1970], and the PWP model [Price et al., 1986]. We start by comparing these models with drifter observations of wind stress and surface currents in the Icelandic Basin. We then estimate the global impact of TLs on power input to near-inertial motions in the OSBL and TKE production.

2.3.1 Local analysis: Iceland Basin (NISKINe site)

The Office of Naval Research (ONR)-sponsored Near Inertial Shear and KInetic eNergy experiment in the North Atlantic (NISKINe) is an ongoing Departmental Research Initiative (DRI) to investigate the generation, evolution, and dissipation of NIWs in the Iceland Basin. This region was chosen for the strong mesoscale eddy field and stormy weather.

As part of a NISKINe field campaign in the boreal summer of 2018, Klenz et al. [2022] discuss the deployment of a fleet of *in situ* Minimet surface drifters to observe the upper-ocean dynamics (i.e., surface to 15-m depth) in the Iceland Basin. The Minimet drifter [Centurioni, 2018] is a robust platform for measuring surface meteorological data, and the Lagrangian nature of the measurements make it an excellent candidate for observing the power input to near-inertial motions, as discussed previously. Specific details pertaining to these observations can be found in Goni et al. [2017], Centurioni [2018], Klenz et al. [2022].

On the 17th and 18th of August, 2018 in the Iceland Basin, a strong, impulse-like wind event occurred over a region of substantial mesoscale activity following deployment of the Minimet drifter fleet. Klenz et al. [2022] performed direct calculations of the power input to near-inertial motions associated with the wind event using the observations from the Minimets. We focus our local analysis on a 15 day period surrounding this wind event, from 10-25 August 2018.

Prior to the wind event, the step-like assumption of the slab model was violated since the MLD and TLD were 10 and 40 meters, respectively (G. Voet, *Pers. Comm.*), giving TLT/MLD = 3. We use these MLD and TLD values to parameterize a forcing stress profile for the generalized slab model. Closed form expressions for the MLTL and traditional stress profiles are provided in section 2.6.3 of the Appendix.

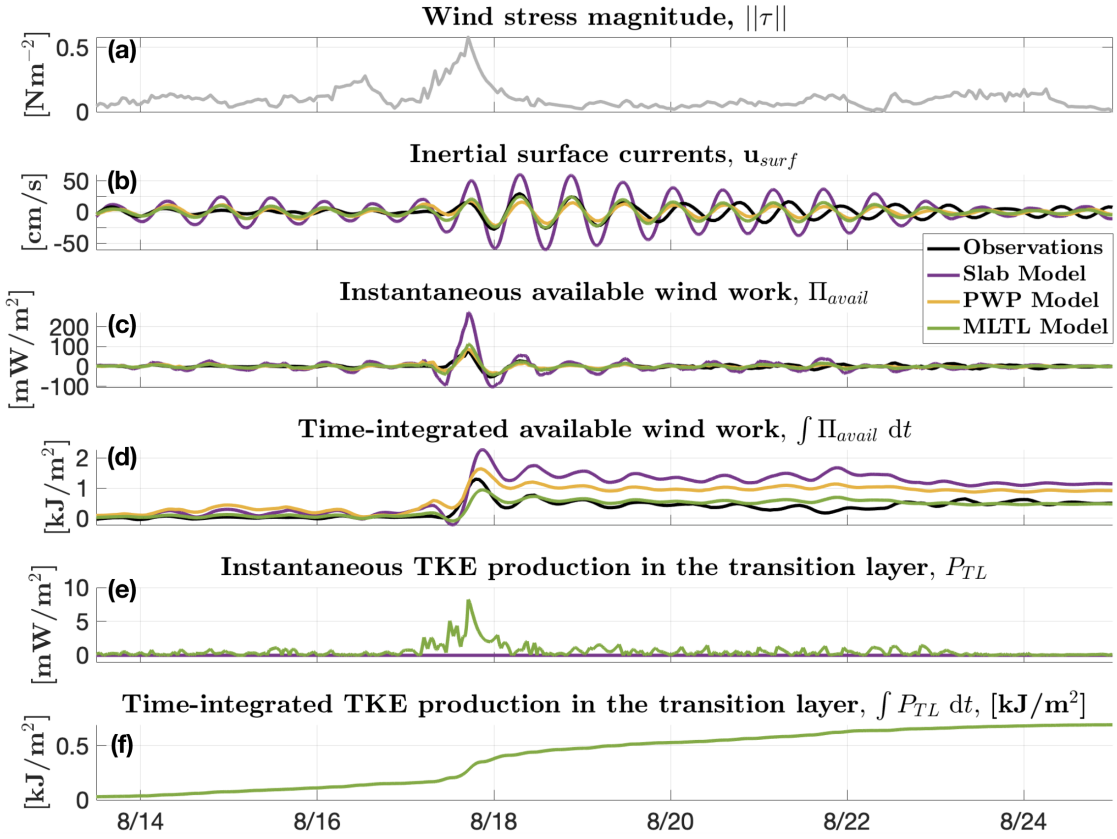

Figure 2.4: The generalized slab model is employed to study the near-inertial response to an impulse-like wind event on 17-18 August, 2018 at the NISKINe site in the Iceland Basin. Lagrangian Minimet surface drifters described by Klenz et al. [2022] provide *in situ* measurements of $\boldsymbol{\tau}$, $\mathbf{u}_{surf}$ and Π_{avail}. The observations of $\boldsymbol{\tau}$ from Minimet 3 [Klenz et al., 2022] are shown in the top panel, and are used as the forcing input for the generalized slab model and PWP. Generalized slab model calculations are performed using both the slab and MLTL stress profiles. For consistency with Klenz et al. [2022, Figure 7], MLD and TLD are set to 10 m and 40 m, respectively. Zonal inertial surface velocities are shown in panel (b). Panels (c) and (d) show the instantaneous and time-integrated Π_{avail}, respectively. Panels (e) and (f) show the instantaneous and time-integrated P_{TL}, respectively. In all cases, the purple line represents the slab model, the gold line represents PWP, the green line represents the MLTL model, and black line represents observations from Klenz et al. [2022].

Hourly surface wind stress measurements by Minimet 3 [see Klenz et al., 2022, Figure 4 for drifter coordinates] are used to force the traditional slab model (with a linear stress profile), generalized slab model (with a MLTL stress profile), and PWP (Fig. 2.4). Prior to the model runs, we apply a 24 hour 1/2 cosine Fourier filter to the wind stress time series to suppress the generation of low frequency mean flows and isolate the near-inertial response. We follow the procedures in Section 2.2 to calculate transports, inertial currents, wind work (total and available), TKE production, and the TKE fraction. Climatological stratification and ocean depths are obtained from the World Ocean Atlas (WOA) 2023 [Locarnini et al., 2023, Reagan et al., 2023] and version 24.1 of Smith and Sandwell [1997], respectively. Summations are truncated at 256 vertical modes. We use a constant Rayleigh damping coefficient of $r^{-1} = 7$ days in the analysis of each model, for consistency with Plueddemann and Farrar [2006]. The Coriolis frequency f varies with drifter location in our model calculations, but the local vorticity is not considered. We configure and run PWP by following Plueddemann and Farrar [2006] and Alford [2020a].

The observed inertial velocities and those predicted by the MLTL model show excellent agreement in both magnitude and phase immediately following the wind event. PWP slightly under-predicts the observed inertial velocities, while the slab model overpredicts the inertial currents, which is expected for shallow MLDs [D'Asaro et al., 1995, Plueddemann and Farrar, 2006]. After a few inertial oscillations, a phase lag develops between the observations and model outputs and the oscillations detune. However, despite differences in phase, the inertial velocity magnitudes associated with the MLTL model output and observations remain consistent (Fig. 2.4).

The Iceland Basin is a region characterized by a highly energetic eddy field [Zhao et al., 2018, Thomas et al., 2020], so the phase lag may be caused by variability in local vorticity. The sharp nature of the detuning suggests the change is related to frontal behavior. In Figure 2.3, we zoom in on the drifter track/location on August 19, 2018 (time of the phase change). Local vorticity is shown in the colored contours of the figure, obtained via satellite altimetry from the Data Unification

and Altimeter Combination System (DUACS) and distributed by the "Copernicus Marine Environment Monitoring Service" (CMEMS); [Taburet et al., 2019]. Because this method of vorticity calculation uses the assumption of geostrophic flow, it cannot resolve sub-mesoscale vorticity and is thus limited to the mesoscale. However, the drifter track suggests that the Minimet encounters a sub-mesoscale eddy ($\sim$ 60.27 N, 21.52 W) at the time when the phase offset appears in the inertial velocities. The drifter, initially traveling eastward, passes through a polarity change in relative vorticity that is coupled with a sea-surface-temperature (SST) gradient and shifts to westward propagation following its encounter with the sub-mesoscale eddy (note that SST data is obtained from the Minimet). The collection of these effects supports our hypothesis that the dephasing of the model and observations is related to a frontal change in local vorticity. Since the observations do not fully resolve sub-mesoscale vorticity, we do not attempt to include these effects in the generalized slab model.

The maximum values of instantaneous wind work calculated by the generalized slab model with the MLTL stress profile and PWP are consistent with the observations, while the slab model again overestimates the peak magnitude of Π_{avail} (Fig. 2.4c). For each model, time-integrated wind work shows a variable degree of deviation from the observations (Fig. 2.4d). Values calculated using the MLTL stress profile show closest agreement with observations. Integrated wind work calculated via PWP and the traditional slab model exceeds observations in both cases. The increased available wind work in PWP is due to a bookkeeping difference. Note that PWP extracts TKE shear production through the damping stress, so all wind work is technically available to drive the inertial currents. In practice, the turbulence parameterization in PWP immediately dissipates a significant fraction of this available wind work.

The wind event acts as an isolated, impulsive forcing event with minimal instantaneous wind work preceding or following 17-18 August (Fig. 2.4). In all cases (i.e., slab, PWP, MLTL, and observations), the peak instantaneous wind work and the peak wind stress magnitude occur on 17 August at 1600, suggesting that hourly resolution is too coarse to estimate the lag between the wind event and

energy input to inertial motions.

There is a substantial burst of TKE production associated with interactions between shear stress and velocity shear in the TL surrounding the wind event that mirrors the burst in Π_{avail}. Otherwise, P_{TL} is generally small and nonzero. Although the TKE production is small compared to the wind work, the TKE production is always positive. After the two-week example time series studied here, the final magnitude of time-integrated P_{TL} is comparable to the final magnitude of time-integrated Π_{avail}. Cumulatively over the course of this example two-week time series, the total wind work is reduced by a factor of ~ 2 as a result of TKE production in the TL.

The TKE dissipation rate (ϵ) can be measured directly using rapidly sampling microstructure shear probes [Gregg, 1991, Thorpe, 2005] and is thus more readily observable than TKE shear production (P). A precise transformation that allows ϵ to be determined from P and vice versa is a topic of ongoing research and beyond the scope of this paper [e.g., Zippel et al., 2022]. However, we follow Alford [2020a] by using dimensional analysis and scaling to estimate the order-of-magnitude of ϵ from P_{TL} that is calculated by the generalized slab model.

Ignoring advective and straining terms, TKE shear production is related to the dissipation rate (ϵ) and the buoyancy flux (J_b) via $P = \epsilon + J_b$ [Tennekes and Lumley, 1972]. Studying turbulent dissipation in the TL, Kaminski et al. [2021] show that a mixing efficiency Γ of 0.2 (defined $\Gamma \equiv J_b/\epsilon$) can be used to relate buoyancy flux to dissipation. Finally, we note that the TKE production in our model has units of power input per unit area while ϵ has units of power input per unit mass. We may convert between the two using the density of seawater and the relevant length scale, which is in this case the TLT. Using values from the August 2018 wind event at the NISKINe site, we find $\epsilon_{TL} \sim \mathrm{O}(10^{-8})$, which is consistent with previous observations of ϵ in the TL which find $\epsilon_{TL} \sim \mathrm{O}(10^{-9} - 10^{-8})$ W/kg [Sun et al., 2013, Kaminski et al., 2021].

We calculate modal spectra for the slab and MLTL models and find that wind work in high modes attenuates much faster with increasing mode number for the MLTL model than for the slab model. Spectra are displayed in Figure 2.5. Mode

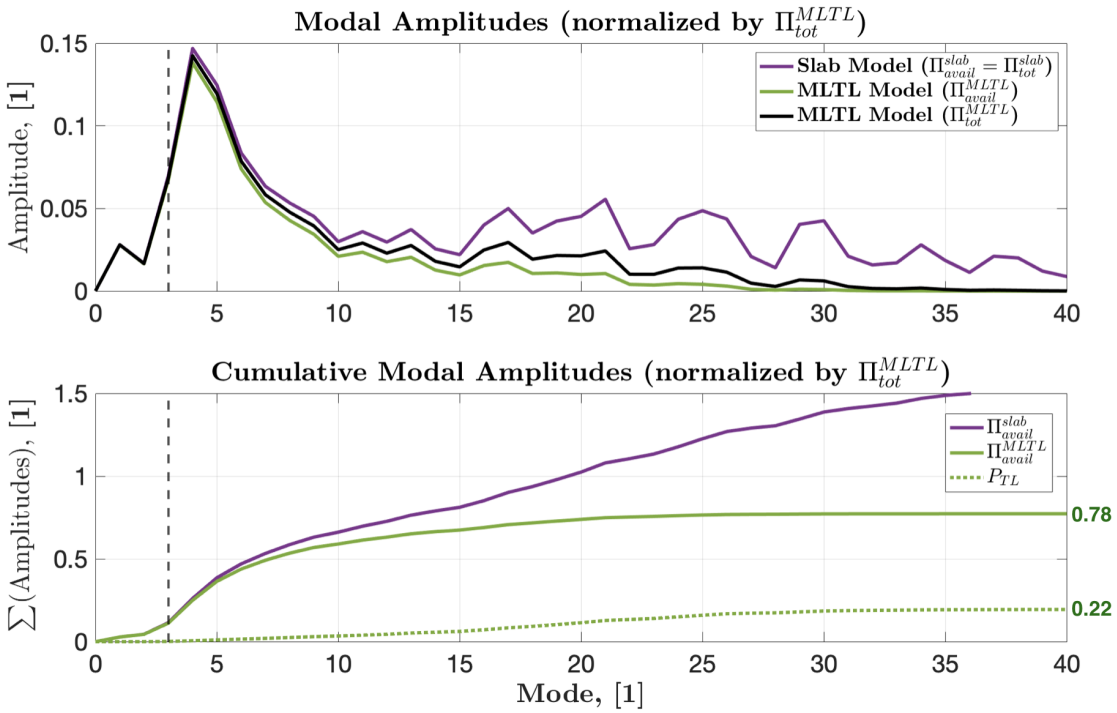

Figure 2.5: Modal spectra for the slab and MLTL model are calculated for the NISKINe site (August 2018; 60 N, 22 W). The OSBL at the NISIKINe site has MLD of 10 m and TLD of 40 m. **Top panel:** Spectral amplitude vs. mode number is displayed. Amplitudes for the total wind work as calculated via slab model (Π_{tot}^{slab}), total wind work as calculated via MLTL model (Π_{tot}^{MLTL}), and available wind work as calculated via MLTL model (Π_{avail}^{MLTL}) are shown with the purple, black, and green lines, respectively. Note that total and available wind work are equal in the case of the slab model. All curves are normalized by the total amplitude of Π_{total}^{MLTL}, for example, $\sum_{n=1}^{\infty} \phi_{ns}\phi_n(0)$. **Bottom panel:** The cumulative modal amplitudes are displayed vs. mode number for the total wind work calculated with the slab model (purple line), available wind work calculated with the MLTL model (green solid line), and TKE production in the TL calculated with the MLTL model (green dotted line). All curves are again normalized by the total amplitude of Π_{avail}^{MLTL}. Normalization by Π_{avail}^{MLTL} allows for easy viewing of the division of total wind work into IKE and TKE, shown by the asymptotic values (horizontal color-matched dash-dotted lines): in this example the sum of amplitudes for P_{TL} and Π_{avail}^{MLTL} are asymptotic to 0.22 with $\sim$ 30 modes and 0.78 with $\sim$ 20 modes, respectively (indicated on the right-hand y-axis). The sum of amplitudes for Π_{tot}^{slab} is asymptotic to 3.12 with $\sim$ 180 modes, indicating that in the case of NISKINe, the slab model overestimates wind work by a factor of 3. Mode 3 is indicated in both panels to mark the classical division between radiative and dissipative modes [Alford, 2020b].

3 is indicated in the figure to mark the classical division between radiative and dissipative modes [Alford, 2020b]. Following Figure 2.4, we assert that available wind work calculated using the MLTL model provides wind work estimates more aligned with observations than the slab model. When viewed in tandem with Figure 2.5, this suggests that the slab model overestimates the wind work in high modes, consistent with the findings of Plueddemann and Farrar [2006], Alford [2020a]. In the NISKINe test case specifically, we see that overestimation of Π becomes significant around mode 10.

A secondary effect that results from the slab model's overestimation of higher-mode wind work is that fewer modes are required to resolve Π when a TL is considered. For the NISKINe test case, total wind work via the MLTL model requires ~ 40 modes to resolve, while total wind work via the slab model requires ~ 150 modes to resolve (Figure 2.5). This is easy to visualize from a mathematical analogy: in a modal decomposition of the slab model, we are reconstructing a step-like profile using smooth, continuous functions. This is analogous to reconstructing a square wave using a Fourier series, which will require infinite modes to reach closure. The TL serves to smooth the step-like discontinuity at the base of the ML, and allows us to resolve the dynamics with fewer modes.

Normalization of available wind work and TKE production by the total wind work highlights how the total power input by the atmosphere is partitioned. A larger fraction of total wind work goes to TKE production for higher modes (Fig. 2.5). Enhanced TKE production begins around mode 10, consistent with the slab model overestimation of Π. In our test case, available wind work is resolved with 25 modes and is 78% of the total wind work and TKE production is resolved with 40 modes and is 22% of the total wind work. Overall, total wind work calculated via the slab model exceeds total wind work via the MLTL model by a factor of 3.

In both models, the spectral peak lies in the dissipative regime at mode 4, with only 8% and 14% of energy contained in modes 1-3 for the slab and MLTL models, respectively. These dissipative spectra are reasonably expected considering the extremely shallow MLD of 10 m. However, the MLTL spectrum sees a red-shift relative to the slab spectra. For deep MLs, the projection onto low modes is

stronger than for shallow MLs [Alford, 2020b]. It follows that the stress profile's impact on the modal projection is inversely proportional to the MLD [D'Asaro et al., 1995]. Our test case at the NISKINe site, with such a shallow ML, provides a limiting case in this sense. Even for the 10 m MLD here, there is less than a 2% difference between the modal amplitudes for the slab and MLTL stress profiles in the radiative modes (1-3). We conclude that a traditional slab model will perform well if only the low-mode dynamics are to be addressed, but one must proceed cautiously for higher modes. Beyond mode 3 deviations between the slab and MLTL models grow rapidly (Fig. 2.5), and the total number of modes used in analysis must be taken into careful consideration.

The cumulative modal amplitudes (Fig. 2.5, bottom panel) reveal how the MLTL stress profile results in a two-fold reduction in the power input to inertial motions with comparison to the slab stress profile. First, because momentum is deposited beneath the ML, inertial currents are reduced, thereby reducing Π_{tot}. This reduction of inertial currents is very pronounced in the Minimet dataset (Fig. 2.4, panel b), with a corresponding $\sim 60\%$ reduction in Π_{tot} (Fig. 2.5, bottom panel). Second, the power imparted to inertial motions is given by Π_{avail}, rather than Π_{tot}. The available wind work incurs an additional $\sim 22\%$ reduction as a result of TKE production in the TL (Fig. 2.5, bottom panel). For the NISKINe case study, the net effect is a $\sim 70\%$ reduction in the power input to inertial motions.

2.3.2 Global Analysis: geospatial characteristics of the TL and implications to TKE production

Data collected from Argo autonomous profiling floats throughout the lifespan of the program [1997-2023; Wong et al., 2020] are used to calculate the TL characteristics on a global scale. We restrict our analysis to high-resolution data (≤ 2 m vertical) because the base of the TL is difficult to resolve if the vertical resolution is too coarse [Johnston and Rudnick, 2009, Helber et al., 2012, Sun et al., 2013]. The local minimum method of Sun et al. [2013] is used to determine TLDs. The procedure picks the base of the TL as the depth corresponding to the first local

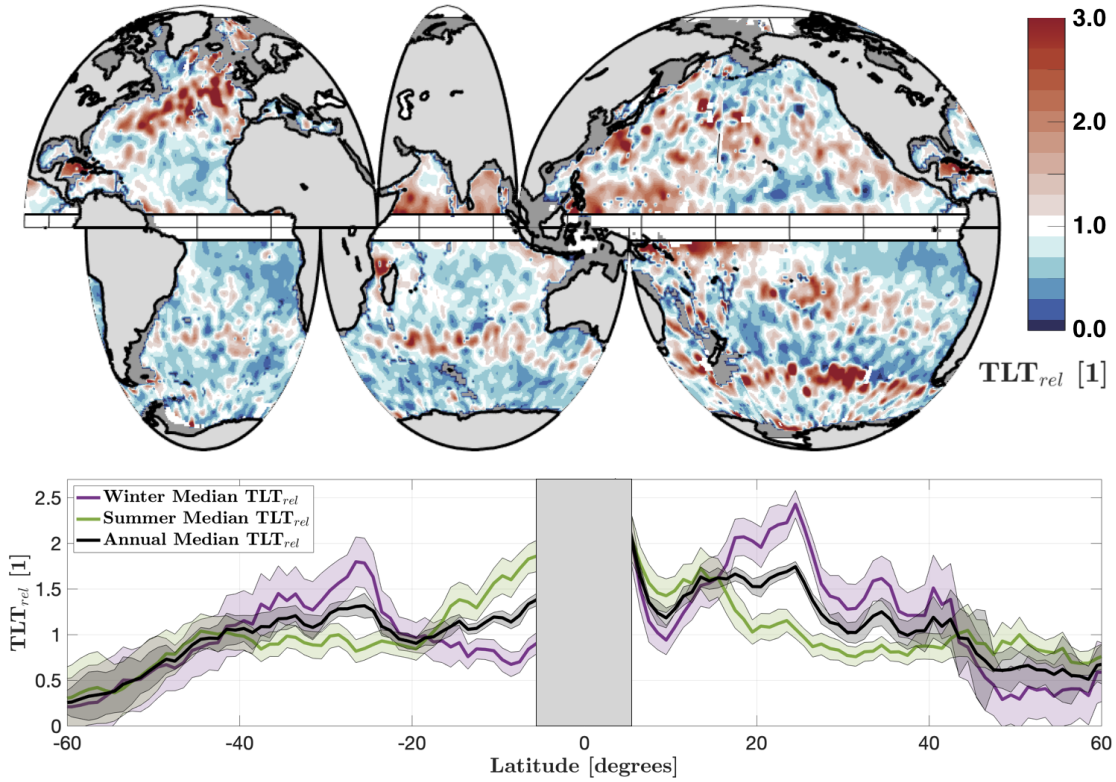

Figure 2.6: Relative transition layer thickness (TLT_{rel}, determined as TLT_{rel} = TLT/MLD) is calculated using high-resolution Argo data and displayed for the global ocean. The pivot point of the diverging colormap is set at $TLT_{rel} = 1$ so that grid points shaded red have TLT<MLD and grid points shaded blue have TLT>MLD. In the line plot below, annual and seasonal median values are given as a function of latitude. Error bars represent standard error, as the distribution of TLT_{rel} is non-Gaussian. Depths less than 2000 m are omitted.

minimum in stratification beneath the depth of maximum stratification. Sun et al. [2013] show this method to be reliable, but occasionally this method may fail if a local minimum does not appear until well below the seasonal thermocline. These cases can introduce anomalously large TLDs. For cases where the local minimum method fails, the depth of maximum stratification is used to characterize the TLD in an effort to keep estimates of TLD conservative. MLDs are taken from the climatologies developed by [Holte et al., 2017]. Together, observations of TLD and MLD allow for the calculation of TLT and the MLTL stress profiles at all grid points with high-resolution Argo data. We ignore the region within $\pm$ 5^o of the equator as slab-like models fail as $f \to 0$ in the equatorial zone.

To assess the validity of a traditional slab model, we compute the relative TL thickness [TLT_{rel} = TLT/MLD]. We assert that if $\text{TLT}_{rel} \sim O(1)$, the assumption of a negligible TL is violated. A global map of annual-mean TLT_{rel} is shown in Figure 2.6. The TLT_{rel} mirrors many trends of MLD [see Holte et al., 2017], most notably that deep TLD and MLD appear in the mode water regions associated with the Southern Ocean, South Atlantic, Gulf Stream, and Kuroshio [Hanawa and Talley, 2001]. These patterns are consistent with the low-resolution estimates of absolute TLT thickness from Helber et al. [2012]. In the bottom panel of Figure 2.6, annual and seasonal median TLT_{rel} values are plotted for each latitude. We elect to use the median rather than the mean because the distribution of TLT_{rel} is not Gaussian. Deviations from a normal distribution increase in regions where the ML is quite shallow. This creates outliers where TLT_{rel} is extremely large, skewing the distribution of TLT_{rel}.

Furuichi et al. [2008], Simmons and Alford [2012], Alford [2020b], and others have shown that there is strong seasonality to wind work that is tied to seasonal variability of the ML. This motivates us to assess seasonal variability of the TL. We follow Alford [2020b] in performing calculations for a global winter and summer. For a global winter we concatenate results from months 1-3 (Jan-Mar) in the northern hemisphere with months 7-9 (Jul-Sep) in the southern hemisphere. The opposite is done for a global summer. The idea behind the global seasonal extremes is to investigate bounding behavior of the TL. The magnitude of TLT_{rel} is greater

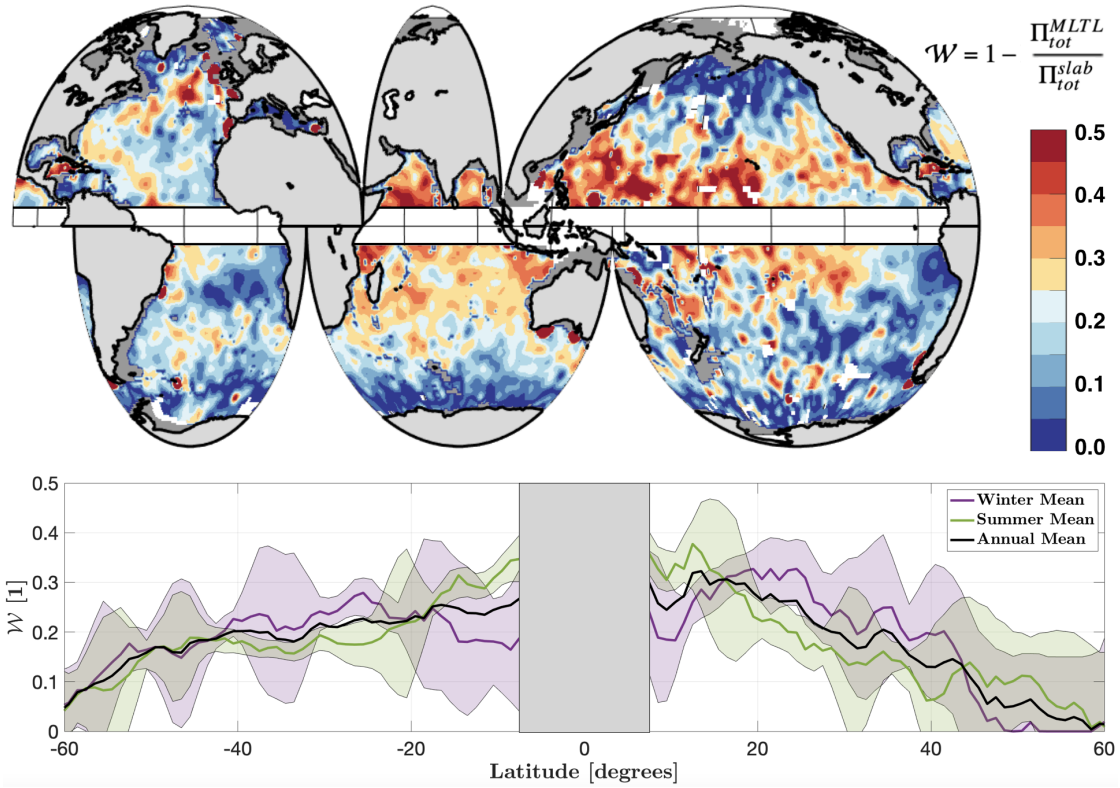

Figure 2.7: The annual-mean ratio $\mathcal{W} = 1 - \Pi_{tot}^{MLTL}/\Pi_{tot}^{slab}$ is calculated from Argo data and shown globally to assess the impact the TL on wind work calculations. Latitude-mean values of $\mathcal{W}$ are shown in the line plot below the map, with error bars representing the standard error for each latitude bin. Depths less than 2000 m are omitted.

in the mid-latitude regions during the winter time, consistent with expectations of Helber et al. [2012].

We first use the global distribution of TLT_{rel} (Fig. 2.6) to investigate the primary reduction in Π_{tot} associated with the decrease in inertial current generation when momentum is deposited in the TL. In Figure 2.7, we sum over 256 verical modes to display the global distribution of annual-mean $\mathcal{W} = 1 - \Pi_{tot}^{MLTL}/\Pi_{tot}^{slab}$ and a seasonal latitude-mean line plot. The reduction of Π_{tot} is correlated to the geospatial distribution of TLT_{rel}, with larger TLT_{rel} producing greater disparities between Π_{tot}^{slab} and Π_{tot}^{MLTL}. These disparities are magnified in some regions of the ocean, notably the Gulf Stream, North Indian Ocean, and Southern Ocean. We find that on the annual-mean, using the MLTL stress profile rather than the

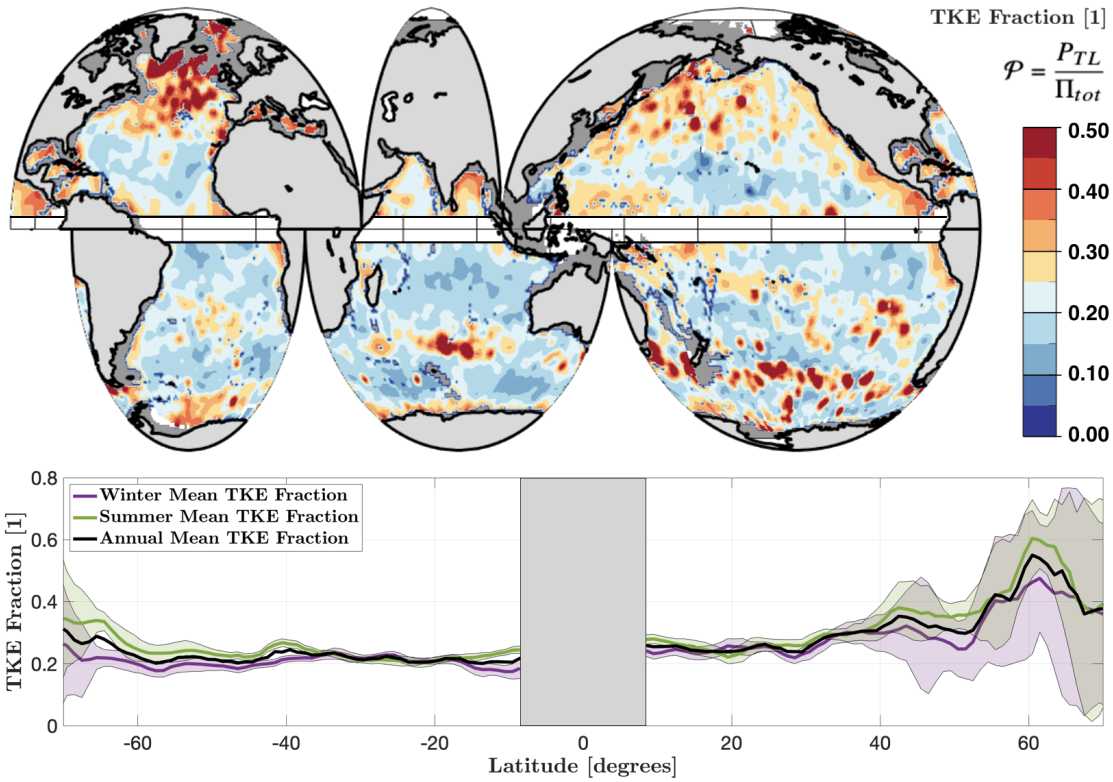

Figure 2.8: The TKE fraction calculated using the MLTL stress profile is shown for the annual-mean. A value near 0 indicates that the there is little to no TKE production, consistent with the traditional slab model of Pollard and Millard [1970]. A value near 1 indicates that nearly all of the wind work is diverted to turbulence production rather than exciting near-inertial motions. Latitude-mean values of $\mathcal{P}$ are shown in the line plot below the map, with error bars representing the standard error for each latitude bin. Depths less than 2000 m are omitted.

traditional slab stress profile reduces total wind work by $\sim 15-25\%$, with local reductions upwards of 50% in extreme cases.

The TKE fraction quantifies the secondary reduction in power input to inertial motions associated with the MLTL stress profile and is calculated via (2.2.2.14). The annual-mean $\mathcal{P}$ is shown in the map displayed in Figure 2.8. The patterns in the TKE fraction map are similar to those in the TLT_{rel} map (Figure 2.6), where the TKE fraction is elevated in areas where TLT_{rel} is large. As in Figures 2.6 and 2.7, the Gulf Stream, North Indian Ocean, and Southern Ocean stand out with elevated $\mathcal{P}$. Latitude-mean dissipation is calculated and displayed in the line plot of Figure 2.8, with error bars representing the standard error of the mean. The

latitude-mean plot of $\mathcal{P}$ in the bottom panel of Figure 2.8 displays trends that do not identically mirror the trends in the latitude-mean TLT_{rel}, contrary to expectation. Most notably, summertime TKE fraction exceeds that of the winter months throughout the ocean. On the global, annual-mean, $\sim 30\%$ of the total wind work is converted to TKE in the TL. In the high-latitude northern hemisphere, this percentage increases to $\sim$ 50-70%.

2.4 Discussion

The curvature of the forcing stress profile has three important implications for the atmospheric power input to the internal wave band. First, the shape of the stress profile can spread momentum input over a greater depth range, reducing surface currents and total wind work (Π_{tot}). Second, when the stress profile extends beneath the base of the mixed layer (ML), a fraction of the total wind work is converted into turbulent kinetic energy (TKE) production via the TKE fraction (P_{TL}). Third, the shape of the stress profile sets the vertical wavenumber spectra, which influences the radiation of internal waves. The sum of these three effects manifests in a generalized slab model that offers improved agreement with observations over the traditional slab model (e.g., Figure 2.4), and underscores the need to refine and improve models and measurements of $\boldsymbol{\tau}(z)$ and $\epsilon(z)$ in the oceanic surface boundary layer (OSBL).

2.4.1 Calculation of total wind work

For the traditional slab model, wind work calculations often exceed observations due to the concentration of momentum in the ML. This issue has been recognized since the model's introduction [Pollard and Millard, 1970], and is exacerbated in locations with a shallow ML, as shown by D'asaro [1995] and Alford [2020a]. Including a TL allows near-inertial momentum imparted by the atmosphere to extend beneath the ML which decreases the calculated inertial currents. In cases of a shallow ML such as observed during NISKINe, this effect considerably improves agreement with observations. In the second panel of Figure 2.4, the improved

agreement for the case of a TL is self-evident, with inertial currents calculated using the stress profile of a traditional slab model exceeding observations by a factor of ~ 2. We use Argo float data to estimate the magnitude of this effect on a global scale (i.e., Fig. 2.7) and find that wind work estimates calculated with the traditional slab model are biased high by a factor of 1.22 on the annual-mean, globally. This is remarkably consistent with the overestimation bias of 1.23 reported by Alford [2020b].

2.4.2 TKE fraction

The TL is a region of strong shear, where the near-constant velocity profile of the ML adapts to the much smaller velocities characteristic of the stratified interior [Sun et al., 2013]. When the forcing stress profile penetrates the TL, a nonzero fraction of the total wind work is converted into TKE production. This term is always zero in models that omit forcing in the TL and assume a linear stress profile in the ML. Using Argo float data to specify MLTL forcing stress profiles, we estimate the TKE fraction to be ~ 0.3 on the annual-mean, globally. In the high-latitude northern hemisphere, the TKE fraction increases to $\sim$ 0.5-0.7. When taken in tandem with the latest global, annual-mean estimates for near-inertial power input of 0.27 TW [Alford, 2020a], these results suggest that 0.08 ± 0.01 TW of the total near-inertial power input are diverted to TKE production rather than generating near-inertial motions. This estimate could be greatly improved by collecting more observations of OSBL turbulence. For example, by equipping Argo floats with microstructure instruments [Roemmich et al., 2019].

The TKE fraction represents the *relative fraction* of the total wind work that is converted to TKE production when the TL is considered in the calculation. Despite the greater *relative* impact of the TL in the summer (Fig. 2.8), *total* wind work is much larger in the winter. Furuichi et al. [2008], Simmons and Alford [2012] find that wintertime wind work is 2-4 times greater in magnitude than in summertime. Thus, the total TKE production in the TL is substantially larger in the winter than in the summer, despite a smaller TKE fraction. For a simple numerical example, [Furuichi et al., 2008, Simmons and Alford, 2012] estimate

that wind work contributes an annual-mean of $\sim$ 400 GW to the global ocean. Ignoring the spring and fall, for a naive argument, we take the middle ground and set winter wind work to 3 times that of summer, so that wind work in the summer contributes $\sim$ 200 GW while wind work in the winter contributes $\sim$ 600 GW. With these numbers and the seasonal TKE fractions calculated from Argo float data, it follows that $\sim$ 40 and $\sim$ 120 GW of the total wind work are converted to TKE production in the TL for the summer and winter, respectively.

2.4.3 Available wind work

Available wind work is the total wind work minus the energy lost to TKE shear production. Alford [2020a] estimated that global available wind work is only 39% of total wind work for PWP, while we estimate a value closer to $\sim$ 70%. The difference arises because Alford [2020a] computed power lost to turbulence by examining the change in potential energy due to ML deepening. ML deepening is driven by intense, short-lived, storms that dramatically alter the ML and TL. In contrast, the TKE shear production estimated here is based on ML and TL climatologies, such that our MLTL stress profile represents an "average" response to moderate winds. As stated earlier, our MLTL stress profile is not appropriate for during storms that dramatically alter the ML and TL. For such storms, ML and TL statistics should be verified against observations to provide accurate wind-work predictions (e.g., Iceland Basin test case). However, in the high-latitude northern hemisphere where the TKE fraction is large, we find that the available wind work is reduced to $\sim$ 30-50% of the total wind work, consistent with Alford [2020a].

A second difference in our estimation of available wind work is the interpretation of dissipation due to the Rayleigh damping term. Our $\sim$ 30% dissipation estimate of results from P_{TL} which arises from the forcing stress profiles alone with no consideration of how oscillations are damped after being set in motion. Additional analyses are necessary to better understand how the energy loss parameterized by Rayleigh drag is divided between internal wave radiation and additional TKE production. Estimates from Alford [2020b] are calculated using PWP estimates of changes in potential energy, which are driven by both "instantanous" wind mix-

ing and mixing induced after the wind forcing has stopped and the currents are spinning down.

2.4.4 Vertical wavenumber spectra

The analysis presented suggests that the slab model and MLTL produce comparable results for the low, radiative modes, but diverge considerably for the dissipative modes (4-∞). These spectra show that for the analysis of the dissipative modes, the shape of the stress profile must be considered. It follows that if one is to compare wind work from different models, care must be taken regarding the number of modes considered. To that effect, we show that the traditional slab stress profile requires far more modes for convergence. With regard to computational expense, the improved convergence of the MLTL model further incentives implementation of a nonlinear stress profile.

2.4.5 Relation to PWP

PWP and the generalized slab model both accurately predict inertial currents, which are necessary to calculate wind work (Fig. 2.4, panel b). A major strength of PWP is that, by accurately parameterizing turbulence dynamics, it can predict the vertical structure of currents using MLD and TLD from background stratification and wind stress alone. In contrast, the generalized slab model leverages observations to eliminate turbulence parameterizations (outside of the Rayleigh drag). In essence, the generalized slab model infers TKE shear production in the TL from observations of stress or currents or MLD and TLD.

The excellent agreement between PWP and the generalized slab model currents in the Icelandic Basin implies that the turbulence parameterization in PWP is consistent with the observed MLD and TLD at that location. We reiterate that differences in available wind work (Fig. 2.4, panel c) are primarily due to different bookkeeping conventions. PWP accounts for TKE shear production in the TL through a damping stress, while the generalized slab model accounts for TKE shear production through a forcing stress. Specifically, PWP estimates about 0.5

kJ/m^2 of "excess" available wind work, which nearly matches the MLTL estimate of 0.6 kJ/m^2 of P_{TL}. These bookkeeping differences might be eliminated by applying wind stress in PWP using an MLTL stress profile rather than a linear (slab) profile. Such a modification would likely reduce regions of subcritical Richardson number, essentially "turning down" the PWP turbulence parameterization. However, we are uncertain how this modification would affect the accuracy of PWP current predictions, particularly during high winds.

We can use the PWP model as a control to estimate the viability of the generalized slab model's inferred TKE production. Alford [2020b] calculated the traditional slab model's overestimation bias factor of 1.23 by comparing the traditional slab results to PWP. We have calculated a comparable overestimation bias factor of 1.22 via comparison with the MLTL model. The two methods used here are completely different numerically, but produce nearly identical results. This implies that the MLTL and the PWP models both vertically spread momentum in the same way, despite the different approaches to the problem, and reinforces the importance of TKE production in the TL.

2.5 Conclusion

The generalized slab model developed here allows for the calculation of the ocean's linear response to an arbitrary, nonlinear, depth-variable forcing stress profile. To introduce a first-order improvement upon the step-like, linear stress profile of the traditional slab model, we utilized a piecewise-nonlinear MLTL stress profile inspired by D'Asaro et al. [1995] which injects momentum into the TL. Our analyses show that nonlinearities in the stress profile lead to a two-fold reduction in power input to inertial motions. When the TL is considered, momentum is distributed to greater depths, reducing surface currents and inducing a primary reduction in wind work. A secondary reduction in wind work results from TKE production in the TL which reduces the amount of energy available to generate inertial currents in the OSBL. Direct comparison between Minimet observations in the Iceland Basin [Klenz et al., 2022], the traditional slab model, the generalized

slab model with the MLTL stress profile, and the PWP model suggest that including the TL improves the slab model performance. Modeled TKE production in the TL in Icelandic Basin is consistent with other observations of turbulent dissipation in the TL [Sun et al., 2013]. A global analysis of Argo autonomous profiling float data suggests that on the global, annual-mean, $\sim 30\%$ of the total power input to near-inertial motions is allocated to TKE production. When taken in tandem with the latest global, annual-mean estimates for near-inertial power input of 0.27 TW [Alford, 2020a], these results suggest that 0.08 ± 0.01 TW of the total near-inertial power input are diverted to TKE production rather than generating near-inertial motions. We emphasize that our estimates of TKE production represent conditions of moderate winds and stress profiles based on climatology.

2.6 Declarations

2.6.1 Acknowledgements

I. A. Stokes was supported by ONR Grant N00014-22-1-2730. A. J. Lucas was supported by ONR Grants N00014-22-1-2730, N00014-22-1-2575, and N00014-21-C-1027. S. M. Kelly was supported by ONR Grant N00014-181-2800 and NSF Grant OCE-1635560. T. Klenz was supported by NSF Grant 1658302 and ONR Grant N000141812386. C. B. Whalen was supported by ONR grant N00014-18-1-2598. A. F. Waterhouse was supported by ONR grants N00014-18-1-2423 and N00014-22-1-2575. L. Centurioni and V. Hormann were supported by ONR Grant N000141812445. Minimet drifters used in this study were funded by ONR Grant N000141712517 and NOAA Grant NA150AR4320071 "The Global Drifter Program." We thank the captain and crew of the R/V Neil Armstrong. Drifter velocities were calculated using J. M. Lilly's MATLAB toolbox, jLab [Lilly, 2021]. The authors are grateful to Matthew Alford for his comments on a previous version of the manuscript, which led to an improved article. We thank Brewer et al. [2003] for providing the colormaps used in this work.

Chapter 2, in full, is a reprint of the material as it appears in A Generalized Slab Model, Journal of Physical Oceanography. Ian A. Stokes, Samuel M. Kelly, Andrew J. Lucas, Amy F. Waterhouse, Caitlin B. Whalen, Thilo Klenz, Verena Hormann, Luca Centurioni; *Minor Revisions* 2023. The dissertation author was the primary investigator and author of this paper.

2.6.2 Data Availability Statement

All shipboard and drifter data collected as part of the U.S. ONR NISKINe DRI are still in the process of being organized and archived. All data will be fully released to the public when the program formally concludes. NISKINe data presented in this study are available from the corresponding author upon reasonable request. Argo data were collected and made freely available by the International Argo Program and the national programs that contribute to it (http://www.argo.ucsd.edu, http://argo.jcommops.org). The Argo Program is part of the Global Ocean Ob-

serving System. Argo (2000). Argo float data and metadata are from Global Data Assembly Centre (Argo GDAC). SEANOE. http://doi.org/10.17882/42182. Satellite altimetry datasets are available from the CMEMS web portal (http://marine.copernicus.eu/services-portfolio/access-to-products/, last access: 29 July 2023) and the C3S data store (https://cds.climate.copernicus.eu, last access: 29 July 2023).

2.6.3 Appendicies

Obtaining a semi-analytical solution

Here we outline a procedure that can be used to obtain a semi-analytical solution from the theory presented.

1. Obtain the wind-stress time series, stratification, and ocean depth for the study area.

2. Solve the eigenvalue problem of (2.2.2.2) to obtain ϕ_n. This can be done using spectral methods consistent with Boyd [2001].

3. Choose the structure of the stress profile, $\Sigma(z)$. We provide expressions for the traditional slab and the MLTL model in (2.6.3.1) and (2.6.3.2), but a form of Σ could be empirically derived from observations. One may also consider writing a new analytical structure function for Σ to represent an abnormal water column (e.g., double thermocline, inversions, etc.).

4. Evaluate the integral in (2.2.2.6) to calculate ϕ_{ns}. Unless the traditional slab model (2.6.3.1) is used, this will need to be done numerically.

5. Obtain $\phi_n(0)$. This is the value of ϕ_n at the ocean surface.

6. Solve (2.2.2.4) numerically to obtain $\mathbf{U}_n$ for each mode, then sum all modes to obtain total transport $\mathbf{U}$. This can be done using a convolution method consistent with Gupta et al. [2019].

7. Solve (2.2.2.10), (2.2.2.12), (2.2.2.13), and (2.2.2.14) to calculate Π_{tot}, Π_{avail}, P_{TL}, and q respectively.

Example stress profiles

Traditional, linear 'slab' stress profile: Assume a linear ML stress gradient profile, consistent with the slab model of Pollard and Millard [1970]. The conditions in a linear formulation are that the surface stress equals the wind stress, and is constant throughout the ML. Below the ML, the stress is zero. The vertical structure function for this stress profile can be expressed as

$$\Sigma(z) = \begin{cases} 1 + z/H_{\text{mix}} & \text{for } z > -H_{\text{mix}}, \\ 0 & \text{for } -H_{\text{mix}} > z, \end{cases} \tag{2.6.3.1}$$

where MLD is denoted as H_{mix}. A sketch of this stress profile is shown with the black line in the right hand panel of Figure 2.1.

Quadratic MLTL stress profile: Assume a linear stress gradient profile in the ML, but include a quadratic taper from the bottom of the ML to the bottom of the TL to obtain the MLTL stress profile. The conditions for the MLTL stress profile are that the profile is continuously differentiable, the surface stress equals the wind stress, and both the stress and its vertical gradient go to zero at the base of the TL. Solving this system produces the structure function

$$\Sigma(z) = \begin{cases} \frac{1+2(z/\text{TLD})}{1+\frac{H_{\text{mix}}}{\text{TLD}}} & \text{for } z > -H_{\text{mix}}, \\ \frac{1+2(z/\text{TLD})+(z/\text{TLD})^2}{1-\left(\frac{H_{\text{mix}}}{\text{TLD}}\right)^2} & \text{for } -H_{\text{mix}} > z > -\text{TLD}. \end{cases} \tag{2.6.3.2}$$

A Sketch of this stress profile is shown with the blue line in the right hand panel of Figure 2.1.

Chapter 3

Near-inertial wave generation in a linear, damped mixed-layer model

3.1 Authors:

Ian A. Stokes, Samuel M. Kelly, Andrew J. Lucas

3.2 Introduction

3.2.1 Motivation

Near-inertial internal waves (NIWs) play a crucial role in wind driven mixing by providing a conduit for large-scale atmospheric forcing to radiate energy into the deep ocean [Alford et al., 2016]. For internal waves, the rate at which energy propagates vertically varies with the horizontal wavenumber squared [Gill, 1982, 1984], and thus NIWs transfer energy vertically downward at a rate set by their lateral length scales [Alford et al., 2016]. It is commonly assumed that NIWs are generated with large horizontal scales that mirror the large-scale storms from which they are generated [Pollard, 1980, Thomson and Huggett, 1981, Asselin et al., 2020, Thomas et al., 2020]. Without a mechanism of scale-reduction, these large-scale waves are inefficient at transferring energy into the ocean's interior.

The importance of lateral scale-reduction is highlighted in the recent works

of Asselin et al. [e.g. 2020], Thomas et al. [e.g. 2020], among others, where a wavenumber evolution approach is employed to describe NIW behavior with time. The wavenumber evolution technique is a vetted method for analysis of NIW propagation, but does not explicitly solve for the generation of these waves. Rather, the lateral scales and energy content of the incident NIW field is used as an input, and is often assumed. We seek to improve understanding of the scales and available energy imparted to the incident NIW field by investigating the NIW generation problem in greater detail.

NIWs are predominantly generated by wind-stress curl [Alford et al., 2016], latitudinal variation in the inertial frequency [i.e., the β-effect: D'Asaro, 1989, D'Asaro et al., 1995, Moehlis and Llewellyn Smith, 2001], and interactions of near-inertial oscillations (NIOs) with the mesoscale eddy field [i.e., the ζ-effect Weller, 1982, Young and Ben Jelloul, 1997]. Wind stress acting on the ocean surface imparts momentum into the mixed layer (ML). After the wind stops, water parcels continue to move due to their inertia while turning due to Coriolis force. They complete an orbit each inertial period, creating near-inertial oscillations (NIOs). Over scales of tens to hundreds of kilometers, the spatial variability of wind stress (primarily the wind stress curl) induces non-uniformity in these oscillations, resulting in regions of convergence and divergence. In these regions, the ML is vertically stretched and squeezed, respectively [Moehlis and Llewellyn Smith, 2001], producing undulations that can propagate freely as gravity waves with a near-inertial frequency.

The meridional variability of the Coriolis parameter can generate NIWs in a similar process to generation via wind-stress curl. Consider for example, a constant wind-stress with large meridional span. The NIOs produced by the wind-stress at different latitudes vary in frequency with the local Coriolis parameter. As time progresses, the phase offsets between the northern and southern NIOs result in convergent and divergent zones, analogous to the case of variable wind-stress. Just as for wind-stress, the ML is modulated by the divergence, resulting in propagating NIWs.

Gradients in local vorticity in a mesoscale eddy field generate near-inertial waves by a similar mechanism to the β-effect [i.e. the ζ-effect: Kunze, 1985, Young

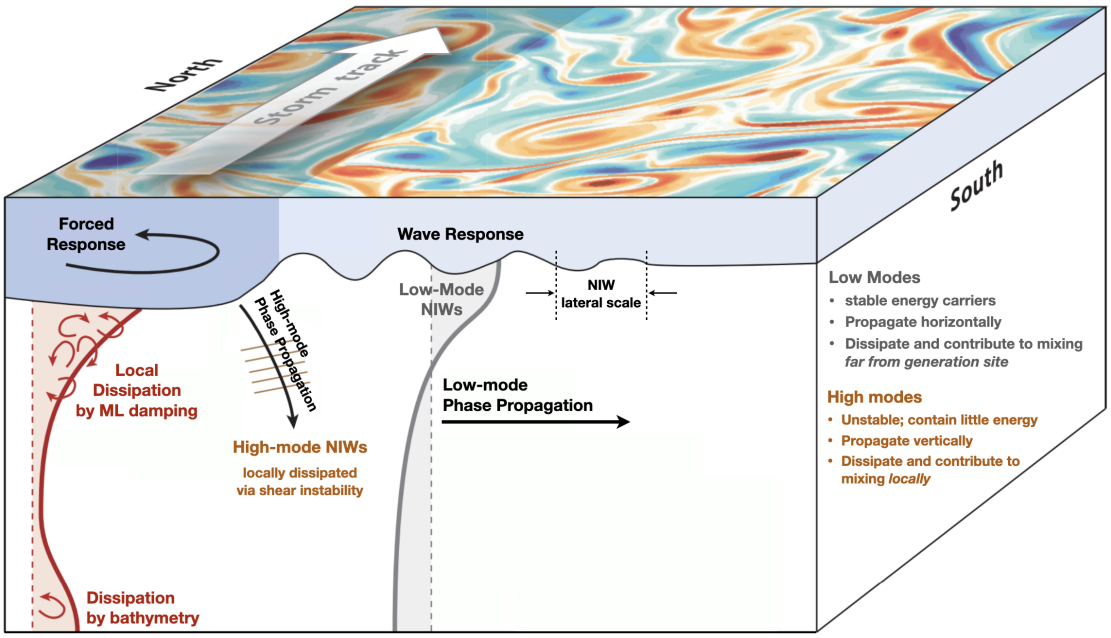

Figure 3.1: A schematic of our NIW generation model is displayed, adapted from Alford et al. [2016], Figure 7. Mid-latitude wind stress along the storm track forces inertial oscillations of the ML. The energy of these oscillations is generates local dissipation from a suite of damping processes and propagating NIWs with modal distribution set by the local stratification and stress profiles [Stokes et al., 2023]. High modes are unstable and contain little energy, but propagate vertically and contribute strongly to local mixing. Low modes are stable and carry the bulk of the near-inertial energy. The energy propagates vertically with the group velocity, which is proportional to the horizontal wavenumber. Low-mode, low horizontal wavenumber NIWs are observed to radiate far from the generation site, ultimately dissipating and contributing to mixing at remote locations [Alford, 2020b].

and Ben Jelloul, 1997]. To illustrate this process, consider a case now at constant latitude in the presence of mesoscale eddies. On a β-plane, NIOs oscillate with the effective Coriolis frequency, $f_{\text{eff}} = f_0 + \beta y + \zeta/2$, where f_0 is the central Coriolis frequency and y is latitude. For constant wind stress in the presence of an eddy field, gradients in ζ set up lateral variability in the effective Coriolis frequency. The NIOs resulting from the wind stress have ζ- imprinted phase lags that become non-negligible over scales of 10-100 km, depending on the local vorticity gradients intrinsic to the eddy field. Gradients in phase detune the initially coherent NIOs,

again producing nonzero divergence resulting in NIW generation.

These generation mechanisms can be important simultaneously in the real-world. Atmospheric storms over the open ocean often have a strong wind-stress curl that can generate NIWs [e.g. Price, 1983, Gill, 1984]). For large storms, the Coriolis parameter may vary significantly across the storm footprint [e.g. Ocean Storms experiment; D'Asaro et al., 1995]. Further complicating the issue, storms are prevalent in the mid- to high- latitudes where local vorticity due to the mesoscale eddy field is strong (e.g. Kuroshio region in the North Pacific and Gulf Stream in the North Atlantic, see Thomas et al. [2020]). The goal of the work presented here is to provide a theoretical and numerical approach to explore bounds on the lateral scales (e.g. horizontal wavenumber) and the magnitude of NIW generation from wind-stress curl, β-, and ζ- effects holistically, so that the relative importance of each can be explored for any particular case.

3.2.2 Theoretical approach:

Starting from the Boussinesq approximation for hydrostatic motions on a β-plane, we use the method of multiple scales to separate the slowly varying quasi-geostrophic flow from the internal wave field. Expansion for small Rossby number produces the internal wave equations. We follow Gill and Clarke [1974] in employing a modal decomposition and assume barotropic mean flow over a flat seafloor so that the modes remain uncoupled and are not subject to intermodal scattering. This allows us to use the formalism developed by Stokes et al. [2023] to obtain the structure of the vertical wavenumbers for each mode as a function of wind-stress forcing and stratification in the oceanic surface boundary layer (OSBL). From here, we proceed in studying the lateral near-inertial response for each mode individually, using vertical modal structure and environmental forcing (e.g. $\nabla \times \tau$, β, and ζ) as inputs.

We separate the near-inertial dynamical motions into a 'forced' component which describes accelerations of the ML due to Coriolis that arise from direct forcing by (wind) stress divergence, and a wave component in which accelerations are balanced by pressure gradients (see Figure 3.1). The forced response drives

vertical motions of the base of the ML at inertial frequencies which we refer to as 'inertial pumping.' The components of inertial pumping related to $\nabla \times \tau$, β, and ζ can be isolated and calculated explicitly for a specified wind stress, latitude, and mesoscale field using this formalism. We use frequency-wavenumber spectra to examine the how the inertial pumping overlaps the modal dispersion curves, setting bounds on the horizontal wavenumbers of NIWs that are generated.

The forced/wave decomposition allows us to parameterize dissipative stresses in the ML by including a linear damping term in the forcing equation, consistent with the ML models described by D'Asaro [1985], Plueddemann and Farrar [2006], Alford [2020a]; and Stokes et al. [2023]. The use of linear damping is common in ML models, because it allows one to account for a broad range of motions that extract energy from the system in a single variable. ML damping stresses commonly considered are turbulent entrainment at the base of the mixed layer, convective shear instabilities, and iteractions with bathymetry in the case of shallow water [Moehlis and Llewellyn Smith, 2001, Plueddemann and Farrar, 2006, Kelly, 2019, Stokes et al., 2023, see Fig. 3.1].

In the numerical experiments that follow, we find that small variations in the damping parameter can have substantial impacts on NIW generation and local dissipation. The propagation of the generated waves that are able to escape the ML is described using the 'wave-response' equations. These wave equations determine the horizontal wavenumber spectra of the NIWs, while the modal distribution and vertical wavenumber spectra are determined by the vertical profile of forcing stress [stress profile Stokes et al., 2023]. Together, this framework allows us to estimate how much energy can reach depths via low-mode, high horizontal wavenumber NIWs; how much energy can propagate to remote dissipation sites via low-mode, low horizontal wavenumber NIWs; and the high-mode contributions to mixing locally. A visual representation of these contributions is shown in Figure 3.1

By separating ML motions from internal wave generation and propagation, we find a useful, previously unappreciated analogy between the generation of internal tides in the vicinity of topography [Llewellyn Smith and Young, 2002] and the generation of NIWs by wind stress curl. We show that the equations which govern

NIW generation can be written in a form that is mathematically equivalent to the equations describing conversion of barotropic tidal energy into internal tides, providing a new perspective on NIW generation. This allows us to use tools previously developed for study of internal tide generation [e.g. the barotropic conversion formula from Llewellyn Smith and Young, 2002] to quantify the energetic volume of NIW generation for each mode.

We next present a numerical tool to solve these governing equations which is analogous to the coupled shallow water (CSW) model of Kelly et al. [2016], Kelly [2019], and Savage et al. [2020]. We refer to this tool as the extended Klein-Gordon (eKG) model. The analogy with internal tide generation allows us to validate this numerical model against analytical solutions of internal wave generation from Llewellyn Smith and Young [2002]. We then use the eKG model to study the dynamics of NIW generation across a range of environmental forcing scenarios inspired by two important oceanographic field campaigns, the Ocean Storms experiment and the Near Inertial Shear and KInetic eNergy experiment in the North Atlantic experiment (NISKINe).

3.2.3 Observations

The Ocean Storms experiment (OS95 hereafter) was an Office of Naval Research (ONR) sponsored initiative with the goal of observing the upper ocean's response to strong storms. Using a moored array in tandem with a fleet of aircraft-deployed Lagrangian drifters, [D'Asaro et al., 1995] documented substantial NIW generation associated with a strong extratropical cyclone in the North Pacific ocean during October 1987. Nominal characteristics of the OS95 storm event are displayed in Table 1. Analysis suggests that β-refraction was the dominant NIW generation mechanism, despite the strong wind-stress curl.

The Near Inertial Shear and KInetic eNergy experiment in the North Atlantic (NISKINe) is an ONR Departmental Research Initiative to investigate the generation, evolution, and dissipation of NIWs in the Iceland Basin. This region was chosen for the strong mesoscale eddy field and stormy weather. Observations from NISKINe suggest that ζ-refraction is often the dominant NIW generation mecha-

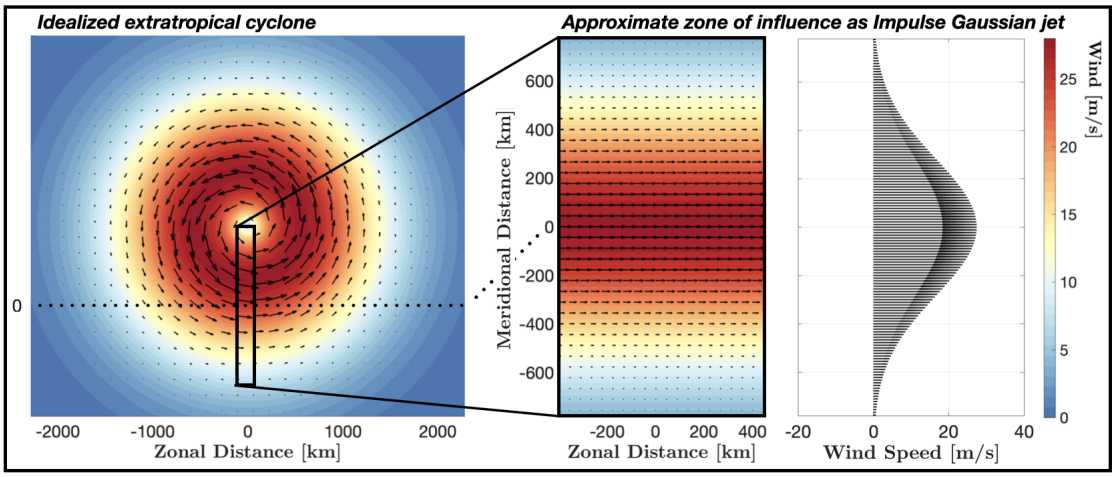

Figure 3.2: A schematic of idealized wind forcing by an extratropical cyclone, as introduced by D'Asaro et al. [1995] in OS95. We idealize the cyclone with radial symmetry, then consider an impulse Gaussian jet associated with the zone of influence of the storm. The zone of influence is denoted by the black rectangle. The storm model is the same in both OS95 and NISKINe, but the magnitude of forcing is different. Forcing magnitude for OS95 is displayed above.

nism as the mesoscale eddy field in the Iceland basin is host to strong eddies with vorticity as large as $\zeta/f \geq 0.3$ [Asselin et al., 2020]. Nominal characteristics of the NISKINe case study are displayed in Table 1.

These two test cases provide examples of strong NIW generation via different mechanisms. OS95 provides context to the more classical storm-generated NIW cases, while NISKINe underscores how strong mesoscale vorticity impacts NIW generation. Throughout the theoretical derivations that follow, we provide contextual examples which draw upon the OS95 and NISKINe test cases. Following development of the theory and model, we use the eKG model to investigate the NIW generation associated with strong storms and mesoscale vorticity. In particular, we explore the OS95 extratropical cyclone and an idealized dipole vortex corresponding to NISKINe observations [Thomas et al., 2020]. In these case studies, our focus is not to replicate the full complexity of the observed dynamics, but to explore the relative interplay between $\nabla \times \tau$, β, and ζ under different idealized forcing conditions. Schematics of the wind and mesoscale forcing for the OS95 and

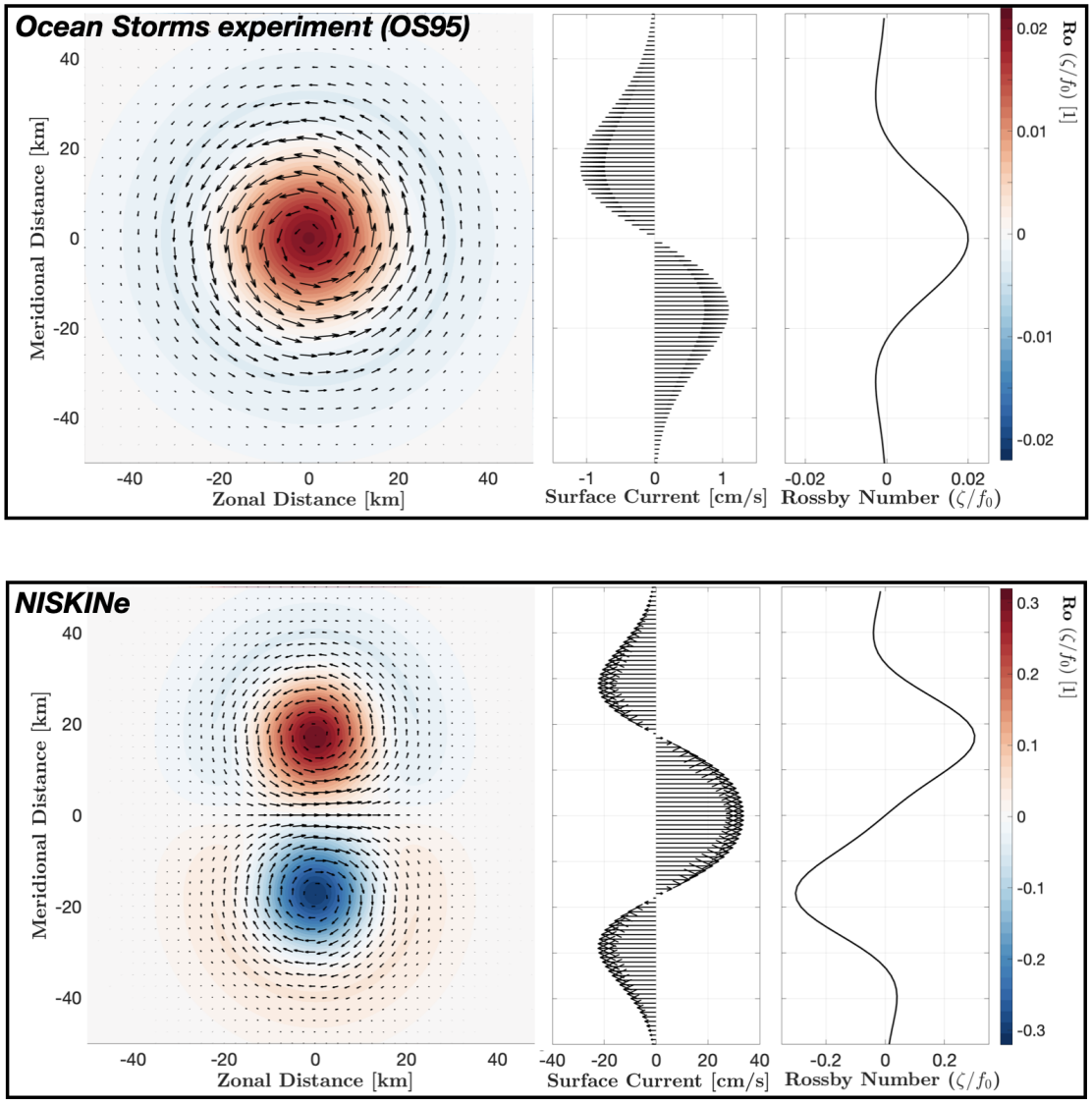

Figure 3.3: Idealized, Gaussian representations of the eddy observed in OS95 [D'Asaro et al., 1995] and the NISKINe dipole vortex [Thomas et al., 2020] are shown. Spatial Rossby number variability is displayed in the color maps. The OS95 storm took place over a region of weak mesoscale eddies, with nominal Rossby number ~ 0.02 and diameter of 100 km. The NISKINe dipole vortex is quite strong with variability of the Rossby number between 0.3 and -0.3. Additional mesoscale characteristics are shown in Table 1. For both cases, meridional profiles of the surface currents and Rossby number are shown in the vertical plots. Note that the spatial axis limits in the color maps are the same for OS95 and NISKINe, but the surface currents and Rossby number are more than an order of magnitude larger in the NISKINe case.

Table 3.1: The parameter space associated with the Ocean Storms experiment [D'Asaro et al., 1995] and NISKINe [Thomas et al., 2020, Klenz et al., 2022] is described. Note that the NISKINe dipole vortex consists of two eddies, so the mesoscale feature width is twice the mesoscale RMS width.

Parameter	**Ocean Storms**	**NISKINe**
Latitude [° N]	47.5	57.8
Ocean Depth, H [m]	4200	3010
Storm RMS Width, L_{storm} [km]	283	283
Peak Wind Stress, τ_{max} [Pa]	2.3	0.8
Inertial Currents, $\lvert\mathbf{u}_F\rvert$ [cm/s]	60	25
Mode-1 Eigenspeed, c [m/s]	2.28	1.59
Rossby Radius, L_{Ro} [km]	21.2	12.9
Mesoscale Feature	Eddy	Dipole
Rossby Number, Ro [1]	0.02	0.3
Eddy RMS Width L_{eddy} [km]	15.9	11.1
Damping Parameter, r^{-1} [days]	7	7

NISKINe case studies are displayed in Figures 3.2 and 3.3, respectively.

3.3 Theory

3.3.1 Governing equations

We are interested in the propagation of internal waves through the ocean's mesoscale. The flow is approximated as Boussinesq, hydrostatic, and rotating on a β-plane. Following Wagner et al. [2017], we expand the equations treating the Rossby number as a small parameter. This expansion separates the slow and fast timescales of the mesoscale and wavefields, respectively, and linearizes the advective terms. After reconstituting the $O(1)$ and $O(\text{Ro})$ equations, the slowly-evolving mesoscale flow evolves according to the standard quasi-geostrophic equation [Wag-

ner et al., 2017], and the rapidly evolving internal wave equations are

$$\frac{\partial \mathbf{u}}{\partial t} + (\overline{\mathbf{u}} \cdot \nabla)\mathbf{u} + f_{\text{eff}}\hat{\mathbf{k}} \times \mathbf{u} = -\nabla p + \frac{\partial \boldsymbol{\tau}}{\partial z}, \tag{3.3.1.1a}$$

$$0 = -\frac{\partial p}{\partial z} + b, \tag{3.3.1.1b}$$

$$\frac{\partial b}{\partial t} + \overline{\mathbf{u}} \cdot \nabla b + wN^2 = 0, \tag{3.3.1.1c}$$

$$\nabla \cdot \mathbf{u} + \frac{\partial w}{\partial z} = 0, \tag{3.3.1.1d}$$

[Savage et al., 2020], where $\mathbf{u} = u\hat{\mathbf{i}} + v\hat{\mathbf{j}}$ and w are the horizontal and vertical velocity, p is pressure (divided by reference density, ρ_0), and $\boldsymbol{\tau}$ is turbulent (Reynolds) stress (divided by reference density). Buoyancy is $b = -g\rho/\rho_0$, where g is gravity and ρ is density. The buoyancy frequency squared is N^2, which is also the vertical gradient of mesoscale buoyancy. The equations are written in Cartesian coordinates, where x, y and z are the zonal, meridional, and vertical directions. The upper and lower boundaries are located at $z = 0$ and $z = -H$, respectively. Wave-wave advection terms have been omitted from (3.3.1.1) because they only force an Eulerian meanflow and second harmonic, which are not presently of interest [Wagner et al., 2017, Savage et al., 2020].

The mesoscale flow in (3.3.1.1) is denoted by an overbar. The small Rossby number approximation eliminates mean vertical velocity, divergence, and strain, which are $O(\text{Ro}^2)$ [Chavanne et al., 2012]. The small Richardson number approximation eliminates terms involving mean flow vertical shear, although it does not require the meanflow to be barotropic. The small Richardson number also ensures stability with respect to symmetric instability. The retained mean flow terms in (3.3.1.1) produce two effects: (i) advecting the internal waves and (ii) altering the effective inertial frequency

$$f_{\text{eff}} = f_0 + \beta y + \zeta/2, \tag{3.3.1.2}$$

through the vertical component of mesoscale vorticity, ζ. The effective inertial frequency also depends on the reference inertial frequency, f_0, and the latitudinal gradient in the inertial frequency, β.

To focus our study on NIW generation via wind stress curl, β refraction, and ζ refraction, we select an idealized setting similar to D'asaro [1995] to eliminate

several effects that primarily affect internal wave propagation. First, we limit our study to a mesoscale flow that is zonal, barotropic, steady, and only varies in the meridional direction $\overline{\mathbf{u}}(x,y,z,t) = \overline{u}(y)\hat{\mathbf{i}}$. Eliminating vertical variability in mesoscale advection and vorticity eliminates internal wave scattering from low to high vertical modes by the mesoscale [Dunphy and Lamb, 2014, Dunphy et al., 2017, Savage et al., 2020]. Next, we ignore topographic variability to eliminate vertical mode scattering by mid ocean ridges and continental slopes [Buijsman et al., 2020, Kelly et al., 2021]. Lastly, we neglect all variability in the zonal direction ($\partial/\partial x \approx 0$) to reduce the flow to two dimensions and eliminate mesoscale advection.

With the above simplifications, the equations of motion become

$$\frac{\partial \mathbf{u}}{\partial t} + f_{\text{eff}}\hat{\mathbf{k}} \times \mathbf{u} = -\frac{\partial p}{\partial y} + \frac{\partial \boldsymbol{\tau}}{\partial z}, \tag{3.3.1.3a}$$

$$0 = -\frac{\partial p}{\partial z} + b, \tag{3.3.1.3b}$$

$$\frac{\partial b}{\partial t} + wN^2 = 0, \tag{3.3.1.3c}$$

$$\frac{\partial v}{\partial y} + \frac{\partial w}{\partial z} = 0, \tag{3.3.1.3d}$$

where the mesoscale only appears in the vorticity ($\zeta = -\partial\overline{u}/\partial y$) that determines f_{eff}.

We represent the internal waves as a sum of vertical normal modes [Gill and Clarke, 1974], which are conveniently uncoupled in our idealized setting,

$$\mathbf{u}(y,z,t) = \sum_{n=1}^{\infty} \mathbf{u}_n(y,t)\phi_n(z), \tag{3.3.1.4a}$$

$$p(y,z,t) = \sum_{n=1}^{\infty} p_n(y,t)\phi_n(z), \tag{3.3.1.4b}$$

where $\mathbf{u}_n$ and p_n are the modal amplitudes, n is the vertical mode number, and $\phi_n(z)$ is the vertical mode [Kelly, 2016]. The vertical modes are orthogonal

$$\frac{1}{H}\int_{-H}^{0} \phi_m\phi_n \mathrm{d}z = \delta_{mn}\ , \tag{3.3.1.5}$$

and determined, along with the eigenspeeds, by solving the Sturm-Liouville prob-

lem

$$\frac{\mathrm{d}^2\Phi_n}{\mathrm{d}z^2} + \frac{N^2}{c_n^2}\Phi_n = 0 \qquad \text{with} \qquad \Phi_n(0) = \Phi_n(-H) = 0 \ , \tag{3.3.1.6}$$

where $\phi_n = \mathrm{d}\Phi_n/\mathrm{d}z$ and $c_n(\mathbf{x})$ is the mode eigenspeed. The rigid-lid approximation in (3.3.1.6) has almost no effect on internal wave dynamics, although it may lead to inconsistencies if it is used when analyzing output from models with a free surface [Kelly, 2016].

Multiplying (3.3.1.3) by ϕ_n and depth averaging produces the modal equation of motion

$$\frac{\partial \mathbf{u}_n}{\partial t} + f_{\text{eff}}\hat{\mathbf{k}} \times \mathbf{u}_n = -\frac{\partial p_n}{\partial y} + \boldsymbol{\tau}_n^w, \tag{3.3.1.7a}$$

$$\frac{\partial p_n}{\partial t} = -c_n^2 \frac{\partial v_n}{\partial y}. \tag{3.3.1.7b}$$

The variable $\boldsymbol{\tau}_n^w$ is given by the projection of an arbitrary wind stress, $\boldsymbol{\tau}_w(\mathbf{x}, z, t)$, onto modes, $\phi_n(z)$, as

$$\boldsymbol{\tau}_n^w = \frac{1}{H}\int_{-H}^{0} \frac{\partial \boldsymbol{\tau}_w}{\partial z}\phi_n \mathrm{d}z. \tag{3.3.1.8}$$

In general, the vertical structure of the wind stress profile is nontrivial, evolves in time, and strongly effects the observed dynamics [D'Asaro et al., 1995]. Strong forcing alters the ML and TL depths through turbulent entrainment and mixing [Price et al., 1986]. Recent work by Stokes et al. [2023] highlights the importance of stress profiles in determining shear production in the OSBL and the amount of energy going into high vertical modes.

The traditional integrated layer 'slab' model [Pollard and Millard, 1970, Plueddemann and Farrar, 2006] parameterizes wind forcing through a constant stress divergence in the ML ($z > -H_{\text{mix}}$) and numerous damping processes through a catch-all linear (Rayleigh) drag, r [Plueddemann and Farrar, 2006]. This formulation is useful as the integral in (3.3.1.8) can be solved in closed form so that the stress projection is

$$\begin{aligned}\boldsymbol{\tau}_n^w &= \frac{1}{H}\int_{-H_{\text{mix}}}^{0} \frac{\boldsymbol{\tau}_w}{H_{\text{mix}}}\phi_n \mathrm{d}z - \frac{1}{H}\int_{-H}^{0} r\mathbf{u}\phi_n \mathrm{d}z \\ &= \alpha_n \boldsymbol{\tau}_w - r\mathbf{u}_n \ ,\end{aligned} \tag{3.3.1.9}$$

where $\tau_w(y,t)$ is wind stress and $\alpha_n = \phi_n(0)/H$ determines the effective forcing on each vertical mode. Alternative stress profiles can also be specified, either through parameterizations, turbulence closure models, or observations, which will change the value of α_n. Stokes et al. [2023].

Since all vertical modes are uncoupled, we can solve (3.3.1.7) for each individual mode. The resulting solutions only differ due to eigenspeed (c_n^2) and forcing (α_n). Thus, we drop modal subscripts in the remainder of this analysis and analyze a single arbitrary mode, which propagates as a linear shallow water wave.

In the analysis of mean flows, it is standard to separate the acceleration (due to Coriolis) into an Ekman component which is balanced by stress divergence, and a geostrophic component which is balanced by the pressure gradient. Here we generalized this procedure to time varying flows and define

$$\left(\frac{\partial}{\partial t} + r\right)\mathbf{u}_F + f_{\text{eff}}\hat{\mathbf{k}} \times \mathbf{u}_F = \alpha\boldsymbol{\tau}_w, \tag{3.3.1.10a}$$

$$\frac{\partial \mathbf{u}'}{\partial t} + f_{\text{eff}}\hat{\mathbf{k}} \times \mathbf{u}' = -\frac{\partial p}{\partial y} \tag{3.3.1.10b}$$

$$\frac{\partial p}{\partial t} + c^2\frac{\partial v'}{\partial y} = -c^2\frac{w}{H}\,, \tag{3.3.1.10c}$$

where F subscripts and primes indicate forced (Ekman) and wave (geostrophic) components of the flow [Kelly, 2019]. We have also re-defined the vertical velocity, $w = H\partial v_F/\partial y$, as the 'inertial pumping' that arises due to horizontal variability in the transport of the forced flow. We note that the forcing due to $\frac{w}{H}$ is actually independent of depth, so (3.3.1.10) only depends on H through the modal forcing coefficient, α.

3.3.2 Inertial pumping

(3.3.1.10a) is a 1D damped forced oscillator that can be solved at each horizontal location [e.g., Pollard and Millard, 1970, Alford, 2001, Plueddemann and Farrar, 2006, Kelly, 2019]. The convergence and divergence of the currents creates inertial pumping that generates near-inertial waves. Inertial pumping depends on the wind stress, β and ζ. The wind stress associated with atmospheric storms is a particularly effective inertial pump. [Gill, 1984, D'Asaro et al., 1995, Brizuela

et al., 2022]. Gill [1984], D'Asaro et al. [1995]; and others have shown it reasonable to approximate a fast moving storm as an impulse forcing event. For a simplified model, we represent the wind stress associated with a storm as an impulse of Gaussian zonal wind stress centered at $y = 0$, with width L,

$$\boldsymbol{\tau}_w(y,t) = A \exp\left(\frac{-y^2}{2L_{\text{storm}}^2}\right) \delta(t)\hat{\mathbf{i}} \tag{3.3.2.1}$$

where $A = \tau_{\text{storm}}\Delta T_{\text{storm}}$ is the wind stress multiplied by the storm duration. For reference, D'asaro [1995] used $\tau_{\text{storm}} = 2.3$ Pa, $\Delta T_{\text{storm}} = 0.5$ days, and $L_{\text{storm}} = 280$ km to replicate the inertial response during the Ocean Storms experiment [note that D'asaro [1995] used a different width convention and prescribed $\sqrt{2}L_{\text{storm}} = 400$ km].

We also include a mesoscale eddy with vorticity

$$\zeta(y) = \zeta_0 \exp\left(-\frac{y^2}{2L_{\text{eddy}}^2}\right) , \tag{3.3.2.2}$$

which is centered at $y = 0$ and has an root-mean-squared width of L_{eddy}. In the Ocean Storms case, we use a nominal mesoscale eddy where $\zeta \sim 0.02 f_0$ and the eddy diameter is 100 km, so that $L_{\text{eddy}} = 100/(2\pi)$ For reference the dipole vortex observed by Thomas et al. [2020], had $\zeta_0 = 0.3 f_0$ and $L_{\text{eddy}} \approx 70$ km.

Inserting this wind stress and vorticity into (3.3.1.10a) and solving for the meridional velocity produces

$$u_F(y,t) = \alpha A \cos(f_{\text{eff}} t) \exp\left(\frac{-y^2}{2L_{\text{storm}}^2} - rt\right) \Theta(t) \tag{3.3.2.3a}$$

$$v_F(y,t) = -\alpha A \sin(f_{\text{eff}} t) \exp\left(\frac{-y^2}{2L_{\text{storm}}^2} - rt\right) \Theta(t) \tag{3.3.2.3b}$$

where $\Theta(t)$ is the Heaviside function. The inertial pumping, $w = H\partial v_F/\partial y$ is then

$$\begin{aligned} w(y,t) = \Bigg[& \frac{y}{L_{\text{storm}}^2} \sin(f_0 t) - \beta t \cos((f_0 + \beta y)t) \\ & + \frac{\zeta_0 y}{2L_{\text{eddy}}^2} \exp\left(-\frac{y^2}{2L_{\text{eddy}}^2}\right) t \cos(f_{\text{eff}} t) \Bigg] \\ & \times \alpha H A \exp\left(-\frac{y^2}{2L_{\text{storm}}^2} - rt\right) \Theta(t) , \end{aligned} \tag{3.3.2.4}$$

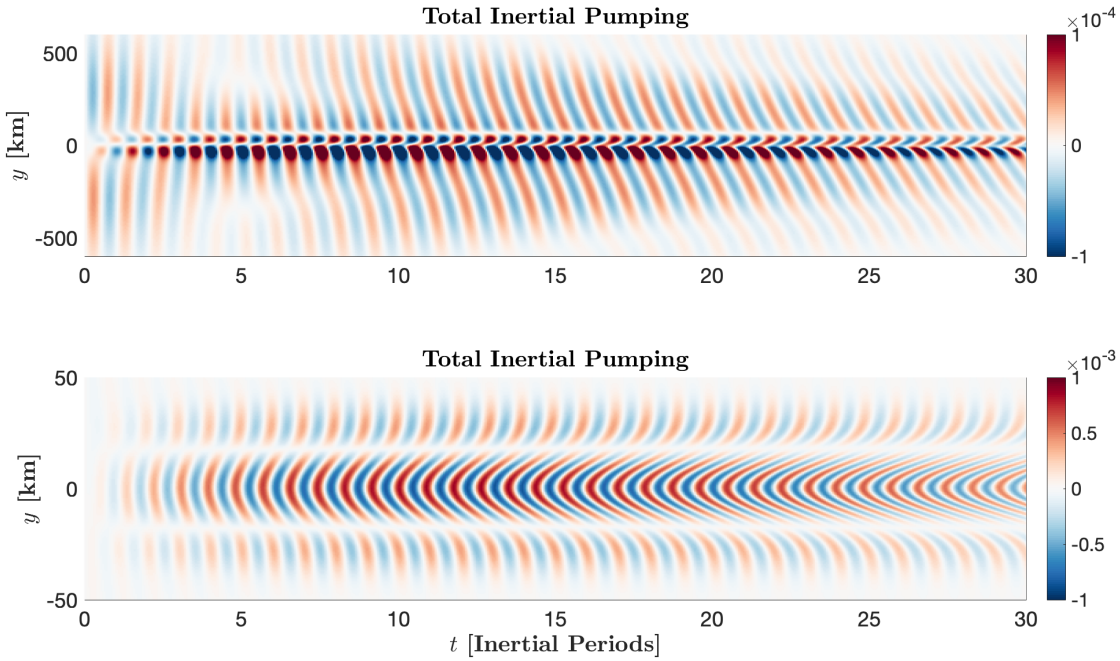

Figure 3.4: Total inertial pumping is shown for the OS95 and NISKINe test cases in the top and bottom panels, respectively. Conditions for the numerical simulations are given in Table 1. Inertial pumping is dominated by β and strongly enhanced by ζ in OS95. In the NISKINe case, inertial pumping is dominated by ζ.

where the first term is due to the wind stress curl, the second term β refraction, and the third term ζ refraction. Note that at $y = L_{\text{eddy}}$, the third term is maximum and equal to $\zeta_0/2L_{\text{eddy}}t\cos(f_{\text{eff}}t)$. That is, $\zeta_0/2L_{\text{eddy}}$ acts like an effective β. Each component [term] of w is shown individually in Figures 3.5 and 3.6 for 30 inertial periods in the OS95 and NISKINe, respectively. The net inertial pumping (e.g. 3.3.2.4) for either case is shown in Figure 3.4.

In the time domain, inertial pumping due to wind stress alone simply oscillates near the inertial frequency, with a spatial pattern that matches the storm. For a Gaussian storm, the wind stress curl has a dominant wavelength of $2\pi L_{\text{storm}}$. β refraction leads to a wavelength that shrinks in time, so that inertial pumping looks like a spatially periodic wave-maker being dragged toward the equator. ζ refraction is similar to β refraction, except the wavelength shrinks at a rate proportional to the vorticity gradient and it looks like a wave-maker being dragged from cyclonic

to anticyclonic regions (i.e., from regions of high to low f_{eff}).

Inertial pumping forces the wave equation (3.3.1.10c). The forcing is most effective at generating internal waves when it lies along the dispersion curve. When ζ and β are not too large (see next section), the dispersion relation can be approximated as

$$\omega^2 = f^2 + c^2 l^2 \tag{3.3.2.5}$$

[Pedlosky, 2003], where ω is the frequency and l is the meridional wavenumber. One can then compare the power spectral density of the three components of w in (3.3.2.4) to the dispersion curve. We show these spectra alongside mode-1 and mode-4 dispersion curves for the OS95 and NISKINe cases in Figures 3.5 and 3.6, respectively. For low modes, β and ζ refraction can cause forcing at high wavenumbers that lie below the dispersion curve. That is, the high wavenumber forcing occurs too close to the inertial frequency to excite internal waves. This forcing may excite higher modes, which have smaller eigenspeeds and flatter dispersion curves, but high-mode generation is ultimately limited by α, which is set by the vertical profile of stress and typically decreases rapidly with mode number [Stokes et al., 2023]. For example, if the wind is blowing over a very deep ML there is very little high mode forcing, even if the mesoscale vorticity produces variability at the right wavelengths for high-mode generation.

3.3.3 Wave generation and propagation

The equations governing wave dynamics in (3.3.1.10) are identical to those governing internal-tide generation under the weak-topography approximation [Llewellyn Smith and Young, 2002], except w is driven by convergence and divergences in a wind driven flow rather than the barotropic tide flowing up and down topography and the equations depend on f_{eff}, which varies in y, instead of a constant f_0 (i.e., the f-plane approximation). The wave equations may be combined into a single

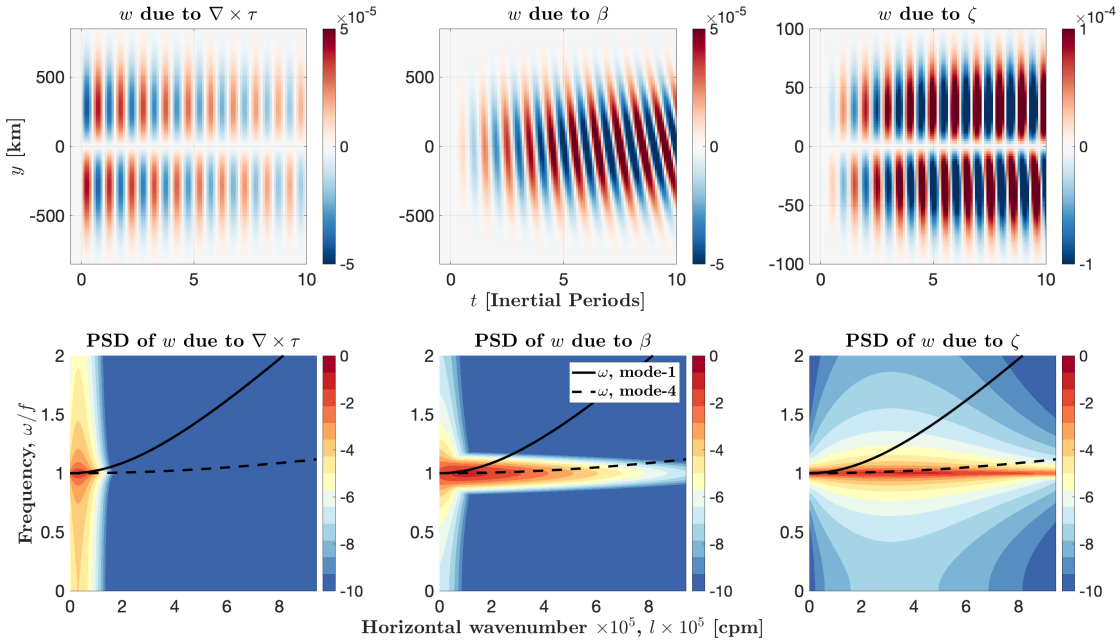

Figure 3.5: Inertial pumping decomposition (panel a: wind-stress curl, panel b: β-refraction, panel c: ζ-refraction) is shown for parameter space associated with OS95 (see the Ocean Storms column of Table 1). The simulation runs for 200 inertial periods; the first 10 are shown (x-axis). Meridional distance (y) is plotted on the y-axis, with negative values representing southward displacements from the origin, and positive values northward displacements. The bottom row, panels d-f, show the power spectral density (PSD) associated with each component of the inertial pumping; wind-stress curl, β-refraction, and ζ-refraction, respectively. The mode-1 and mode-4 dispersion curves are plotted as solid and dashed black lines, respectively. Internal waves are generated where non-negligible PSD overlaps with the dispersion curve. Note the different y-axis and colorbar bounds in the inertial pumping decomposition plots (top row).

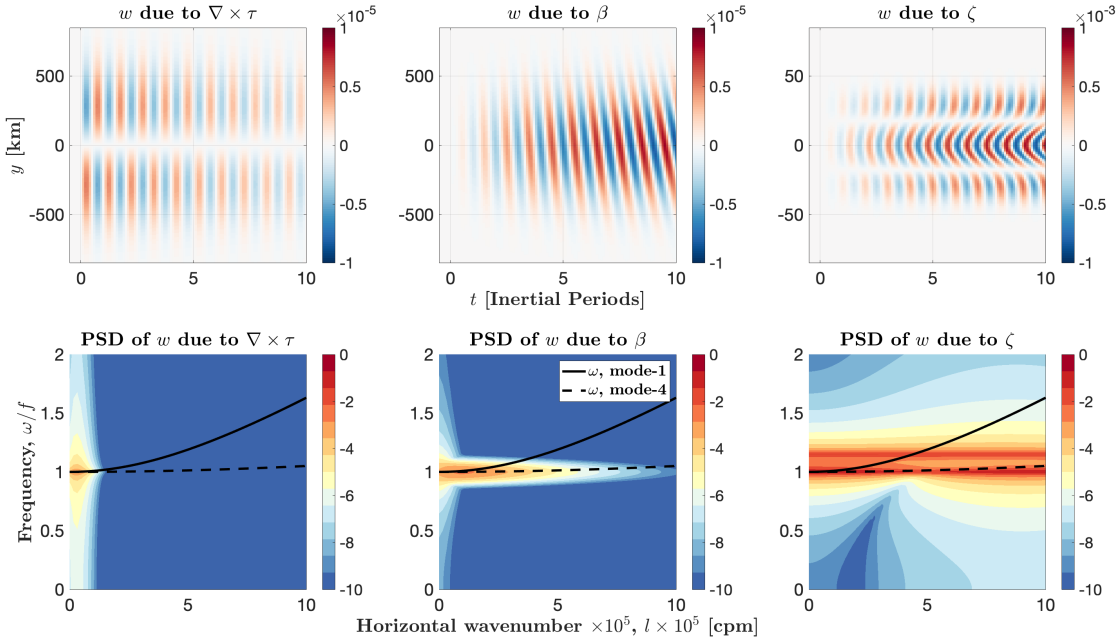

Figure 3.6: Inertial pumping decomposition (panel a: wind-stress curl, panel b: β-refraction, panel c: ζ-refraction) is shown for parameter space associated with NISKINe (see the NISKINe column of Table 1). The simulation runs for 200 inertial periods; the first 10 are shown (x-axis). Meridional distance (y) is plotted on the y-axis, with negative values representing southward displacements from the origin, and positive values northward displacements. The bottom row, panels d-f, show the power spectral density (PSD) associated with each component of the inertial pumping; wind-stress curl, β-refraction, and ζ-refraction, respectively. The mode-1 and mode-4 dispersion curves are plotted as solid and dashed black lines, respectively. Internal waves are generated where non-negligible PSD overlaps with the dispersion curve. Note the different y-axis and colorbar bounds in the inertial pumping decomposition plots (top row).

equation

$$\left(\frac{\partial^2}{\partial t^2}+f_{\text{eff}}^2\right)^2\frac{\partial p}{\partial t}-\left(\frac{\partial^2}{\partial t^2}+f_{\text{eff}}^2\right)c^2\frac{\partial^2}{\partial y^2}\frac{\partial p}{\partial t} \\ +c^2\frac{\partial f_{\text{eff}}^2}{\partial y}\frac{\partial}{\partial y}\frac{\partial p}{\partial t}=-\left(\frac{\partial^2}{\partial t^2}+f_{\text{eff}}^2\right)^2 c^2\frac{w}{H}\,, \tag{3.3.3.1}$$

[Pedlosky, 2003]. These equations are nearly a forced Klein-Gordon equation, except the third term has been added due to variability in the effective inertial frequency. We refer to (3.3.3.1) as the extended Klein-Gordon (eKG) equation.

On an f-plane without a mean flow, $\partial f_{\text{eff}}^2/\partial y = 0$, and the third term on the right hand side of (3.3.3.1) vanishes. In this case, we recover the standard Klein-Gordon (KG) equation

$$\left(\frac{\partial^2}{\partial t^2}+\left(f_0+\frac{\zeta}{2}\right)^2\right)\frac{\partial p}{\partial t}-c^2\frac{\partial^2}{\partial y^2}\frac{\partial p}{\partial t}=-\left(\frac{\partial^2}{\partial t^2}+\left(f_0+\frac{\zeta}{2}\right)^2\right)c^2\frac{w}{H}\,, \tag{3.3.3.2}$$

as derived, and solved, by Llewellyn Smith and Young [2002] to describe internal tide generation. This equation produces the traditional inertia-gravity wave dispersion relation for shallow water waves.

Extending the Klein-Gordon internal tide generation formalism to describe NIW generation

Llewellyn Smith and Young [2002] solved (3.3.3.2) using vertical velocities (w) generated by a spatially-uniform oscillating barotropic tide (u_0) over Gaussian and Witch of Agnesi ridges to model the conversion of the barotropic tide to internal tides ('conversion' is equivalent to 'internal wave generation'). To apply these results, we must find the wind stress $\boldsymbol{\tau}(\mathbf{x},t)$ that produces vertical velocities equal in magnitude as those generated in the tidal problem. If the wind stress is purely zonal, oscillates in time, and only varies in the meridional direction then we can write $\boldsymbol{\tau}_w(\mathbf{x},t)=\tau_x(y)e^{-i\omega t}\hat{\mathbf{i}}$. Substituting this into (3.3.1.10a) produces the forced velocities

$$u_F(y,t)=\frac{-i\omega}{\omega^2-f^2}\tau_x e^{-i\omega t} \tag{3.3.3.3a}$$

$$v_F(y,t)=\frac{f}{\omega^2-f^2}\tau_x e^{-i\omega t} \tag{3.3.3.3b}$$

The vertical velocity is obtained from (3.3.1.3d) as

$$w(y,t) = \frac{-1}{\omega^2/f^2 - 1}\frac{\partial}{\partial y}\left(\frac{\tau_x}{f}\right)e^{-i\omega t}\ . \tag{3.3.3.4}$$

Evidently, a wind-stress curl is analogous to a topographic slope. We write both the topography and wind stress as Gaussian

$$H = H_0 - h_{\max}e^{-\frac{1}{2}\left(\frac{y}{L}\right)^2} \tag{3.3.3.5a}$$

$$\tau_x = \tau_{\max}e^{-\frac{1}{2}\left(\frac{y}{L}\right)^2} \tag{3.3.3.5b}$$

where L is the RMS width of the feature (storm or ridge). The vertical velocities are now

$$w_{\text{tide}} = -\left[u_0 h_{\max}\right]\frac{y}{L^2}e^{-\frac{1}{2}\left(\frac{y}{L}\right)^2}e^{-i\omega t} \tag{3.3.3.6a}$$

$$w_{\text{wind}} = \left[\frac{\tau_{\max}/f}{\omega^2/f^2 - 1}\right]\frac{y}{L^2}e^{-\frac{1}{2}\left(\frac{y}{L}\right)^2}e^{-i\omega t} \tag{3.3.3.6b}$$

where the quantities in brackets can be compared. In the ocean, a reasonable internal-tide generation problem might involve a 1 cm/s barotropic current flowing over a 1000 m tall ridge, yielding $u_0 h_{\max} \approx 10$. In comparison, a 0.1 Pa wind stress at 44° latitude with a frequency $\omega/f = 1.05$ also yields $\frac{\tau_{\max}/f}{\omega^2/f^2-1} \approx 10$.

Analytical solution to the Klein-Gordon equation

Analytical solutions to (3.3.3.2) are derived in Llewellyn Smith and Young [2002] and Pollmann et al. [2019]. The Klein-Gordon equation is valid on an f-plane, so $f_{\text{eff}} \longrightarrow f_0$. The equation is solved in the frequency domain using the Fourier transform pair

$$\hat{p}(\omega) = \int_{-\infty}^{\infty} p(t)e^{-i\omega t}\mathrm{d}t, \tag{3.3.3.7a}$$

$$p(t) = \frac{1}{2\pi}\int_{-\infty}^{\infty} \hat{p}(\omega)e^{-i\omega t}\mathrm{d}\omega\ , \tag{3.3.3.7b}$$

for pressure, and an analogous Fourier transform pair for the vertical velocity source function, $\hat{w}(\omega)$. The Green's function is

$$G(y,y') = \frac{e^{i\kappa|y-y'|}}{2i\kappa}\ , \quad \text{where} \quad \kappa \equiv \sqrt{1 - \frac{f_0^2}{\omega^2}}\frac{\omega}{c}, \tag{3.3.3.8}$$

is the meridional wavenumber of a free wave with frequency ω. Pressure is then computed as

$$\hat{p}(y,\omega) = -c_g \frac{1}{2H} \int_{-\infty}^{\infty} e^{i\kappa|y-y'|} \hat{w}(y',\omega) \mathrm{d}y' \; . \tag{3.3.3.9}$$

The key quantity of interest is the near-inertial wave generation, which represents the power going into the near-inertial wave field. This is generically defined

$$\hat{C}(\omega) = -\rho_0 \frac{1}{2} \int_{-\infty}^{\infty} (\hat{w}\hat{p}^* + \hat{w}^*\hat{p}) \, \mathrm{d}y \; , \tag{3.3.3.10}$$

where a star superscript denotes the complex conjugate and the negative sign indicates that internal wave generation is associated with downward energy flux.

Llewellyn Smith and Young [2002] prove that for a 1D source function ($\hat{w}(\omega)$), the spatially integrated conversion (3.3.3.10) simplifies to

$$\hat{C}(\omega) = c_g \frac{\rho_0 |\hat{w}(\kappa)|^2}{2H} \tag{3.3.3.11}$$

which is just the energy associated with inertial pumping times the group speed

$$c_g \equiv \sqrt{1 - \frac{f_0^2}{\omega^2}} c \; . \tag{3.3.3.12}$$

K-G solutions for a 1D, idealized Gaussian storm:

For an arbitrary storm, we approximate the forcing as an impulse and obtain the total generation by integrating over all frequencies

$$C = \int_{-\infty}^{\infty} \hat{C}(\omega) \mathrm{d}\omega \quad [\mathrm{W/(m - storm\ length)}] \; . \tag{3.3.3.13}$$

Solution of (3.3.3.13) requires specification of w. We are interested in NIW generation by a 1D, idealized, Gaussian storm over a mesoscale eddy field, e.g. C(τ, β, ζ), so w is related to the inertial pumping and given in (3.3.2.4). We take the Fourier transform of the inertial pumping to find the source function $\hat{w}(\omega)$, written in terms of the variable κ as

$$\hat{w}(\kappa) = \sqrt{2\pi} L \frac{\boldsymbol{\tau}_w}{f_0} \left[\frac{\xi^2}{(1 - ir^*\xi)^2 - \xi^2} \right] \kappa e^{-\frac{1}{2}(L\kappa)^2}, \tag{3.3.3.14}$$

where the notations $\xi = f_0/\omega$ and $r^* = r/f_0$ are introduced for simplicity. NIW generation, is found by inserting (3.3.3.14) into (3.3.3.11) and evaluating the integral in (3.3.3.13).

A crucial distinction between the work presented and that of Llewellyn Smith and Young [2002] is that the model derived in Llewellyn Smith and Young [2002] is inviscid. By invoking the Ekman-geostrophic decomposition in the model we have constructed, the vertical velocity source function which forces the Klein-Gordon equation is derived from a damped slab, e.g. (3.3.1.10). This allows us to extend the work of Llewellyn Smith and Young [2002] and employ the analytical Klein-Gordon solutions in a damped flow regime to validate our damped numerical model against theory and explore how damping effects internal wave generation.

A natural quantity to compare C with is the total wind work

$$\begin{aligned}\Pi &= \int_{-\infty}^{\infty} \frac{\rho_0 H}{2} |u_F(y,0)|^2 \mathrm{d}y \\ &= \frac{\rho_0 H}{2} |\alpha A|^2 \sqrt{\pi} L_{\mathrm{storm}},\end{aligned} \tag{3.3.3.15}$$

which is just the meridional integral of the forced flow energy at $t = 0$, calculated in the time domain. Note that for a specified stress profile, wind work only depends on the storm width, wind forcing, and bottom depth. Stress profile effects the wind work through modulation of the variable α [Stokes et al., 2023].

The fraction of energy dissipated by the forcing flow

$$q = 1 - \frac{C}{\Pi}, \tag{3.3.3.16}$$

is expected to vary greatly because C is a sensitive function of β, ζ, f_0 and r (through w), while Π is not. This variable is analogous to the 'locally dissipated fraction,' also denoted q, discussed by Alford [2020b].

3.4 Numerical Experiments

We use the eKG model to investigate how the interplay between forcing, damping, and the mesoscale impacts near-inertial internal wave generation. We begin by comparing our model output with analytical K-G solutions from Llewellyn Smith

and Young [2002] to evaluate agreement between theory and numerics. This exercise highlights how the strength of damping affects the numerical solutions. Following model validation, the OS95 and NISKINe test cases are explored with model runs and spectral analysis to assess the energetic volume NIW generation and scales of the generated waves. These case studies provide contextual visualization of NIW generation and propagation under β-dominated and ζ-dominated regimes, respectively. Finally we investigate how storm size, β, and ζ are coupled to NIW generation in a generalized numerical experiment where storm size is varied with and without mesoscale vorticity, on f- and β-planes.

3.4.1 Numerical solutions

To calculate the NIW generation and propagation associated with synoptic storm events, we solve (3.3.3.1) numerically. The inertial pumping, w, forces (3.3.3.1) and must be calculated first. For a 1D meridional grid, this can be done directly through (3.3.2.4), producing a time-variable forcing map (e.g. Figure 3.4). This 1D spatiotemporal map of w is inserted into (3.3.3.1), which is solved on the grid using third-order Adams-Bashforth and fourth order Adams-Moulton time-stepping algorithms and time constants consistent with regional ocean modeling software [ROMS; Shchepetkin and McWilliams, 2005].

3.4.2 Model validation

To validate our model, the analytical K-G solution is calculated for the OS95 case on an f-plane with variable damping (recall that the K-G equation is not valid on a β-plane). The analytical and numerical solutions agree with respect to NIW generation (C) and the local dissipation (q), shown in the top and bottom panels of Figure 3.7, respectively.

Choice of f- or β-plane approximations has a substantial impact on NIW generation in the case of the OS95 storm. As the storm size decreases (i.e. Figure 3.14), the f-plane and β-plane curves for C and q converge. Because the eKG model allows for analysis on a β-plane and recovers the analytical results on an

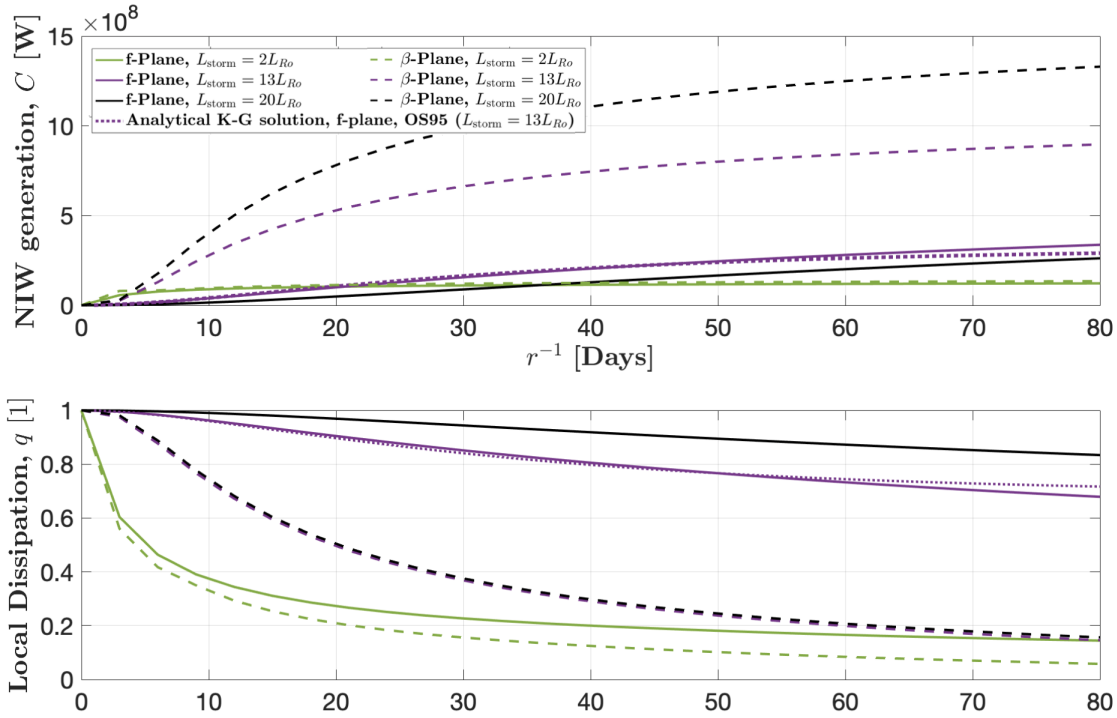

Figure 3.7: Near inertial wave generation (C, top panel) and the associated local dissipation (q, bottom panel) are calculated for parameters associated with the Ocean Storms experiment (OS95; purple lines. See Table 1 for parameter details. $L_{\text{storm}} = 13\ L_{Ro} \sim 280$ km), without consideration of mesoscale vorticity on f-plane and β-plane approximations (solid and dashed lines, respectively). The Rossby radius ($L_{Ro} = 21.1$ km) is calculated for the Ocean storms mode-1 eigenspeed, $c = 2.28$ m/s. Calculations are additionally performed for small and large storms ($L_{\text{storm}} = 2\ L_{Ro} \sim 42$ km, green lines; $L_{\text{storm}} = 20\ L_{Ro} \sim 424$ km, black lines) for comparison. The analytical Klein-Gordon solution is shown for the OS95 case with a purple dashed line.

f-plane for small storms, we conclude that our model is valid for analysis of NIW generation on a β-plane.

Including ζ is appropriate for both the KG and eKG equations, because ζ does not impact the governing equations from which these are derived. ζ simply modifies the effective Coriolis parameter, f_{eff}, and the forcing function, w Therefore ζ and can be considered without issue in both f- and β-plane approximations [Reznik, 2010].

3.4.3 Model sensitivity to linear damping

We explore the effect of damping on NIW generation and dissipation, on an f-plane and a $\beta-$plane for three storm sizes, ignoring mesoscale vorticity (i.e. $\zeta = \text{Ro} = 0$). $L_{\text{storm}} = 13L_{\text{Ro}}$ is the middle storm size, corresponding to OS95 observations [D'Asaro et al., 1995]. $L_{\text{storm}} = 2\ L_{\text{Ro}}$ and $L_{\text{storm}} = 20\ L_{\text{Ro}}$ are selected for small and large storm test cases, respectively. Results from this experiment are shown in Figure 3.7. To supplement these results, we keep storm size and strength fixed using the OS95 parameter space, and then allow the damping parameter to vary through a broad range, from $r^{-1} = 1$ day to $r^{-1} = 5$ years. Results from this experiment are shown in Figure 3.8.

The study of response to variable damping as storm size and strength are fixed allows us to establish the 'inviscid' range of $r^{-1} \geq 1$ year, as generation changes very little between $r^{-1} = 1$ year and $r^{-1} = 5$ years. In the inviscid limit (i.e. $r = 0$, $r^{-1} \longrightarrow \infty$), all the wind work is radiated on both the f-plane and beta-plane, and local dissipation becomes negligible (i.e. $q \longrightarrow 0$). This trend is seen in the bottom panel of Figure 3.7. Literature estimates of damping range from $r^{-1} \sim$ 3-14 days, where a damping parameter of two weeks is thought of as nearly inviscid [Plueddemann and Farrar, 2006]. In Figure 3.8, we see that for the OS95 case, varying r^{-1} from 2 weeks to the inviscid limit causes an associated increase in NIW generation by a factor of ~ 2.5.

The effect of variable damping on generation is even more strongly enhanced within the 'realistic' range of damping values, where $r^{-1} \sim$ 3-14 days. In the OS95 case, there is an order of magnitude of variation in C over this range. Looking at

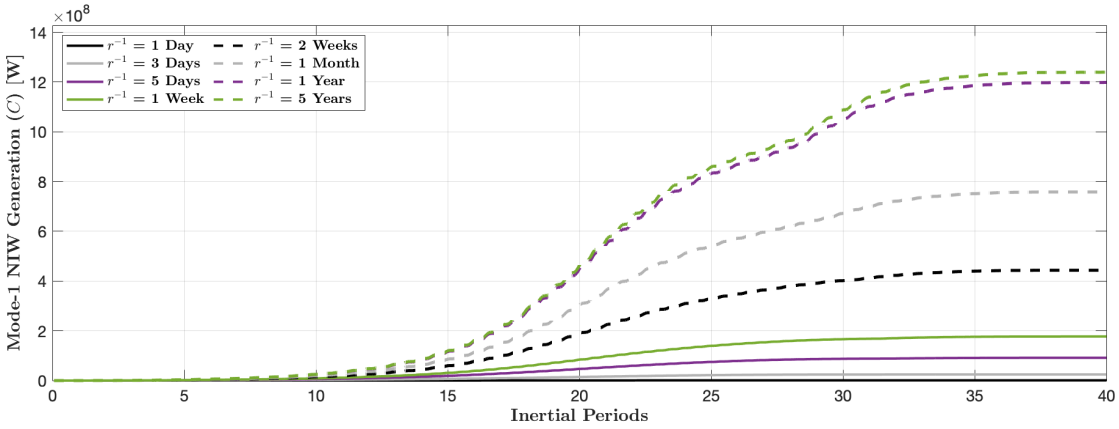

Figure 3.8: Near inertial wave generation (C), is plotted against inertial periods for a range of linear damping values under the OS95 parameter space on a β-plane.

the curve for q in the bottom panel of Figure 3.7, we see that damping has a huge impact on the local dissipation as well. For the 'nearly inviscid' case of $r^{-1} = 14$ days, about 30 percent of the NIW energy is dissipated locally for small storms and 60 percent of the NIW energy is dissipated for large storms.

These results are striking because previous studies of near-inertial wave generation have focused on the perfectly inviscid case. The results here indicate that even a minute amount of damping has a large impact on internal-wave generation and local dissipation. Without endorsing the specific choice of linear drag that was used here, we caution that a model's damping parameterization greatly impacts near-inertial wave generation.

3.4.4 OS95 and NISKINe case studies

We now apply the eKG model to the OS95 and NISKINe settings. Stratification, inertial currents, and vertical wavenumber spectra for OS95 and NISKINe are shown in Figure 3.9. OS95 is much more stratified than NISKINe, by about an order of magnitude in N^2. The storm associated with OS95 produced stronger inertial currents, by more than a factor of 2. These motions are intensified in the low modes, likely due to the deeper ML of OS95 (35 m in OS95, 10 m in NISKINe). The relative importance of high-vs-low modes is shown in the vertical wavenumber

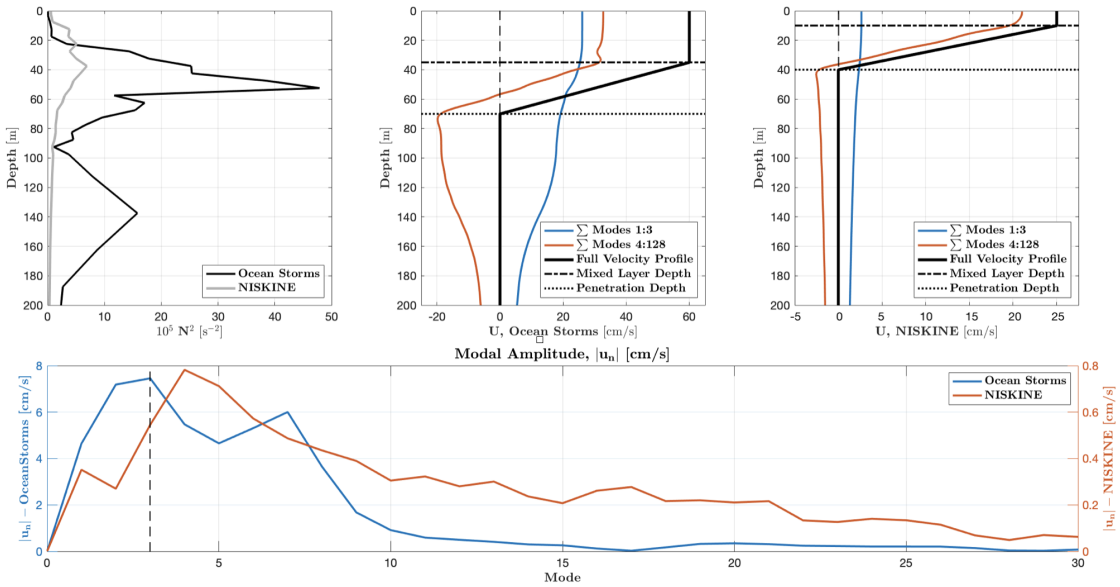

Figure 3.9: **Panel a:** Stratification for OS95 and NISKINe are shown with the black and grey lines, respectively. **Panel b:** Total inertial currents for OS95 are shown with the black line, with nominal ML currents of $\sim$ 60 cm/s. A modal decomposition of these currents is displayed for radiative modes (1-3) and dissipative modes (4-∞) with the blue and red lines, respectively. The inertial currents have comparable contributions from the radiative and dissipative modes. **Panel c:** Total inertial currents for NISKINe are shown with the black line, with nominal ML currents of $\sim$ 25 cm/s. A modal decomposition of these currents is displayed for radiative modes (1-3) and dissipative modes (4-∞) with the blue and red lines, respectively. The inertial currents are dominated by the dissipative (high-mode) contributions. **Panel d:** Vertical wavenumber spectra are shown for OS95 and NISKINe with the blue and red lines, respectively.

spectra as well; the OS95 dynamics can be resolved with $\sim$ 15 modes while NISKINe requires $>$ 30 modes. The differences in these cases provide an instructive set of observations with which to explore the utility of our numerical model.

Ocean Storms Experiment

We assess the dynamics associated with the large extratropical cyclone observed by D'Asaro et al. [1995] in the North Pacific during October 1989 (e.g. the Ocean Storms experiment, hereafter OS95). We approximate the impact of the storm as an impulse Gaussian jet with RMS width of 283 km (see Fig. 3.2). For a

characteristic length scale, we use the mode-1 Rossby radius, given by c_n/f, which is $\mathrm{Ro}_1 = 21.2$ km (Table 1). The inertial period at the latitude of observations (47.5 N) is 16.2 hours, which serves as the characteristic time scale of the analysis. We have established that dynamics are the same between different modes, except that the Rossby radius shrinks as the eigenpseed, c_n, becomes smaller. Here, we focus our study on the evolution of mode-1, the most dispersive mode, with reference to modes 4 and 10 for context.

In our simulations, the storm is modeled as an impulse and prescribed analytically using (3.3.2.4). We use a 2 km grid with 6000 grid points. For consistency with Stokes et al. [2023] we set damping to $r^{-1} = 7$ days. Performing calculations under both the β-plane approximation and the f-plane approximation allows us to estimate the NIW generation associated with β-refraction. The OS95 observations occur in an area of weak mesoscale eddies with near-surface RMS vorticity of about 0.02 f_0 [D'asaro, 1995]. To explore possible effects of NIW generation via ζ-refraction, we include the option to superpose a mesoscale eddy in our simulation domain. We set the nominal eddy diameter to 100 km with a Rossby number Ro = 0.02 for consistency with the length scales of a typical mesoscale eddy [Rhines, 2001] and observed local vorticity in OS95 [D'asaro, 1995].

Model output for mode-1 NIW generation associated with the OS95 test case is shown in Figure 3.10. Throughout a majority of the domain, the inertial pumping signal is dominated by $\nabla \times \tau$ and β. However, local enhancement by ζ contributes strongly to the inertial pumping in the neighborhood of the eddy. Inertial pumping due to $\nabla \times \tau$ and β is maximized 100 km north or south of the storm's core, negligible at locations outside of the storm, and decays to negligible values for times greater than 50 inertial periods after the storm. This is consistent with the mode-1 NIW generation, which suggests that NIW generation ceases after 30 inertial periods as the forced velocities decay through drag. This decay limits the generation of extremely long near-inertial waves with extremely slow group speeds.

The group velocity of the generated waves can be extracted from the slope of the cone of pressure fluctuations. Phase velocity is extracted as the slope of individual bands of constant pressure. As the waves propagate southwards, group velocity

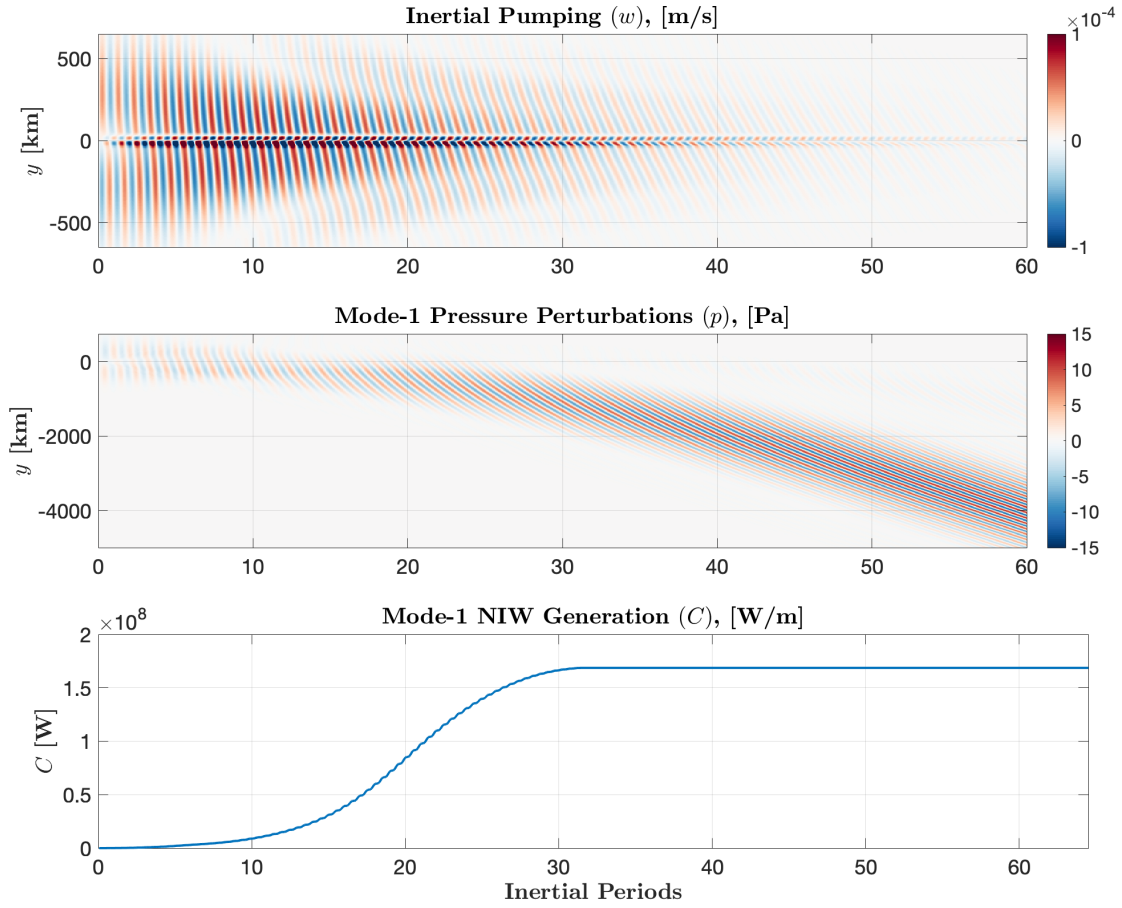

Figure 3.10: Model output for mode-1 NIW generation associated with the Ocean Storms Experiment test case is shown. For all cases, time is given as inertial periods on the x-axis. **Top panel:** Inertial pumping (w) is shown as a function of distance [km north/south, y-axis] and time. Peak vertical velocities of 2.6×10^{-4} cm/s are observed after 10 inertial periods, beyond which inertial pumping decays exponentially. **Middle panel:** Pressure fluctuations associated with the NIWs are shown as a function of distance [km north/south, y-axis] and time. Group velocity is extracted as the slope of the cone, and phase velocity is extracted as the slope of individual isobars. **Bottom panel:** Total NIW flux (generation) is calculated for the domain. After $\sim$ 30 inertial periods, generation ceases.

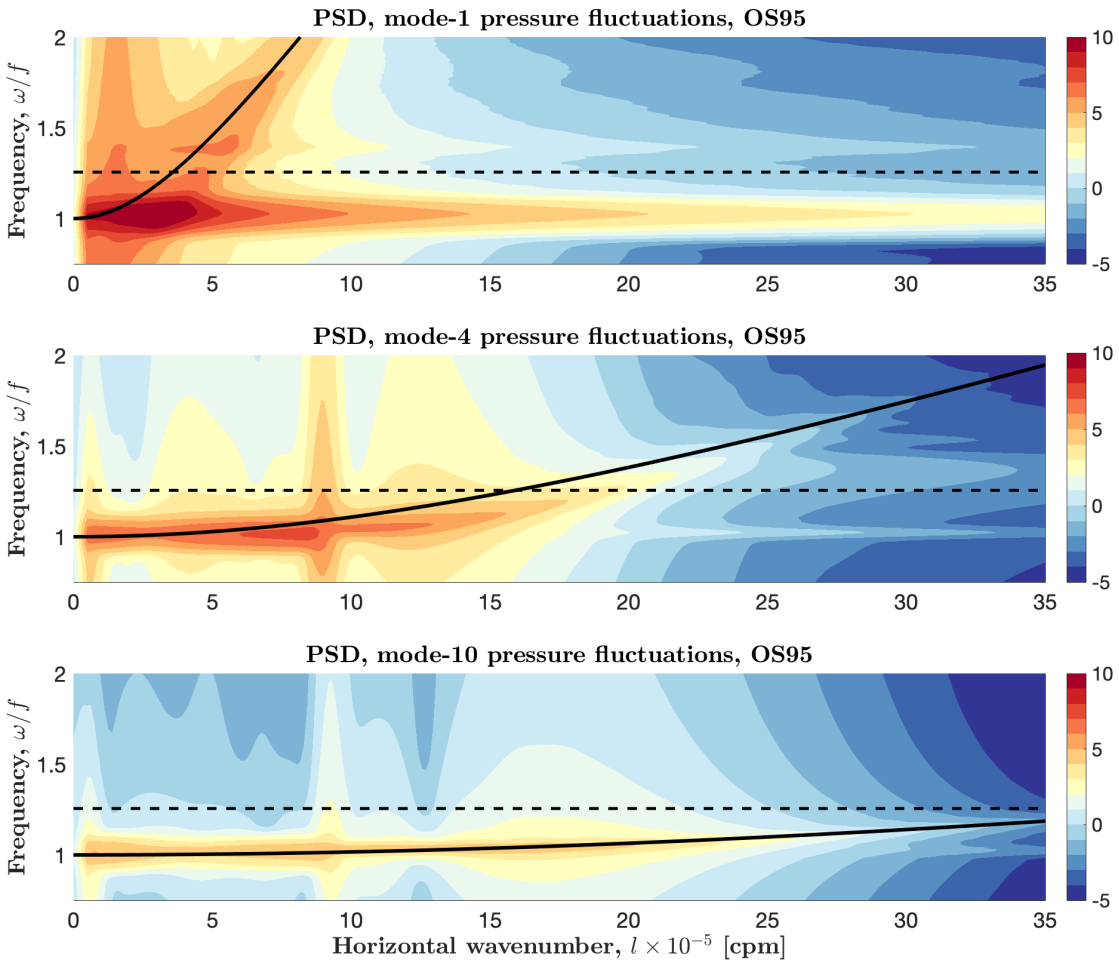

Figure 3.11: Modal pressure spectra and the corresponding dispersion curves are shown for modes 1, 4, and 10 using OS95 parameters. Pressure spectra are calculated from model runs after 100 inertial periods.

increases and phase velocity decreases, consistent with the standard inertia-gravity wave dispersion relation.

The NIW generation occurs over 30 inertial periods before the inertial pumping signal is damped out and generation associated with the impulse storm is over. Mode-1 and mode-4 NIW generation related to individual sources ($\nabla \times \tau$, β, and ζ) can be inferred from the spectra of Figure 3.5. NIW generation is enhanced where the modal dispersion curve passes through regions of elevated power spectral density in frequency/wavenumber space (mode-1 and mode-4 dispersion curves are shown). This provides cutoff wavenumbers for each generation mechanism and sets the horizontal scales of the generated waves. Higher mode dispersion relations result in flatter lines in frequency wavenumber space, and thus allow for the generation of waves with smaller horizontal scales. However, the amplitude of the vertical velocity for each mode is determined by the stress profile [through α in (3.3.2.4)], and tends to decrease rapidly at higher modes, which ultimately limits the generation of waves at small horizontal scales.

Cutoff wavenumbers can be more rigorously quantified by taking the power spectral density of the pressure fluctuations in frequency-wavenumber space and comparing these spectra to the modal dispersion curves. We calculate these spectra for modes 1, 4, and 10 in Figure 3.11, alongside the dispersion curves. Viewing the pressure spectra in tandem with the modal distribution provides a three-dimensional view of the wave-field characteristics. For example, in the case of OS95, the vertical wavenumber spectra is asymptotic to zero beyond mode-10 (Fig 3.9, bottom panel). Looking at the mode-10 pressure spectra shows that the PSD decays rapidly for wavenumbers larger than $\sim 25 \times 10^{-5}$. This defines a lower bound on the lateral scales of NIWs that can be generated from the OS95 forcing case, and we find minimum wavelengths of ~ 25 km. We note that this technique provides more precision with respect to estimating cutoff wavenumbers for specific modes, but comes at the cost of losing the ability to isolate individual forcing mechanisms from one another.

NISKINe Dipole Vortex

Observations from the NISKINe experiment in the Iceland basin revealed a strong, time-persistent pair of counter-rotating eddies that were termed the 'dipole vortex' [Thomas et al., 2020]. This structure featured variability of the Rossby number on the order of 0.1 over distances of $\sim$ 10 km, with total dipole size on the order of $\sim$ 100 km [Asselin et al., 2020]. The resulting dipole feature has a Rossby number Ro $\sim$ 0.3.

Strong storms are common in the Iceland basin. In an investigation of the power input to near inertial motions in the ML, Klenz et al. [2022] discusses observations of one such storm in the Iceland Basin. Using Lagrangian Minimet drifters, the peak wind stress associated with the storm was observed to have $\tau_{max} \sim 0.8$ Pa [Centurioni, 2018, Klenz et al., 2022]. The storm size is not explicitly quantified in the study, but wind maps show size comparable to the storm observed by D'Asaro et al. [1995]. This storm was weaker than OS95, with peak wind stress of 0.8 Pa, but is still a substantial atmospheric forcing event, was shown by Klenz et al. [2022] to generate strong inertial oscillations, and was hypothesized to be an effective NIW generation event.

We construct a numerical study of NISKINe which draws upon the observations discussed by Thomas et al. [2020] and Klenz et al. [2022]. In this case study, we superpose an idealized storm on a simplified dipole vortex consistent with Asselin et al. [2020]. We employ the same impulsive Gaussian storm structure and size as that used in our analysis of OS95, but impose the wind stress observed by Klenz et al. [2022]. For vorticity, we approximate the structure as two Gaussian eddies in tandem, with opposing sign of ζ. The local vorticity is positive in the northern eddy and negative in the southern eddy, with a central latitude of 57.8° N. Note that in the observations, the dipole is oriented with major axis running from northwest to southeast, but for our 1D meridional model, we neglect this zonal rotation. For NISKINe, $c_1 \sim 1.59$, yielding a mode-1 Rossby radius of $\text{Ro}_1 = 12.9$ km.

Model output for mode-1 NIW generation associated with the NISKINe test case is shown in Figure 3.12. Here, the inertial pumping due to ζ is $\sim$ two orders of magnitude stronger than that of $\nabla \times \tau$ and β [Asselin et al., 2020]. The spectral

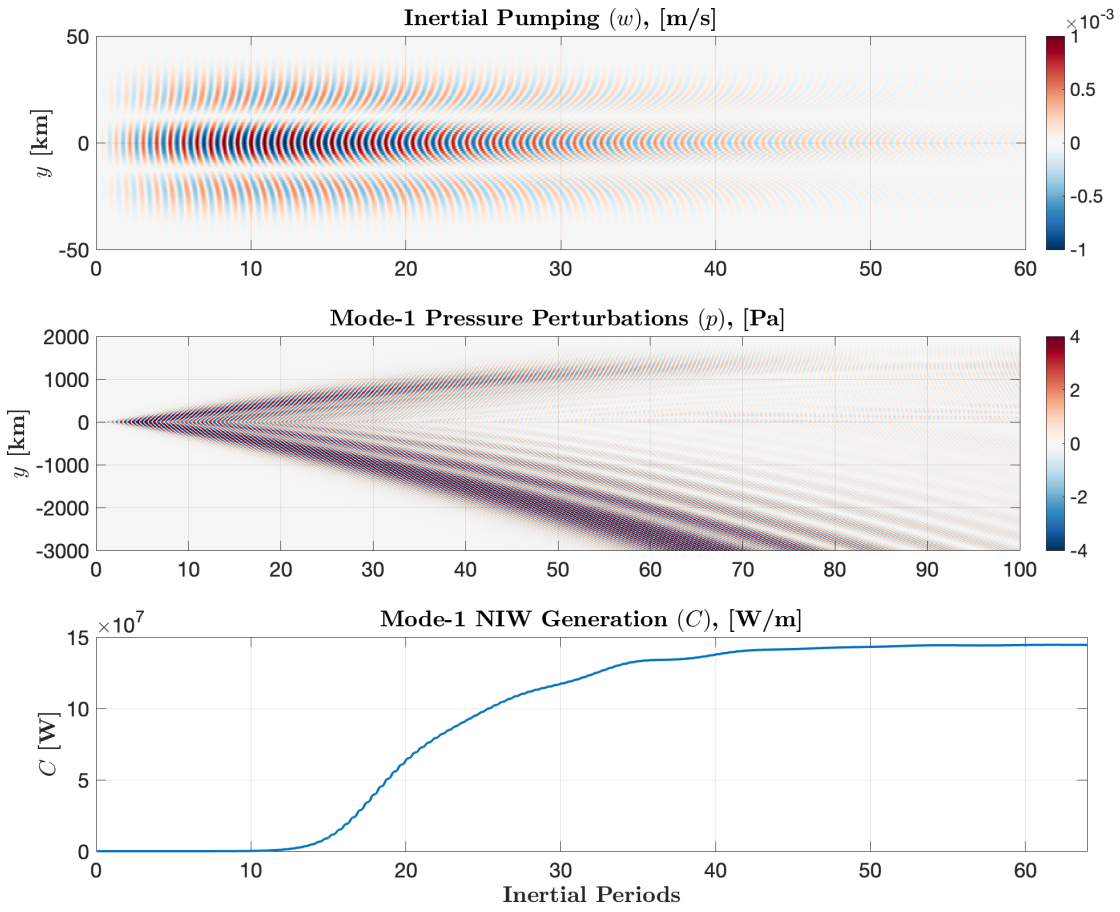

Figure 3.12: Model output for mode-1 NIW generation associated with the NISKINe Dipole Vortex test case is shown. For all cases, time is given as inertial periods on the x-axis. **Top panel:** Inertial pumping (w) is shown as a function of distance [km north/south, y-axis] and time. Peak vertical velocities of 8.6×10^{-4} m/s are calculated after 15 inertial periods, beyond which inertial pumping decays. **Middle panel:** Pressure fluctuations associated with mode-1 NIWs are shown as a function of distance [km north/south, y-axis] and time. Group velocity is extracted as the slope of the cone, and phase velocity is extracted as the slope of individual isobars. **Bottom panel:** Total NIW flux (generation) is calculated for the domain. After $\sim$ 55 inertial periods, generation ceases.

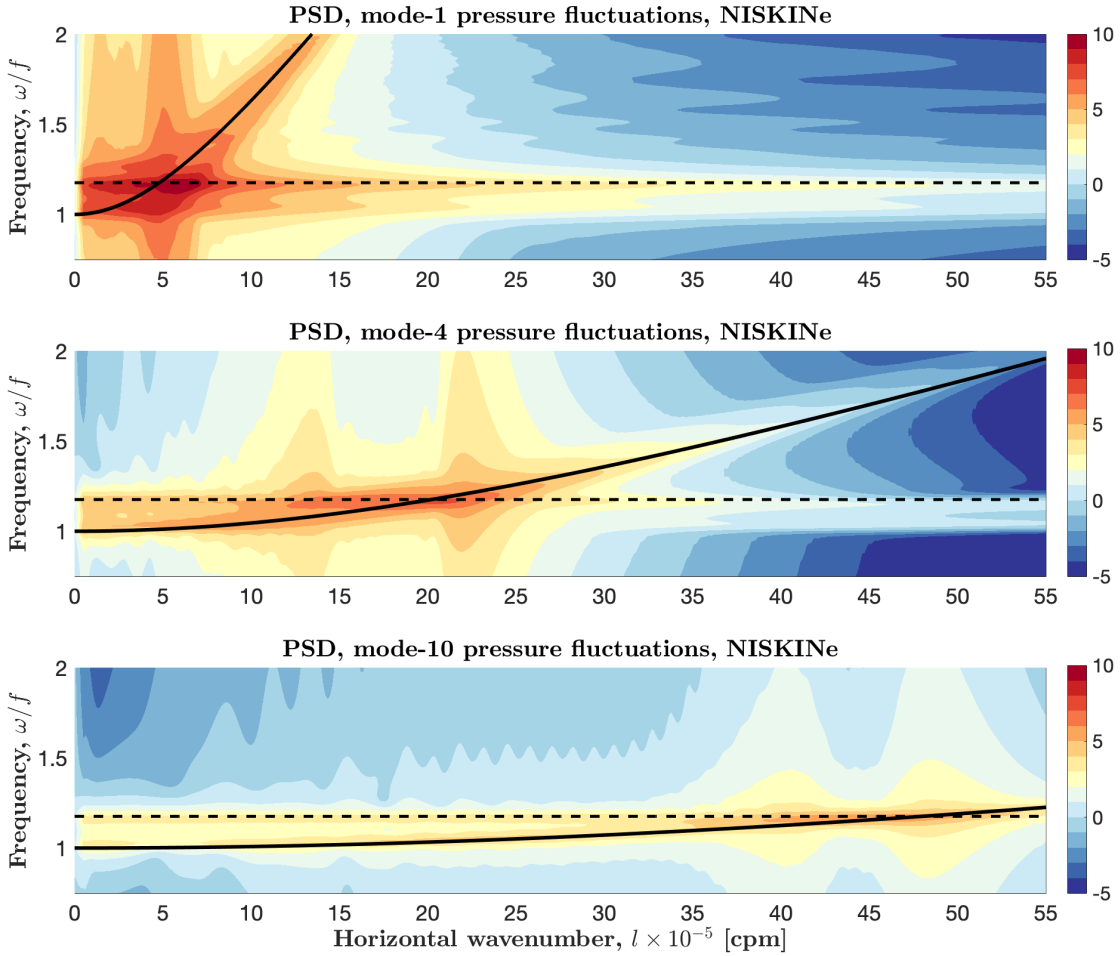

Figure 3.13: Modal pressure spectra and the corresponding dispersion curves are shown for modes 1, 4, and 10 using NISKINe parameters. Pressure spectra are calculated from model runs after 100 inertial periods.

density of mesoscale forcing (Figure 3.6) implies that the contribution to NIW generation associated with ζ for all modes is also roughly two orders of magnitude greater than that of $\nabla \times \tau$ and β. We note that although the magnitudes of inertial pumping we see in the NISKINe case are stronger by an order of magnitude or more, the OS95 case generates nearly twice the energetic volume of mode-1 waves.

NIW generation is dominant in the neighborhood of the dipole vortex, where wave frequencies are strongly modified by the local Rossby number. Packets of waves generated near the core of the cyclonic eddy can travel poleward for great distances due to this shift in inertial frequency. Model output shows poleward propagating waves reaching as far as 1500 km north of the generation site, consistent with Fu [1981]'s turning-latitude theory. This presents a considerable contrast with the Ro=0.02 eddy in OS95, where poleward NIW propagation is negligible.

The individual mode-1 waves that are generated at the dipole, however, have much larger lateral scales than the feature itself. This can be explained by comparing the power spectral densities of $\zeta-$forcing with the mode-1 dispersion curve (Fig. 3.6). The forcing spectral peak lies in the super-inertial band on $l \sim 5 \times 10^{-5}$, which corresponds to length scales on the order of the dipole size. Despite the peak forcing at these scales, the mode-1 dispersion curve increases quickly and leaves the peak forcing regime as wavenumber increases, with little contribution for $l \geq 2 \times 10^{-5}$. This trend is mirrored in the pressure spectra. For contrast, the flatter mode-4 dispersion curve is coincident with the strongest $\zeta-$forcing throughout a broader range of wavenumbers.

The NISKINe case study has a rich modal structure with substantial high-mode activity showing on the vertical wavenumber spectra (Fig. 3.9, bottom panel). While the mode-1 waves which exceed the dipole in lateral scale, we find that the forcing in the NISKINe case preferentially generates waves that decrease in lateral scale as mode increases. In the pressure spectra, this shows as the spectral peak of $l \sim 20 \times 10^{-5}$ for mode-4 and the peak of $l \sim 45 \times 10^{-5}$ for mode-10. This is a very different picture from the OS95 case, where a maximum wavenumber was reached by mode-4, which was unchanged through mode-10 and beyond, where generation ceases.

3.4.5 Sensitivity of generation to storm size and mesoscale vorticity

Mode-1 NIW generation, local dissipation, and wind work are shown for a range of storm sizes in Figure 3.14. The 'default' storm parameters in the figure are again set for consistency with OS95 (see Table 1). Performing analyses on both an f-plane and a β-plane allows us to place quantitative bounds on the threshold storm size beyond which β-refraction must be considered. This is determined by the minimum storm size that causes the generation curves calculated on f- and β-planes to diverge. We find a bounding storm size of approximately 2 Rossby radii in terms of the OS95 parameter space, which is equivalent to an RMS storm width of ~ 40 km.

As storm size increases, the energetic volume of NIW generation monotonically increases. However, as RMS storm width increases beyond ~ 70 km ($3.5\ L_{\mathrm{Ro}}^{\mathrm{OS95}}$), C *decreases* if β is not considered, regardless of Rossby numnber. This implies that the wind stress curl becomes less effective at generating NIWs for large storms. For the OS95 case, we find that β's contribution to NIW generation is nearly 80%, with $\nabla \times \tau$ contributing only $\sim 15\%$ of the total NIW generation. This is qualitatively consistent with D'Asaro et al. [1995], but the decomposition introduced in the work presented allows us to extend D'Asaro et al. [1995]'s results by quantifying the individual productivity of the three NIW generation mechanisms considered.

As with the relationship of β to storm size, there exists a threshold storm size beyond which ζ plays an important role in NIW generation. Recall that we are studying the impact of a nominal mesoscale eddy with diameter of 100 km and Ro = 0.1 [Rhines, 2001]. Our numerical experiment suggests that once the size of the storm exceeds the size of the eddy, the impact of ζ becomes non-negligible. Unlike β, here we find that ζ does not continue to increase generation indefinitely with increasing storm size. In the case presented, for $L_{\mathrm{storm}} > 6\ L_{\mathrm{Ro}}^{\mathrm{OS95}}$, increases in C due to ζ attenuate as storm size increases. This appears in the top panel of Figure 3.14 as the region where the two dashed lines parallel each other, showing that further increases in C at this point are attributed to β rather than ζ.

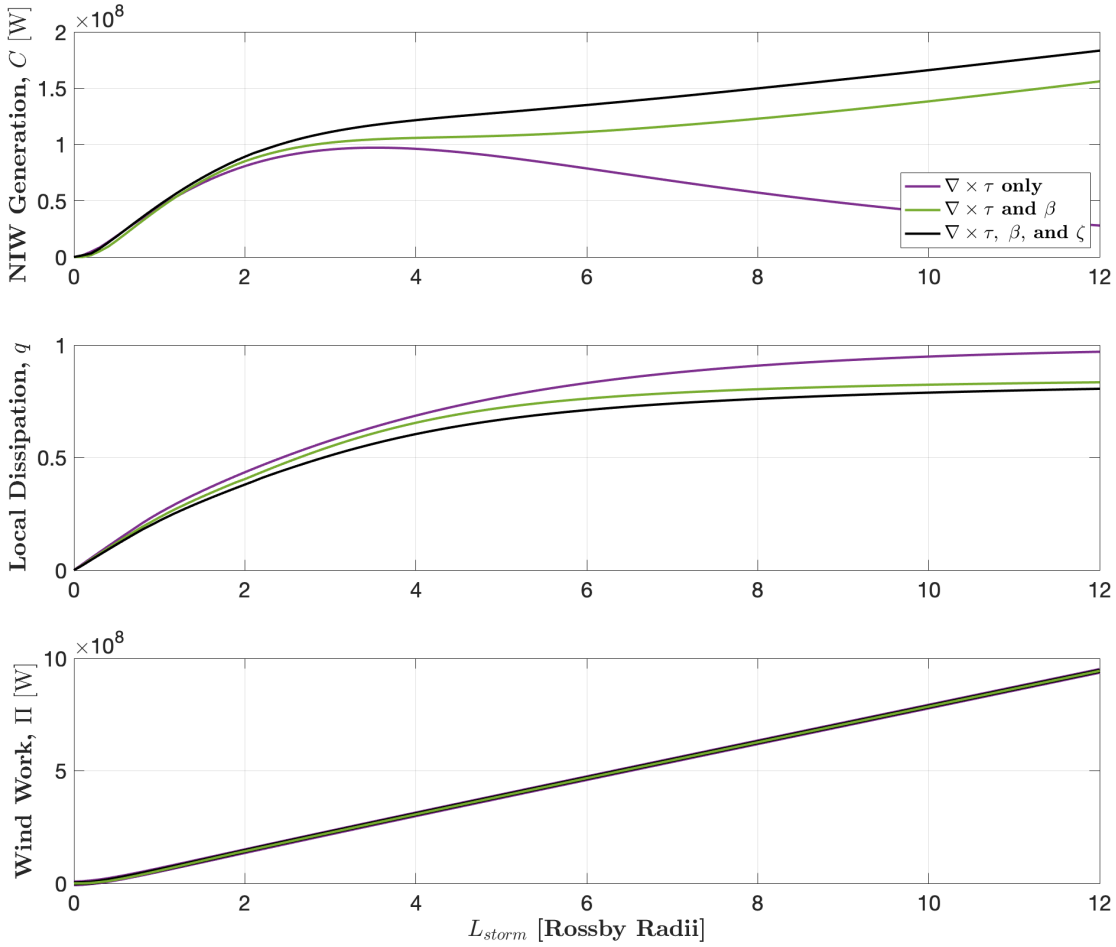

Figure 3.14: Near inertial wave generation (C, top panel), the associated local dissipation (q, middle panel), and wind work (Π, bottom panel) are calculated for variable storm size. The base parameter space corresponds to OS95 with $\zeta = 0$. When mesoscale eddies are considered, the vorticity structure follows a nominal mesoscale eddy with 100 km diameter and Ro = 0.1 [Rhines, 2001].

3.5 Discussion

3.5.1 NIWs vs Tides

We have developed a new conceptual model of NIW generation. In this formulation, the NIW generation problem is analogous to internal tide generation, but the vertical velocities are set by forced dynamics in the oceanic surface boundary layer (OSBL) rather than flow over topography [Llewellyn Smith and Young, 2002]. For a typical parameter space, these fundamentally different forcing mechanisms (OSBL and topography) produce comparable vertical velocities (e.g. Sec. 3.3.3.6). Because the vertical velocities provide the forcing in the internal wave generation equations, which are analogous, a naive assertion would be that the resulting energy contained in these respective internal wave fields should be similar in magnitude.

The relative importance of internal tides and near inertial internal waves is an open area of research with a long history [Baines, 1986, Alford et al., 2007]. Internal tidal conversion is well-observed and estimated to contribute 1 $\pm O(0.1)$ TW of power to the global ocean [Baines, 1982, Egbert and Ray, 2000, 2001]. Because tidal forcing is continuous, measurements of internal tides are ubiquitous, driving down uncertainties in their energetic contributions [Zhao et al., 2016]. On the contrary, NIWs are forced intermittently by wind events causing observations of NIWs to be more sparse than those of internal tides [Alford et al., 2016]. Though the importance of NIWs is incontrovertible, inconsistency of observation, analysis techniques, and variable resolution of wind measurement/reanalysis all contribute to the large uncertainties associated with the impact of NIWs on the global ocean's energy budget. The analogy presented here allows one to directly compare the forcing of an NIW generation event with that of internal tide generation, and may prove useful in constraining the relative importance of these two phenomena. The mathematical equivalence of the two problems also opens up a suite of tools for use in the study of NIW generation, as we have used the conversion formula from Llewellyn Smith and Young [2002] in our analysis.

3.5.2 The limits on the lateral scales of NIW generation:

We have introduced a method for estimating the lateral scales of NIWs generated at each mode, summarized as follows. The forced/wave decomposition allows us to isolate the inertial pumping that results from each source of ML forcing under consideration ($\nabla \times \tau$, β, and ζ). Taking the power spectral density of the forcing reveals where in frequency-wavenumber space NIWs can be generated. One can then compare the dispersion curve for a particular mode to estimate the wavenumber of generated waves, and at which frequencies these will occur. Because the forcing is decomposed by generation mechanism, this reveals the relative importance of each mechanism, for each generated wave (e.g. by mode, frequency, wavenumber etc).

Taking the power spectral densities of the pressure fluctuations provides a rigorous bound on the lateral scale of NIWs that are generated at each mode, but this technique has the drawback that the pressure spectra cannot be obtained *a priori* as in the case of the forcing spectra. That is, forward time-stepping over some domain must occur in order to obtain the pressure dataset upon which spectral analysis is performed.

3.5.3 Damping

Results from the parameter sweeps using the eKG model emphasize the care that must be taken in tuning the damping in a mixed layer model. We have shown that damping has little impact on wind work, while NIW generation (C) is strongly effected by damping. One must proceed cautiously when using an inviscid model. The results of our study suggest that damping scales of $r^{-1} = 1$ month may impact NIW generation by $\sim$ 20-40 % for small and large storms, respectively, compared to inviscid results. Compared to standing literature estimates, which assert damping scales are on the order of $r^{-1} =$ 3-7 days, inviscid models may overestimate NIW generation by 50 % or more. These results generally support the notion that tuning the damping parameterizations in numerical models is of first-order importance to estimating NIW generation.

Ultimately, the stress profile is a key part of this problem to consider. Recall that throughout the analysis presented, we have used the damped slab model of

Pollard and Millard [1970]. This ML model is used for simplicity, so that the modal forcing (denoted α_n here) can be approximated as a constant. In general, the modal forcing is an integral related to the form of the stress profile. Stokes et al. [2023] develop a generalized slab model for which the modal forcing can be calculated using an observed (or assumed) stress profile.

Stokes et al. [2023] show that the stress profile contributes strongly to the local dissipation which we have absorbed into our catch-all linear damping parameter r. Additionally, they show that changing the stress profile shifts the vertical wavenumber spectra which ultimately effects whether NIWs will dissipate locally or propagate away from the generation site, which has important implications to ocean mixing. In the present manuscript, part of the large impact that varying damping has on NIW generation is directly related to these factors that are accounted for by the damping parameter, such as the shape of the stress profile. We emphasize the need to refine and improve models and measurements of the stress and dissipation profiles ($\boldsymbol{\tau}(z)$ and $\epsilon(z)$) in the oceanic surface boundary layer.

3.5.4 High-frequency limit of the near-inertial band

It is not clear where the line should be drawn in frequency-wavenumber space define the high-frequency limit of the near-inertial band. Alford et al. [2016] suggests that the near-inertial band cuts off where $\omega/f \leq 1.2$, based on the abundance of observations where this is the case. However, our pressure spectra suggest that the wind impulse generates a continuum of internal waves. The frequency range of this continuum is mode dependent, with low-mode waves reaching higher values of ω/f. In both the OS95 and NISKINe cases, we calculate mode-1 spectra with frequencies extending through and beyond $\omega/f = 2$. Such large frequencies lie well outside of the traditional near-inertial band, but because these waves arise from the ML's inertial response to wind forcing, it seems fair to refer to them as near-inertial waves. An open area of research is further investigating where and when the bandwidth of inertially-generated waves may be directly observable vs. where and when it is dominated by GM or submesoscale variability.

3.6 Conclusions

(1) The extended Klein-Gordon (eKG) model developed in this manuscript provides a new perspective on the NIW generation process. Specifically, we show that NIW generation can be formulated so that it is exactly analogous to internal tide generation. This analogy allows us to quantitatively compare forcing and to use previously developed tools, such as the conversion formula from Llewellyn Smith and Young [2002] (e.g. 3.3.3.11). One could even use the convolutions developed by Nycander [2005], but these require greater numerical computations than simply solving the eKG equations.

(2) The separation of the forcing function and wave response reveals that $\beta-$ and ζ refraction can produce high-wavenumber variability that does *not* generate waves. This contradicts the common assumption that NIWs are generated at scales which identically mirror their forcing. For example, D'Asaro et al. [1995] quantified the growing meridional wavenumber of mixed layer currents as a result of $\beta-$refraction, but this does not guarantee that inertia-gravity waves are radiated at every observed wavenumber. For the OS95 case our spectral analysis suggest that once the wavelength reaches about 25 km, mode-1 waves are no longer generated. More generally, the spectral approach we have introduced constrains the scales of NIW generation for each mode. Because the vertical energy propagation associated with internal waves is a function of the total wave generation and the lateral scale of these waves, this technique may prove to be a useful tool in reducing uncertainties related to how NIWs impact the global ocean's energy budget.

(3) Even modest damping can have a major impact on near-inertial wave generation and local dissipation. Reducing the number of phenomena that are absorbed into the linear damping parameter will relax the impact of damping variability on generation and dissipation.

3.6.1 Acknowledgements

I. A. Stokes was supported by ONR Grant N00014-22-1-2730. A. J. Lucas was supported by ONR Grants N00014-22-1-2730, N00014-22-1-2575, and N00014-21-

C-1027. S. M. Kelly was supported by ONR Grant N00014-181-2800 and NSF Grant OCE-1635560. We thank Brewer et al. [2003] for providing the colormaps used in this work.

Chapter 3, in full, is a reprint of the material as it appears in Near-inertial wave generation in a linear, damped mixed layer model, Journal of Physical Oceanography. Ian A. Stokes, Samuel M. Kelly, Andrew J. Lucas; *In Preparation* 2023. The dissertation author was the primary investigator and author of this paper.

3.6.2 Data Availability Statement

All shipboard and drifter data collected as part of the U.S. ONR NISKINe DRI are still in the process of being organized and archived. All data will be fully released to the public when the program formally concludes. NISKINe data presented in this study are available from the corresponding author upon reasonable request.

Bibliography

Peter N Adams, Douglas L Inman, and Nicholas E Graham. Southern california deep-water wave climate: characterization and application to coastal processes. *Journal of Coastal Research*, 24(4 (244)):1022–1035, 2008.

M. H. Alford. Internal swell generation: The spatial distribution of energy flux from the wind to mixed layer near-inertial motions. *J. Phys. Oceanogr.*, 31: 2359–2368, 2001.

M. H. Alford and M. Whitmont. Seasonal and spatial variability of near-inertial kinetic energy from historical moored velocity records. *J. Phys. Oceanogr.*, 37: 2022–2037, 2007.

M. H. Alford, J. A. MacKinnon, Z. Zhao, R. Pinkel, J. Klymak, and T. Peacock. Internal waves across the Pacific. *Geophys. Res. Lett.*, 34:L24601, doi:10.1029/2007GL031566, 2007.

M. H. Alford, J. A. MacKinnon, H. L. Simmons, and J. D. Nash. Near-inertial internal gravity waves in the ocean. *Ann. Rev. Mar. Sci.*, 12:389–433, 2016.

Matthew H Alford. Revisiting near-inertial wind work: Slab models, relative stress, and mixed layer deepening. *Journal of Physical Oceanography*, 50(11):3141–3156, 2020a.

Matthew H Alford. Global calculations of local and remote near-inertial-wave dissipation. *Journal of Physical Oceanography*, 50(11):3157–3164, 2020b.

Matthew H Alford, Meghan F Cronin, and Jody M Klymak. Annual cycle and depth penetration of wind-generated near-inertial internal waves at ocean station

papa in the northeast pacific. *Journal of Physical Oceanography*, 42(6):889–909, 2012.

Wayne M Angevine, JE Hare, CW Fairall, Daniel E Wolfe, RJ Hill, WA Brewer, and Allen B White. Structure and formation of the highly stable marine boundary layer over the gulf of maine. *Journal of Geophysical Research: Atmospheres*, 111(D23), 2006.

Olivier Asselin, Leif N Thomas, William R Young, and Luc Rainville. Refraction and straining of near-inertial waves by barotropic eddies. *Journal of Physical Oceanography*, 50(12):3439–3454, 2020.

P. G. Baines. On internal tide generation models. *Deep-Sea Res.*, 29:307–338, 1982.

P. G. Baines. Internal tides, internal waves, and near-inertial motions. In C. N. K. Mooers, editor, *Baroclinic Processes on Continental Shelves*, volume 3, pages 19–31. American Geophys. Union, Washingtn D. C., 1986.

Lisa T Ballance. Flight energetics of free-ranging red-footed boobies (sula sula). *Physiological Zoology*, 68(5):887–914, 1995.

Michael L Banner and W Kendall Melville. On the separation of air flow over water waves. *Journal of fluid mechanics*, 77(4):825–842, 1976.

Eric Barthélemy. Nonlinear shallow water theories for coastal waves. *Surveys in Geophysics*, 25(3-4):315–337, 2004.

Changwei Bian, Zhiyu Liu, Yongxiang Huang, Liang Zhao, and Wensheng Jiang. On estimating turbulent reynolds stress in wavy aquatic environment. *Journal of Geophysical Research: Oceans*, 123(4):3060–3071, 2018.

Vincent Bonnin, Emmanuel Bénard, J-M Moschetta, and CA Toomer. Energy-harvesting mechanisms for uav flight by dynamic soaring. *International Journal of Micro Air Vehicles*, 7(3):213–229, 2015.

Willem Bouten, Edwin W Baaij, Judy Shamoun-Baranes, and Kees CJ Camphuysen. A flexible gps tracking system for studying bird behaviour at multiple scales. *Journal of Ornithology*, 154(2):571–580, 2013.

John P Boyd. *Chebyshev and Fourier spectral methods*. Courier Corporation, 2001.

Keith E Brainerd and Michael C Gregg. Surface mixed and mixing layer depths. *Deep Sea Research Part I: Oceanographic Research Papers*, 42(9):1521–1543, 1995.

Cynthia A Brewer, Geoffrey W Hatchard, and Mark A Harrower. Colorbrewer in print: a catalog of color schemes for maps. *Cartography and geographic information science*, 30(1):5–32, 2003.

Noel G Brizuela, TM Shaun Johnston, Matthew H Alford, Olivier Asselin, Daniel L Rudnick, Jim Moum, Elizabeth J Thompson, Shuguang Wang, and Chia-Ying Lee. A vorticity-divergence view of internal wave generation by tropical cyclones: insights from super typhoon mangkhut. *Authorea Preprints*, 2022.

Marc P Buckley and Fabrice Veron. Structure of the airflow above surface waves. *Journal of Physical Oceanography*, 46(5):1377–1397, 2016.

Marc P Buckley and Fabrice Veron. The turbulent airflow over wind generated surface waves. *European Journal of Mechanics-B/Fluids*, 73:132–143, 2019.

M. C. Buijsman, G. R. Stephenson, J. K. Ansong, B. K. Arbic, J. A. M. Green, J. G. Richman, J. F. Shriver, C. Vic, A. J. Wallcraft, and Z. Zhao. On the interplay between horizontal resolution and wave drag and their effect on tidal baroclinic mode waves in realistic global ocean simulations. *Ocean Modelling*, 152:101656, 2020.

Eugeny Buldakov, Dimitris Stagonas, and Richard Simons. Extreme wave groups in a wave flume: Controlled generation and breaking onset. *Coastal Engineering*, 128:75–83, 2017.

Luca R Centurioni. Drifter technology and impacts for sea surface temperature, sea-level pressure, and ocean circulation studies. *Observing the Oceans in Real Time*, pages 37–57, 2018.

E. P. Chassignet, H. E. Hurlburt, O. M. Smedstad, G. R. Halliwell, P. J. Hogan, A. J. Wallcraft, R. Baraille, and R. Bleck. The HYCOM (HYbrid Coordinate Ocean Model) data assimilative system. *J. Mar. Systems*, 65:60–83, 2007.

Cédric P Chavanne, Eric Firing, and François Ascani. Inertial oscillations in geostrophic flow: Is the inertial frequency shifted by $\zeta/2$ or by ζ? *Journal of Physical Oceanography*, 42(5):884–888, 2012.

Clarence D Cone. Thermal soaring of birds. *American Scientist*, 50(1):180–209, 1962.

E. D'Asaro. The energy flux from the wind to near-inertial motions in the surface mixed layer. *J. Phys. Oceanogr.*, 15:1043–1059, 1985.

E. D'Asaro. The decay of wind-forced mixed layer inertial oscillations due to the β effect. *J. Geophys. Res.*, 94:2045–2056, 1989.

E. A. D'Asaro, C. C. Eriksen, M. D. Levine, P. Niler, C. A. Paulson, and P. Van Meurs. Upper-ocean inertial currents forced by a strong storm. Part I: Data and comparisons with linear theory. *J. Phys. Oceanogr.*, 25:2909–2936, 1995.

Eric A D'asaro. Upper-ocean inertial currents forced by a strong storm. part ii: Modeling. *Journal of physical oceanography*, 25(11):2937–2952, 1995.

RE Davis, R DeSzoeke, D Halpern, and P Niiler. Variability in the upper ocean during mile. part i: The heat and momentum balances. *Deep Sea Research Part A. Oceanographic Research Papers*, 28(12):1427–1451, 1981.

Luc Deike, Nick Pizzo, and W Kendall Melville. Lagrangian transport by breaking surface waves. *Journal of Fluid Mechanics*, 829:364, 2017.

Markus Deittert, Arthur Richards, Chris A Toomer, and Anthony Pipe. Engineless unmanned aerial vehicle propulsion by dynamic soaring. *Journal of guidance, control, and dynamics*, 32(5):1446–1457, 2009.

Kathleen Dohan and Russ E Davis. Mixing in the transition layer during two storm events. *Journal of Physical Oceanography*, 41(1):42–66, 2011.

OA Druzhinin, Yu I Troitskaya, and SS Zilitinkevich. Direct numerical simulation of a turbulent wind over a wavy water surface. *Journal of Geophysical Research: Oceans*, 117(C11), 2012.

M. Dunphy and K. G. Lamb. Focusing and vertical mode scattering of the first mode internal tide by mesoscale eddy interaction. *J. Geophys. Res.*, 119:523–536, 2014.

M. Dunphy, A. L. Ponte, P. Klein, and S. Le Gentil. Low-mode internal tide propagation in a turbulent eddy field. *J. Phys. Oceanogr.*, 47:649–659, 2017.

James B Edson, Venkata Jampana, Robert A Weller, Sebastien P Bigorre, Albert J Plueddemann, Christopher W Fairall, Scott D Miller, Larry Mahrt, Dean Vickers, and Hans Hersbach. On the exchange of momentum over the open ocean. *Journal of Physical Oceanography*, 43(8):1589–1610, 2013.

G. D. Egbert and R. D. Ray. Significant dissipation of tidal energy in the deep ocean inferred from satellite altimeter data. *Nature*, 405:775–778, doi:10.1038/35015531, 2000.

G. D. Egbert and R. D. Ray. Estimates of M_2 tidal energy dissipation from TOPEX/POSEIDON altimeter data. *J. Geophys. Res.*, 106:22475–22502, 2001.

Kyle H Elliott, Maryline Le Vaillant, Akiko Kato, John R Speakman, and Yan Ropert-Coudert. Accelerometry predicts daily energy expenditure in a bird with high activity levels. *Biology letters*, 9(1):20120919, 2013.

Robert Edmund Froude, William Froude, and William Thomson. On the soaring of birds: being a communication from mr re froude in continuation of the extract

from a letter by the late mr william feoude to sir william thomson, published in these "proceedings," march 19, 1888. *Proceedings of the Royal Society of Edinburgh*, 18:65–72, 1892.

Lee-Lueng Fu. Observations and models of inertial waves in the deep ocean. *Reviews of Geophysics*, 19(1):141–170, 1981.

Takashi Fujiki, Koji Kawaguchi, Fumikazu Suehiro, and Noriaki Hashimoto. Highly resolved directional properties of wind waves and swell with various scales. *Coastal Engineering Proceedings*, (36):36–36, 2018.

Naoki Furuichi, Toshiyuki Hibiya, and Yoshihiro Niwa. Model-predicted distribution of wind-induced internal wave energy in the world's oceans. *Journal of Geophysical Research: Oceans*, 113(C9), 2008.

Ann E Gargett. Ocean turbulence. *Annual Review of Fluid Mechanics*, 21(1): 419–451, 1989.

A. E. Gill. *Atmosphere-ocean dynamics*. Academic Press, 1982.

A. E. Gill. On the behavior of internal waves in the wakes of storms. *J. Phys. Oceangr.*, 14:1129–1151, 1984.

A. E. Gill and A. J. Clarke. Wind-induced upwelling, coastal currents and sea-level changes. *Deep-Sea Res.*, 21:325–345, 1974.

Gustavo J Goni, Robert E Todd, Steven R Jayne, George Halliwell, Scott Glenn, Jili Dong, Ruth Curry, Ricardo Domingues, Francis Bringas, Luca Centurioni, et al. Autonomous and lagrangian ocean observations for atlantic tropical cyclone studies and forecasts. *Oceanography*, 30(2):92–103, 2017.

AA Grachev and CW Fairall. Upward momentum transfer in the marine boundary layer. *Journal of physical oceanography*, 31(7):1698–1711, 2001.

Alan LM Grant and Stephen E Belcher. Wind-driven mixing below the oceanic mixed layer. *Journal of physical oceanography*, 41(8):1556–1575, 2011.

Laurent Grare, Luc Lenain, and W Kendall Melville. Vertical profiles of the wave-induced airflow above ocean surface waves. *Journal of Physical Oceanography*, 48(12):2901–2922, 2018.

Michael C Gregg. The study of mixing in the ocean: A brief history. *Oceanography*, 4(1):39–45, 1991.

Rahul Gupta, Rohit Gupta, and Dinesh Verma. Application of convolution method to the impulsive response of a lightly damped harmonic oscillator. *International Journal of Scientific Research in Physics and Applied Sciences*, 7(3):173–175, 2019.

F Reed Hainsworth. Induced drag savings from ground effect and formation flight in brown pelicans. *Journal of Experimental Biology*, 135(1):431–444, 1988.

Kimio Hanawa and Lynne D Talley. Mode waters. In *International Geophysics*, volume 77, pages 373–386. Elsevier, 2001.

A Hedenstrom and FELIX Liechti. Field estimates of body drag coefficient on the basis of dives in passerine birds. *Journal of Experimental Biology*, 204(6): 1167–1175, 2001.

Robert W Helber, A Birol Kara, James G Richman, Michael R Carnes, Charlie N Barron, Harley E Hurlburt, and Timothy Boyer. Temperature versus salinity gradients below the ocean mixed layer. *Journal of Geophysical Research: Oceans*, 117(C5), 2012.

Ulf Högström, A Smedman, Erik Sahleé, WM Drennan, KK Kahma, H Pettersson, and F Zhang. The atmospheric boundary layer during swell: A field study and interpretation of the turbulent kinetic energy budget for high wave ages. *Journal of the atmospheric sciences*, 66(9):2764–2779, 2009.

James Holte and Lynne Talley. A new algorithm for finding mixed layer depths with applications to argo data and subantarctic mode water formation. *Journal of Atmospheric and Oceanic Technology*, 26(9):1920–1939, 2009.

James Holte, Lynne D Talley, John Gilson, and Dean Roemmich. An argo mixed layer climatology and database. *Geophysical Research Letters*, 44(11):5618–5626, 2017.

Chuan Jiang Huang and Fangli Qiao. Simultaneous observations of turbulent reynolds stress in the ocean surface boundary layer and wind stress over the sea surface. *Journal of Geophysical Research: Oceans*, 126(2):e2020JC016839, 2021.

D Hummel. The aerodynamic characteristics of slotted wing-tips in soaring birds. *Acta Congressus Internationalis Ornithologici*, 1:391–396, 1980.

Nyla T Husain, Tetsu Hara, Marc P Buckley, Kianoosh Yousefi, Fabrice Veron, and Peter P Sullivan. Boundary layer turbulence over surface waves in a strongly forced condition: Les and observation. *Journal of Physical Oceanography*, 49(8): 1997–2015, 2019.

P Idrac. Experimental study of the "soaring" of albatrosses. *Nature*, 115(2893): 532–532, 1925.

W Jameson. The wandering albatross. *HartDavis, London*, 1958.

HAN Jiakun, HUI Zhe, TIAN Fangbao, and CHEN Gang. Review on bio-inspired flight systems and bionic aerodynamics. *Chinese Journal of Aeronautics*, 2020.

L Christoffer Johansson, Lasse Jakobsen, and Anders Hedenström. Flight in ground effect dramatically reduces aerodynamic costs in bats. *Current Biology*, 28(21): 3502–3507, 2018.

TM Shaun Johnston and Daniel L Rudnick. Observations of the transition layer. *Journal of physical oceanography*, 39(3):780–797, 2009.

Alexis K Kaminski, Eric A D'Asaro, Andrey Y Shcherbina, and Ramsey R Harcourt. High-resolution observations of the north pacific transition layer from a lagrangian float. *Journal of Physical Oceanography*, 51(10):3163–3181, 2021.

S. M. Kelly. The vertical mode decomposition of surface and internal tides in the presence of a free surface and arbitrary topography. *J. Phys. Oceanogr.*, 46: 3777–3788, 2016.

S. M. Kelly. Coastally generated near-inertial waves. *J. Phys. Oceanogr.*, 49: 2979–2995, 2019.

S. M. Kelly, P. F. J. Lermusiaux, T. F. Duda, and P. J. Haley Jr. A coupled-mode shallow-water model for tidal analysis: Internal tide reflection and refraction by the Gulf Stream. *J. Phys. Oceanogr.*, 46:3661–3679, 2016.

Samuel M Kelly, Amy F Waterhouse, and Anna C Savage. Global dynamics of the stationary m2 mode-1 internal tide. *Geophysical Research Letters*, 48(11), 2021.

Thilo Klenz, Harper L Simmons, Luca Centurioni, Jonathan M Lilly, Jeffrey J Early, and Verena Hormann. Estimates of near-inertial wind power input using novel in situ wind measurements from minimet surface drifters in the iceland basin. *Journal of Physical Oceanography*, 52(10):2417–2430, 2022.

P. K. Kundu, S.-Y. Chao, and J. P. McCreary. Transient coastal currents and inertio-gravity waves. *Deep-Sea Res.*, 30:1059–1082, 1983.

E. Kunze. Near-inertial wave propagation in geostrophic shear. *J. Phys. Oceanogr.*, 15:544–565, 1985.

EV Laitone. Comment on'drag reduction factor due to ground effect'. *Journal of Aircraft*, 27(1):96–96, 1990.

M. Lakshmanan. Solitons, tsunamis and oceanographical applications of. In Robert A. Meyers, editor, *Mathematics of Complexity and Dynamical Systems*, pages 1603–1617. Springer New York, New York, NY, 2011. ISBN 978-1-4614-1806-1. doi: 10.1007/978-1-4614-1806-1_103.

William G Large, James C McWilliams, and Scott C Doney. Oceanic vertical mixing: A review and a model with a nonlocal boundary layer parameterization. *Reviews of geophysics*, 32(4):363–403, 1994.

Eva Le Merle, Danièle Hauser, and Céline Tison. Directional wave spectra at the regional scale with the kuros airborne radar: comparisons with models. *Ocean Dynamics*, 69(6):679–699, 2019.

Vianey Leos-Barajas, Theoni Photopoulou, Roland Langrock, Toby A Patterson, Yuuki Y Watanabe, Megan Murgatroyd, and Yannis P Papastamatiou. Analysis of animal accelerometer data using hidden markov models. *Methods in Ecology and Evolution*, 8(2):161–173, 2017.

Jonathan M. Lilly. jLab: A data analysis package for Matlab, v. 1.7.1. http://www.jmlilly.net/software, 2021.

S. G. Llewellyn Smith and W. R. Young. Conversion of the barotropic tide. *J. Phys. Oceanogr.*, 32:1554–1566, 2002.

R. A. Locarnini, O. K. Baranova, A. V. Mishonov, T. P. Boyer, J. R. Reagan, D. Dukhovskoy, D. Seidov, H. E. Garcia, C. Bouchard, S. Cross, C. R. Paver, and Z. Wang. *World Ocean Atlas 2023, volume 1: Temperature*. U.S. Government Printing Office, NOAA Atlas NESDIS edition, 2023.

Chiang C Mei. *The applied dynamics of ocean surface waves*, volume 1. World scientific, 1989.

C. Millot and M. Crépon. Inertial oscillations on the continental shelf of the Gulf of Lions–observations and theory. *J. Phys. Oceanogr.*, 11:639–657, 1981.

J. Moehlis and S. G. Llewellyn Smith. Radiation of mixed layer near-inertial oscillations into the ocean interior. *J. Phys. Oceanogr.*, 31:1550–1560, 2001.

F Montiel, VA Squire, M Doble, J Thomson, and P Wadhams. Attenuation and directional spreading of ocean waves during a storm event in the autumn beaufort sea marginal ice zone. *Journal of Geophysical Research: Oceans*, 123(8):5912–5932, 2018.

Max M Munk. The minimum induced drag of aerofoils: National advisory committee for aeronautics. Technical report, Report, 1923.

Pearn P Niiler. Deepening of the wind-mixed layer. *J. mar. Res*, 33(3):405–421, 1975.

J. Nycander. Generation of internal waves in the deep ocean by tides. *J. Geophys. Res.*, 110:C10028, doi:10.1029/2004JC002487, 2005.

Robin D Paulos, Marie Trone, and Stan A Kuczaj II. Play in wild and captive cetaceans. *International Journal of Comparative Psychology*, 23(4), 2010.

J. Pedlosky. *Waves in the Ocean and Atmosphere*. Springer, 1 edition, 2003.

CJ Pennycuick. The soaring flight of vultures. *Scientific American*, December, 1973. ISSN 0036-8733.

Colin J Pennycuick. Thermal soaring compared in three dissimilar tropical bird species, fregata magnificens, pelecanus occidentals and coragyps atratus. *Journal of Experimental Biology*, 102(1):307–325, 1983.

Colin J Pennycuick. *Bird flight performance*. Oxford University Press, 1989.

Colin J Pennycuick. *Modelling the flying bird*. Elsevier, 2008.

Neal Robert Pettigrew. *The dynamics and kinematics of the coastal boundary layer off Long Island*. PhD thesis, Massachusetts Institute of Technology, 1981.

A. J. Plueddemann and J. T. Farrar. Observations and models of the energy flux from the wind to mixed-layer inertial currents. *Deep-Sea Res.*, 53:5–30, 2006.

R. T. Pollard and R. C. Millard. Comparison between observed and simulated wind-generated inertial oscillations. *Deep-Sea Res.*, 17:813–821, 1970.

RT Pollard. Properties of near-surface inertial oscillations. *Journal of Physical Oceanography*, 10(3):385–398, 1980.

Friederike Pollmann, Jonas Nycander, Carsten Eden, and Dirk Olbers. Resolving the horizontal direction of internal tide generation. *Journal of Fluid Mechanics*, 864:381–407, 2019.

J. F. Price. Internal wave wake of a moving storm. Part I: Scales, energy budget, and observations. *J. Phys. Oceanogr.*, 13:949–965, 1983.

J. F. Price, R. A. Weller, and R. Pinkel. Diurnal cycling: Observations and models of the upper ocean response to diurnal heating, cooling, and wind mixing. *J. Geophys. Res.*, 91:8411–8427, 1986.

Lord Rayleigh. The soaring of birds. *Nature*, 27(701):534–535, 1883.

Jeremy MV Rayner. On the aerodynamics of animal flight in ground effect. *Philosophical Transactions of the Royal Society of London. Series B: Biological Sciences*, 334(1269):119–128, 1991.

J. R. Reagan, D. Dukhovskoy, D. Seidov, T. P. Boyer, R. A. Locarnini, O. K. Baranova, A. V. Mishonov, H. E. Garcia, C. Bouchard, S. Cross, C. R. Paver, and Z. Wang. *World Ocean Atlas 2023, volume 2: Salinity.* U.S. Government Printing Office, NOAA Atlas NESDIS edition, 2023.

GM Reznik. Dynamics of localized vortices on the beta plane. *Izvestiya, Atmospheric and Oceanic Physics*, 46:784–797, 2010.

PB Rhines. Mesoscale eddies in encyclopedia of ocean sciences, edited by: Steele, jh, 1717–1730, 2001.

Philip L Richardson. How do albatrosses fly around the world without flapping their wings? *Progress in Oceanography*, 88(1-4):46–58, 2011.

Philip L Richardson. Leonardo da vinci's discovery of the dynamic soaring by birds in wind shear. *Notes and Records: the Royal Society journal of the history of science*, 73(3):285–301, 2019.

Philip L Richardson, Ewan D Wakefield, and Richard A Phillips. Flight speed and performance of the wandering albatross with respect to wind. *Movement ecology*, 6(1):1–15, 2018.

K.F. Riley, M.P. Hobson, and S.J. Bence. *Mathematical Methods for Physics and Engineering: A Comprehensive Guide*, chapter 21, pages 751–767. Cambridge University Press, 2002. ISBN 9780521890670.

Antonija Rimac, Jin-Song von Storch, Carsten Eden, and Helmuth Haak. The influence of high-resolution wind stress field on the power input to near-inertial motions in the ocean. *Geophysical Research Letters*, 40(18):4882–4886, 2013.

Dean Roemmich, Matthew H Alford, Hervé Claustre, Kenneth Johnson, Brian King, James Moum, Peter Oke, W Brechner Owens, Sylvie Pouliquen, Sarah Purkey, et al. On the future of argo: A global, full-depth, multi-disciplinary array. *Frontiers in Marine Science*, 6:439, 2019.

G Sachs, J Traugott, AP Nesterova, and F Bonadonna. Experimental verification of dynamic soaring in albatrosses. *Journal of Experimental Biology*, 216(22): 4222–4232, 2013.

A. C. Savage, A. F. Waterhouse, and S. M Kelly. Internal tide nonstationarity and wave-mesoscale interactions in the Tasman Sea. *J. Phys. Oceanogr.*, 50: 2931–2951, 2020.

Gary D Schnell and Jenna J Hellack. Flight speeds of brown pelicans, chimney swifts, and other birds. *Bird-banding*, 49(2):108–112, 1978.

Alvaro Semedo, Øyvind Saetra, Anna Rutgersson, Kimmo K Kahma, and Heidi Pettersson. Wave-induced wind in the marine boundary layer. *Journal of the Atmospheric Sciences*, 66(8):2256–2271, 2009.

Alvaro Semedo, Roberto Vettor, Øyvind Breivik, Andreas Sterl, Magnar Reistad, Carlos Guedes Soares, and Daniela Lima. The wind sea and swell waves climate in the nordic seas. *Ocean Dynamics*, 65(2):223–240, 2015.

A. F. Shchepetkin and J. C. McWilliams. The regional oceanic modeling system (ROMS): a split-explicit, free-surface, topography-following-coordinate oceanic model. *Ocean Modelling*, 9:347–404, 2005.

Ana Nobre Silva, Rui Taborda, Bruno Castelle, and Guillaume Dodet. Wave directional spreading importance on sheltered embayed beaches. *Journal of Coastal Research*, 95(SI):1536–1541, 2020.

Katherine E Silverthorne and John M Toole. Seasonal kinetic energy variability of near-inertial motions. *Journal of Physical Oceanography*, 39(4):1035–1049, 2009.

H. L. Simmons and M. H. Alford. Simulating the long-range swell of internal waves generated by ocean storms. *Oceanography*, 25:30–41, 2012.

Eric D Skyllingstad, Roger M Samelson, Harper Simmons, Lou S Laurent, Sophia Merrifield, Thilo Klenz, and Luca Centuroni. Boundary layer energetics of rapid wind and wave forced mixing events. *Journal of Physical Oceanography*, 2023.

A Smedman, Ulf Högström, Erik Sahlée, WM Drennan, KK Kahma, H Pettersson, and F Zhang. Observational study of marine atmospheric boundary layer characteristics during swell. *Journal of the atmospheric sciences*, 66(9):2747–2763, 2009.

Ann-Sofi Smedman, Michael Tjernström, and Ulf Högström. The near-neutral marine atmospheric boundary layer with no surface shearing stress: A case study. *Journal of Atmospheric Sciences*, 51(23):3399–3411, 1994.

W. H. F. Smith and D. T. Sandwell. Global sea floor topography from satellite altimetry and ship depth soundings. *Science*, 277:1956–1962, 1997.

Yu P Soloviev and VN Kudryavtsev. Wind-speed undulations over swell: Field experiment and interpretation. *Boundary-layer meteorology*, 136(3):341–363, 2010.

I. A. Stokes, S. M. Kelly, A. J. Lucas, A. F. Waterhouse, C. B. Whalen, T. Klenz, V. Hormann, and L. Centurioni. The role of the transition layer in atmospheric power input to near-inertial internal waves. *J. Phys. Oceanogr.*, page in review., 2023.

Roland B Stull, C Donald Ahrens, et al. *Meteorology for scientists and engineers*. Brooks/Cole, 2000.

Young B Suh and Cyrus Ostowari. Drag reduction factor due to ground effect. *Journal of Aircraft*, 25(11):1071–1072, 1988.

Peter P Sullivan and James C McWilliams. Dynamics of winds and currents coupled to surface waves. *Annual Review of Fluid Mechanics*, 42, 2010.

Peter P Sullivan, James B Edson, Tihomir Hristov, and James C McWilliams. Large-eddy simulations and observations of atmospheric marine boundary layers above nonequilibrium surface waves. *Journal of the Atmospheric Sciences*, 65 (4):1225–1245, 2008.

Oliver M Sun, Steven R Jayne, Kurt L Polzin, Bryan A Rahter, and Louis C St. Laurent. Scaling turbulent dissipation in the transition layer. *Journal of Physical Oceanography*, 43(11):2475–2489, 2013.

Guillaume Taburet, Antonio Sanchez-Roman, Maxime Ballarotta, Marie-Isabelle Pujol, Jean-François Legeais, Florent Fournier, Yannice Faugere, and Gerald Dibarboure. Duacs dt2018: 25 years of reprocessed sea level altimetry products. *Ocean Science*, 15(5):1207–1224, 2019.

Hidetoshi Takahashi and Isao Shimoyama. Waterproof pitot tube with high sensitive differential pressure sensor and nano-hole array. In *2018 IEEE Micro Electro Mechanical Systems (MEMS)*, pages 214–217. IEEE, 2018.

Hitoshi Tamura, William M Drennan, Clarence O Collins, and Hans C Graber. Turbulent airflow and wave-induced stress over the ocean. *Boundary-Layer Meteorology*, 169(1):47–66, 2018.

Graham Taylor and Adrian Thomas. *Evolutionary biomechanics: selection, phylogeny, and constraint*. OUP Oxford, 2014.

Graham K Taylor, Kate V Reynolds, and Adrian LR Thomas. Soaring energetics and glide performance in a moving atmosphere. *Philosophical Transactions of the Royal Society B: Biological Sciences*, 371(1704):20150398, 2016.

H. Tennekes and J. L. Lumley. *An First Course in Turbulence*. MIT Press, 1972.

Leif N Thomas, Luc Rainville, Olivier Asselin, William R Young, James Girton, Caitlin B Whalen, Luca Centurioni, and Verena Hormann. Direct observations of near-inertial wave ζ-refraction in a dipole vortex. *Geophysical Research Letters*, 47(21):e2020GL090375, 2020.

Richard E Thomson and W Stanford Huggett. Wind-driven inertial oscillations of large spatial coherence. *Atmosphere-Ocean*, 19(4):281–306, 1981.

Steve A Thorpe. *The turbulent ocean*. Cambridge University Press, 2005.

Jelle Treep, Gil Bohrer, Judy Shamoun-Baranes, Olivier Duriez, Renato Prata de Moraes Frasson, and Willem Bouten. Using high-resolution gps tracking data of bird flight for meteorological observations. *Bulletin of the American Meteorological Society*, 97(6):951–961, 2016.

Vance A Tucker. Gliding birds: reduction of induced drag by wing tip slots between the primary feathers. *Journal of experimental biology*, 180(1):285–310, 1993.

Lars Umlauf and Hans Burchard. Second-order turbulence closure models for geophysical boundary layers. a review of recent work. *Continental Shelf Research*, 25(7-8):795–827, 2005.

TS Van Den Bremer, Colin Whittaker, R Calvert, A Raby, and PH Taylor. Experimental study of particle trajectories below deep-water surface gravity wave groups. *Journal of Fluid Mechanics*, 879:168–186, 2019.

G. L. Wagner, G. Ferrando, and W. R. Young. An asymptotic model for the propagation of oceanic internal tides through quasi-geostrophic flow. *J. Fluid Mech.*, 828:779–811, 2017.

M. Watanabe and T. Hibiya. Global estimates of the wind-induced energy flux to inertial motions in the surface mixed layer. *Geophys. Res. Lett.*, 29:1239, 2002.

R. A. Weller. The relation of near-inertial motions observed in the mixed layer during the JASIN (1978) experiment to the local wind stress and to the quasi-geostrophic flow field. *J. Phys. Oceanogr.*, 12:1122–1136, 1982.

Hannah J Williams, Olivier Duriez, Mark D Holton, Giacomo Dell'Omo, Rory P Wilson, and Emily LC Shepard. Vultures respond to challenges of near-ground thermal soaring by varying bank angle. *Journal of Experimental Biology*, 221 (23), 2018.

JA Wilson. Sweeping flight and soaring by albatrosses. *Nature*, 257(5524):307–308, 1975.

Annie PS Wong, Susan E Wijffels, Stephen C Riser, Sylvie Pouliquen, Shigeki Hosoda, Dean Roemmich, John Gilson, Gregory C Johnson, Kim Martini, David J Murphy, et al. Argo data 1999–2019: Two million temperature-salinity profiles and subsurface velocity observations from a global array of profiling floats. *Frontiers in Marine Science*, 7:700, 2020.

Carl Wunsch. The work done by the wind on the oceanic general circulation. *Journal of Physical Oceanography*, 28(11):2332–2340, 1998.

W. R. Young and M. Ben Jelloul. Propagation of near inertial oscillations through a geostrophic flow. *J. Mar. Res.*, 55:735–766, 1997.

Jian Zhao, Amy Bower, Jiayan Yang, Xiaopei Lin, and Chun Zhou. Structure and formation of anticyclonic eddies in the iceland basin. *Journal of Geophysical Research: Oceans*, 123(8):5341–5359, 2018.

Yiyuan J Zhao and Ying Celia Qi. Minimum fuel powered dynamic soaring of unmanned aerial vehicles utilizing wind gradients. *Optimal control applications and methods*, 25(5):211–233, 2004.

Z. Zhao, M. H. Alford, J. B. Girton, L. Rainville, and H. L. Simmons. Global observations of open-ocean mode-1 M_2 internal tides. *J. Phys. Oceanogr.*, 46: 1657–1684, 2016.

Bin Zhu, Jianzhong Zhu, and Qingwei Chen. A bio-inspired flight control strategy for a tail-sitter unmanned aerial vehicle. *Science China Information Sciences*, 63:1–10, 2020.

Seth F Zippel, J Thomas Farrar, Christopher J Zappa, and Albert J Plueddemann. Parsing the kinetic energy budget of the ocean surface mixed layer. *Geophysical Research Letters*, 49(2):e2021GL095920, 2022.